

AFWL-TR-70-76

AFWL-TR-
70-76

AD712707



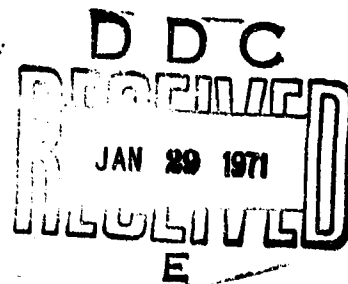
A LADAR CLOUD/TARGET POLARIZATION DISCRIMINATION TECHNIQUE

Joe E. Manz
Maj USAF

TECHNICAL REPORT NO. AFWL-TR-70-76

COLOR ILLUSTRATIONS REPRODUCED
IN BLACK AND WHITE

October 1970



AIR FORCE WEAPONS LABORATORY

Air Force Systems Command
Kirtland Air Force Base
New Mexico

Reproduced by
NATIONAL TECHNICAL
INFORMATION SERVICE
Springfield, Va. 22151

This document has been approved for public release
and sale; its distribution is unlimited.

183

AFWL-TR-70-76

A LADAR CLOUD/TARGET POLARIZATION
DISCRIMINATION TECHNIQUE

Joe E. Manz
Major USAF

TECHNICAL REPORT NO. AFWL-TR-70-76

This document has been approved
for public release and sale;
its distribution is unlimited.

AFWL-TR-70-76

AIR FORCE WEAPONS LABORATORY
Air Force Systems Command
Kirtland Air Force Base
New Mexico

When U. S. Government drawings, specifications, or other data are used for any purpose other than a definitely related Government procurement operation, the Government thereby incurs no responsibility nor any obligation whatsoever, and the fact that the Government may have formulated, furnished, or in any way supplied the said drawings, specifications, or other data, is not to be regarded by implication or otherwise, as in any manner licensing the holder or any other person or corporation, or conveying any rights or permission to manufacture, use, or sell any patented invention that may in any way be related thereto.

This report is made available for study with the understanding that proprietary interests in and relating thereto will not be impaired. In case of apparent conflict or any other questions between the Government's rights and those of others, notify the Judge Advocate, Air Force Systems Command, Andrews Air Force Base, Washington, D. C. 20331.

DO NOT RETURN THIS COPY. RETAIN OR DESTROY.

FOREWORD

This research was performed under Program Element 62601F, Project 5791, Task 028.

Inclusive dates of research were October 1964 through April 1970. The report was submitted 20 July 1970 by the Air Force Weapons Laboratory Project Officer, Major Joe E. Manz (ESA).

This technical report has been reviewed and is approved.

Joe E. Manz
JOE E. MANZ
Major, USAF
Project Officer

Walter M. Hart, Jr.
WALTER M. HART, JR.
Lt Colonel, USAF
Chief, Arming and Fuzing Branch

Carl F. Davis
CARL F. DAVIS
Colonel, USAF
Chief, Electronics Division

ABSTRACT

(Distribution Limitation Statement No. 1)

The use of laser detection and ranging (ladar) systems in the atmosphere is limited by the severe attenuation of the signal due to absorption by atmospheric gases and/or scattering by cloud and fog particles. Furthermore, the cloud and fog particles may scatter the transmitted radiation toward the receiver, thus producing a false return, which must be distinguished from the true target return. Described herein is an optical polarization technique for discriminating between a cloud return and a target return. Also presented are the results of a research program which demonstrated the validity of the discrimination technique both in the laboratory and in the field. The discrimination technique is based on the theory that if a linearly polarized laser beam propagating through an atmospheric cloud or fog is incident on a diffuse surface, then according to Mie theory the radiation scattered from the cloud is either linearly or elliptically polarized while the radiation reflected from the surface is depolarized. The results of the investigation described have shown that if the transmitter output of a ladar system is linearly polarized and an analyzer with its plane of polarization perpendicular to that of the transmitted wave is placed at the input to the receiver (which is adjacent to the transmitter), then the cloud return will be up to 94 percent less than the value obtained when the analyzer's plane of polarization is parallel to that of the transmitted signal. The target return remains unchanged. The conclusion is that the cloud/target discrimination technique will greatly improve the capability of a ladar system to distinguish between an atmospheric cloud and a target.

AFWL-TR-70-76

This page intentionally left blank.

CONTENTS

<u>Section</u>		<u>Page</u>
I	INTRODUCTION	1
II	THE PHYSICS OF ATMOSPHERIC AEROSOLS	4
	Introduction	4
	The Classification of Fogs and Clouds	5
	The Thermodynamics of the Formation of Atmospheric Aerosols	15
	Condensation in Particle-Free Air	26
	The Nuclei of Atmospheric Condensation and Sublimation	30
	The Growth and Size Distribution of Cloud Droplets	34
III	OPTICAL PROPERTIES OF ATMOSPHERIC AEROSOLS	43
	Introduction	43
	The Mie Theory of Scattering	44
	Application of Mie Theory to Atmospheric Aerosols	73
IV	THE DERIVATION OF THE CLOUD/TARGET POLARIZATION DISCRIMINATION TECHNIQUE	77
	Qualitative Description of the Discrimination Technique	77
	Mathematical Derivation of the Discrimination Technique	82
V	THE LABORATORY SIMULATION OF THE FORMATION OF ATMOSPHERIC AEROSOLS	96
	Introduction	96
	The Cloud Chamber	97
	Cloud Generation Techniques	100
	Cloud Sampling Techniques	104

CONTENTS (cont'd)

<u>Section</u>		<u>Page</u>
VI	EXPERIMENTAL VERIFICATION OF THE CLOUD/TARGET POLARIZATION DISCRIMINATION TECHNIQUE	117
	Introduction	117
	Cloud Chamber Experiments	125
	Sandia Peak Aerial Tramway Experiments	135
VII	DISCUSSION	146
	Conclusions	146
	Recommendations for Future Research	156
	REFERENCES	158

LIST OF ILLUSTRATIONS

<u>Figure</u>		<u>Page</u>
1	Geometry for Mie Scattering Problem	53
2	Geometry for Rayleigh's Roughness Criterion	78
3	Qualitative Illustration of the Cloud/Target Polarization Discrimination Technique	81
4	Geometry for Derivation of Ladar Range Equation	86
5	Geometry for Derivation of Cloud Return	90
6	Overall Dimensions of Cloud Chamber Module	98
7	Cut-away View of Cloud Chamber Module	101
8	Histogram of Droplet Diameters for First Sampling Method (Temperature: -5°C - 0°C)	109
9	Histogram of Droplet Diameters for First Sampling Method (Temperature: 0°C - $+5^{\circ}\text{C}$)	110
10	Histogram of Droplet Diameters for Second Sampling Method (Temperature: -5°C - 0°C)	112
11	Histogram of Droplet Diameters for Second Sampling Method (Temperature: 0°C - $+5^{\circ}\text{C}$)	113
12	Photomicrograph (x400) of Laboratory Generated Cloud Droplets	114
13	Photomicrograph (x400) of Laboratory Generated Coastal Fog Droplets	115
14	Experimental Arrangement for Photographs of Fig. 15	119
15	Photographic Illustration of the Cloud/Target Polarization Discrimination Technique. (a) Laser Output Linearly Polarized, No Analyzer on Camera; (b) Laser Output Linearly Polarized, Plane of Polarization of Analyzer (Located at Camera) Orthogonal to That of Transmitted Beam.	120
16	Experimental Arrangement for Photographs of Fig. 17	121
17	Photographic Illustration of the Cloud/Target Polarization Discrimination Technique. (a) Laser Output Linearly Polarized, No Analyzer on Camera; (b) Laser Output Linearly Polarized, Plane of Polarization of Analyzer (Located at Camera) Orthogonal to That of Transmitted Beam	122

LIST OF ILLUSTRATIONS (Continued)

<u>Figure</u>		<u>Page</u>
18	Experimental Arrangement for He-Ne Laser Cloud Scattering Experiments	126
19	Target Return vs. Cloud Transmissivity	129
20	Target and Cloud Returns vs. Cloud Transmissivity	131
21	Target and Cloud Returns vs. Cloud Transmissivity	132
22	Target and Cloud Returns vs. Cloud Transmissivity	133
23	Target and Cloud Returns vs. Cloud Transmissivity	134
24	Experimental Arrangement for Ruby Laser Cloud Scattering Experiments	136
25	Typical View of Sandia Tramway Cabin on Partially Cloudy Day	138
26	Interior View of Sandia Tramway Cabin Showing Experimental Arrangement Used for Laser Cloud Scattering Experiments	140
27	Oscillogram of Cloud and Target Returns. (a) Laser Transmitter Output Linearly Polarized, Plane of Polarization of Analyzer (Located at Receiver) Parallel to That of Transmitted Signal; (b) Laser Transmitter Output Linearly Polarized, Plane of Polarization of Analyzer (Located at Receiver) Orthogonal to That of Transmitted Signal. Vertical Sensitivity: .5v/div; Sweep Rate: 100 nanosec/div. Range: Cloud \approx 75 ft., Target \approx 150 ft.	141
28	Oscillogram of Cloud and Target Returns. (a) Laser Transmitter Output Linearly Polarized, Plane of Polarization of Analyzer (Located at Receiver) Parallel to That of Transmitted Signal; (b) Laser Transmitter Output Linearly Polarized, Plane of Polarization of Analyzer (Located at Receiver) Orthogonal to That of Transmitted Signal. Vertical Sensitivity: .2v/div; Sweep Rate: 100 nanosec/div. Range: Cloud \approx 100 ft., Target \approx 175 ft.	142

LIST OF ILLUSTRATIONS (Continued)

<u>Figure</u>		<u>Page</u>
29	Oscillogram of Cloud and Target Returns. (a) Laser Transmitter Output Linearly Polarized, Plane of Polarization of Analyzer (Located at Receiver) Parallel to That of Transmitted Signal; (b) Laser Transmitter Output Linearly Polarized, Plane of Polarization of Analyzer (Located at Receiver) Orthogonal to That of Transmitted Signal. Vertical Sensitivity: .2v/div; Sweep Rate: 200 nanosec/div. Range: Cloud = 80 ft., Target = 250 ft.	143
30	Typical View of Sandia Tramway Cabin Enveloped in a Dense Stratus Cloud. Camera Was Approximately 50 ft. from Cabin.	144
31	Target and Cloud Returns vs. Cloud Transmissivity for Realistic Earth Targets	151

LIST OF TABLES

<u>Table</u>		<u>Page</u>
1	Characterisitcs of Natural Fog and Cloud Droplets	41
2	Definition of Radiometric Quantities	84

ABBREVIATIONS AND SYMBOLS

Symbol	Definition	Page
$A_{ }(\theta)$	amplitude function whose electric vector is in the plane of scattering	75
$A_{\perp}(\theta)$	amplitude function whose electric vector is perpendicular to the plane of scattering	75
A_R	area of receiving aperture	88
A_t	area of the target illuminated by transmitted beam	89
A_v	gain of the receiver	153
\vec{a}_r	unit vector in r direction	54
\vec{a}_{θ}	unit vector in θ direction	54
\vec{a}_{ϕ}	unit vector in ϕ direction	54
\vec{a}_x	unit vector in the x direction	64
\vec{a}_y	unit vector in the y direction	64
\vec{a}_z	unit vector in the z direction	64
B	radiance	84
c_p	specific heat capacity of a gas at constant pressure	22
c_v	specific heat capacity of a gas at constant volume	22
D	coefficient of diffusion of water vapor in air	36
d_d	mode diameter of particles in distribution of cloud droplets	40
d_m	mean diameter of particles in distribution of cloud droplets	40
d_{\max}	maximum diameter of particles in distribution of cloud droplets	40

Symbol	Definition	Page
d_{\min}	minimum diameter of particles in distribution of cloud droplets	40
dQ	change in heat content of a gas	21
dq	change in heat content per unit mass of a gas	21
dU	change internal energy of a gas	21
du	change in specific internal energy of a gas	21
d_v	predominant volume diameter of particles in distribution of cloud droplets	40
dW	change in work performed by or done on a gas	21
E	irradiance	84
\vec{E}	electric field intensity vector	49
E_o	peak amplitude of incident electric field	63
E_R	irradiance at receiving aperture	89
E'_R	irradiance from cloud at receiving aperture	91
E_r	radial component of the electric field vector \vec{E}	54
E_θ	component of the electric field vector \vec{E} in the θ direction	54
E_ϕ	component of the electric field vector \vec{E} in the ϕ direction	55
E_x	component of the incident electric field in x direction	63
E_y	component of the incident electric field in y direction	63
E_z	component of the incident electric field in z direction	63

Symbol	Definition	Page
F	flux of water vapor	36
F	fraction of liquid water in air composed of drops of diameter less than x	40
\vec{H}	magnetic field intensity vector	49
H_0	peak amplitude of incident magnetic field	63
H_r	radial component of the magnetic field vector \vec{H}	53
H_θ	component of the magnetic field vector \vec{H} in the θ direction	54
H_ϕ	component of the magnetic field vector \vec{H} in the ϕ direction	54
H_x	component of incident magnetic field in x direction	63
H_y	component of incident magnetic field in y direction	63
H_z	component of incident magnetic field in z direction	63
h	relative humidity	25
I	radiant intensity	84
I_c	radiant intensity reflected from cloud	91
$I_{c }$	parallel component of relative intensity of cloud return whose plane of polarization parallel to that of the transmitted signal	130
$I_{c\perp}$	perpendicular component of relative intensity of cloud return whose plane of polarization perpendicular to that of the transmitted signal	130
I_{c+}	relative intensity of cloud return	130
I_R	radiant intensity at receiving aperture	89
I'_R	radiant intensity from cloud at receiving aperture	91
I_t	radiant intensity reflected from target	87
$I_{t }$	parallel component of relative intensity of target return whose plane of polarization parallel to that of the transmitted signal	127

Symbol	Definition	Page
$I_{t\perp}$	perpendicular component of relative intensity of target return whose plane of polarization perpendicular to that of the transmitted signal	127
I_{t+}	relative intensity of the target return	127
i	van't Hoff factor	35
i	imaginary number ($= \sqrt{-1}$)	54
i_{\parallel}	intensity function ($= A_{\parallel}(\theta) ^2$)	75
i_{\perp}	intensity function ($= A_{\perp}(\theta) ^2$)	75
$J_{n+1/2}^{(kr)}$	Bessel function of the first kind	61
$j_n(kr)$	spherical Bessel function of the first kind	61
K	thermal conductivity of air	38
k	volume coefficient of expansion	16
k^2	constant ($= \omega^2 \mu \epsilon - i \omega \mu \sigma$)	56
k_0	volume coefficient of expansion at 0°C	16
L	latent heat of condensation or evaporation	38
ladar	laser detection and ranging	3
l	height of surface irregularities	37
l	distance from target to receiver	85
M	gram-molecular weight	18
M_d	mean molecular weight of all atmospheric gases	19
M_w	molecular weight of water	19
m	mass	18
m_d	mean mass of all atmospheric gases except water vapor	24
m_w	mass of water vapor	24

Symbol	Definition	Page
$N_{n+1/2}(kr)$	Bessel function of the second kind	61
N_R	efficiency of receiver optics	153
$N(r)$	number of cloud droplets per cubic centimeter of size r	42
n	number of gram molecules contained in volume of gas	17
$n_n(kr)$	spherical Bessel function of the second kind	61
$n(r)$	volume concentration of cloud droplets	42
P	radiant flux (radiant power)	84
PDC	polarization discrimination coefficient	94
$P_n(\cos\theta)$	Legendre function of the first kind	66
$P_n^m(\cos\theta)$	associated Legendre function of the first kind	62
P_R	radiant flux (power) received	88
$P'_{R }$	component of radiant flux reflected from cloud with its polarization vector parallel to plane of polarization of transmitted signal	93
$P_{R\perp}$	component of radiant flux reflected from target with its polarization vector perpendicular to plane of polarization of transmitted signal	93
P_T	radiant flux (power) output of transmitter	88
P_t	radiant flux reflected from target	85
p	pressure	16
p_d	sum of partial pressures of all atmospheric gases except water vapor	19
p_r	vapor pressure at surface of cloud droplet	37
p_{rs}	saturation vapor pressure over surface of pure water droplet of radius r	29

Symbol	Definition	Page
P_w	partial pressure of water vapor	19
P_{ws}	saturation vapor pressure over plane surface of pure water	29
$Q_n^m(\cos\theta)$	associated Legendre function of the second kind	62
q	specific humidity	25
R	universal gas constant	17
R	radial direction	36
R'	individual gas constant ($= R/M$)	29
R_L	load resistance	153
r	radius of cloud droplet	29
r_c	critical radius of cloud droplet	37
r, θ, ϕ	coordinate axes of spherical coordinate system	51
S	sensitivity of the detector	153
SNR	signal-to-noise ratio for transmitter with plane polarized output	94
SNR_+	signal-to-noise ratio for transmitter with unpolarized output	93
T	temperature	19
T^*	virtual temperature	26
T_r	temperature at surface of cloud droplet	37
t	temperature	16
t	time	36
V_R	receiver output voltage	153
v	volume	89
v	molecular volume	18
V	volume	16

Symbol	Definition	Page
P_w	partial pressure of water vapor	19
P_{ws}	saturation vapor pressure over plane surface of pure water	29
$Q_n^m(\cos\theta)$	associated Legendre function of the second kind	62
q	specific humidity	25
R	universal gas constant	17
R	radial direction	36
R'	individual gas constant ($= R/M$)	29
R_L	load resistance	153
r	radius of cloud droplet	29
r_c	critical radius of cloud droplet	37
r, θ, ϕ	coordinate axes of spherical coordinate system	51
S	sensitivity of the detector	153
SNR	signal-to-noise ratio for transmitter with plane polarized output	94
SNR_+	signal-to-noise ratio for transmitter with unpolarized output	93
T	temperature	19
T^*	virtual temperature	26
T_r	temperature at surface of cloud droplet	37
t	temperature	16
t	time	36
V_R	receiver output voltage	153
v	volume	89
v	molecular volume	18
V	volume	16

Symbol	Definition	Page
x, y, z	coordinate axes of Cartesian coordinate system	51
α	constant ($= \sigma + i\omega\epsilon$)	63
α	specific volume	18
β	constant ($= -i\omega\mu$)	63
$\beta(\pi)$	angular volume scattering coefficient	91
$\beta_{11}(\pi)$	component of volume backscatter coefficient parallel to plane of polarization of transmitted signal	93
$\beta(\theta)$	angular volume scattering coefficient	75
γ	angle of incidence	77
ϵ	permittivity	49
η	transmission efficiency of polarizer	93
θ_R	receiver field of view	92
θ_T	beamwidth of transmitter	88
λ	wavelength	79
μ	permeability	49
$\vec{\Pi}, \vec{\Pi}^*$	Hertz vector potentials	56
Π_r	radial component of the Hertz field vector $\vec{\Pi}_r$	56
Π_r^*	radial component of the Hertz field vector $\vec{\Pi}^*$	56
Π_θ	component of the Hertz field vector $\vec{\Pi}$ in the θ direction	56
Π_θ^*	component of Hertz field vector $\vec{\Pi}^*$ in θ direction	56
Π_ϕ	component of the Hertz field vector $\vec{\Pi}$ in the ϕ direction	56
Π_ϕ^*	component of Hertz field vector $\vec{\Pi}^*$ in ϕ direction	56

Symbol	Definition	Page
ρ	density	18
ρ	position vector of any point	64
ρ	coefficient of reflection	85
ρ_d	sum of densities of all atmospheric gases except water vapor	19
ρ_l	density of the cloud droplet	37
ρ_{\perp}	component of reflection coefficient perpendicular to plane of polarization of transmitted signal	93
ρ_w	water vapor density (absolute humidity)	19
ρ_{ws}	water vapor density at saturation	25
σ	attenuation (extinction) coefficient ($= \sigma_a + \sigma_s$)	44
σ	conductivity	49
$\frac{1}{\sigma}$	extinction distance	45
σ_a	absorption coefficient	44
σ_s	scattering coefficient	44
τ	surface tension	29
τ	transmissivity	128
ψ, ψ^*	scalar potentials	49
ψ_i	scalar electric potential of the incident wave	67
ψ_i^*	scalar magnetic potential of the incident wave	67
ψ_s	scalar electric potential of the scattered wave	68
ψ_s^*	scalar magnetic potential of the scattered wave	68
ψ_o	scalar electric potential within sphere	68

Symbol	Definition	Page
ψ_o^*	scalar magnetic potential within sphere	68
ω	radian frequency ($= 2\pi f$, where f = frequency in Hz)	54
ω	solid angle	85
ω	mixing ratio	24
ω_s	saturation mixing ratio	25
	signifies radiation whose plane of polarization is parallel to that of the transmitted wave	117
⊥	signifies radiation whose plane of polarization is perpendicular to that of the transmitted wave	117
+	signifies unpolarized radiation	117

This page intentionally left blank.

SECTION I

INTRODUCTION

The development of the first laser in 1960 has stimulated multidisciplinary research in almost all areas of science and engineering. The list of applications is seemingly unlimited, running the gamut from retinal "welding" and "bloodless" surgery to power transmission systems. However, the list will not be expounded upon in this report. The reader is referred to Reference 39 for a comprehensive review of many laser applications. While considerable attention has been devoted to the application of lasers in communication and radar systems and to a lesser extent in surveillance and reconnaissance work, the effective use of such systems in the atmosphere is seriously limited by the severe attenuation of the laser signal due to absorption by atmospheric gases and/or scattering by cloud and fog particles. Furthermore, in detection and ranging applications (which broadly includes surveillance and reconnaissance applications, etc.) the cloud and fog particles may scatter the transmitted radiation in the direction of the receiver, thus producing a false return which must be distinguished from the true target return. It is the primary concern of this report to present a solution to the problem of distinguishing between the target return and the cloud return.

Most present day laser detection and ranging systems use some form of range gating (coincident pulse discrimination, binocular ranging, etc.) to eliminate (not solve) the cloud return problem. While for some situations this may be a satisfactory compromise between the advantages and disadvantages of using a laser system, the use of range-gating techniques to eliminate cloud returns is unacceptable in the majority of potential applications. Any electronic discrimination

technique based on determining the difference in characteristics between the cloud and target returns would probably be very complicated and extremely expensive if not impossible, to implement. What is needed, then, is a simple, reliable, inexpensive method for discriminating between cloud and target returns.

In 1908 Gustav Mie [Ref. 42] presented the results of his research on the interaction of a linearly polarized monochromatic plane wave of light with a single homogeneous sphere of any description situated in a homogeneous medium. He found that if the diameter of the sphere is of the same order of magnitude as the wavelength of the incident radiation, then the scattered radiation is, in general, either linearly or elliptically polarized depending on the plane of observation. At laser wavelengths, then, clouds actually represent a medium composed of Mie scattering particles. On the other hand, most targets—earth terrain including man-made irregularities, airborne objects such as aircraft, etc.,—can be considered to be diffuse scatterers at these wavelengths. Thus, one possible approach to developing a cloud/target discrimination technique that is both simple and reliable while being relatively inexpensive to implement could be based on the difference in the polarization characteristics of each return.

The purpose of this report is to describe an optical technique for discriminating between a cloud return and a target return, and to present the results of a research program to determine, experimentally, the validity of the discrimination technique. The feasibility evaluation of the discrimination technique encompasses such an enormous amount of multidisciplinary reference material that we shall restrict our discussion

to those subjects that are directly applicable to the investigation. Inasmuch as clouds present the most serious obstacle to the use of a ladar (laser detection and ranging) system in the atmosphere, we begin our report in Section II with a comprehensive discussion of the processes involved in the formation of an atmospheric cloud. Section III presents our derivation and a discussion of the Mie scattering equations. Section IV presents a qualitative description and the mathematical derivation of the discrimination technique. Section V describes the cloud-chamber facility used in the laboratory verification phase of the program. Section VI presents the results of the laboratory verification and field evaluation phases of the program. In Section VII a discussion of the feasibility of the discrimination technique is presented.

SECTION II

THE PHYSICS OF ATMOSPHERIC AEROSOLS

2.1 INTRODUCTION

A cloud or a fog can be described as a colloidal suspension in air of liquid water droplets or ice crystals, or a mixture of droplets and crystals, which is frequently referred to as an atmospheric aerosol. The formation of an atmospheric aerosol is dependent upon the conversion of some of the water vapor in the atmosphere to either the liquid or solid state or a combination thereof. The conversion process involving a direct change from the vapor state to the liquid state is defined as condensation, while a direct change from the vapor state to the solid state is called sublimation. As demonstrated by several researchers toward the end of the last century, the changes of state of water vapor in the atmosphere that result in the formation of clouds are dependent upon, (a) the numbers and types of condensation and sublimation nuclei present, and (b) the state of saturation of the surrounding air. The degree of saturation necessary for the formation of an aerosol can vary considerably depending on the hygroscopic nature and abundance of the condensation and sublimation nuclei. The process of condensation or sublimation of water vapor on suitable nuclei is called nucleation. For the nucleation process to proceed, it is necessary for the air to be maintained in a saturated or nearly saturated state which in essence requires some means of continuously supplying the necessary water vapor. A state of saturation may be achieved either by decreasing the temperature of the air to the point where its capacity for water vapor is

greatly reduced, or by adding water vapor to the air to the extent necessary to increase the content to the maximum capacity possible at the prevailing temperature. A combination of these processes may also result in a state of saturation. In general, a cloud is formed when air containing water vapor rises to the higher altitudes where a continuous decrease in atmospheric pressure results in the expansion and subsequent cooling of the moist air until some of the water vapor condenses or sublimates on the available nuclei.

2.2 THE CLASSIFICATION OF FOGS AND CLOUDS

An internationally accepted classification system for describing clouds is based primarily on visual appearance, and is essentially the same system as that proposed in 1803 by a British pharmacist, Luke Howard, [Ref. 25] and later modified by Renou [Ref. 49] and Hildebrandsson [Ref. 19] to include considerations of altitude. Since the close of the 19th century, the World Meteorological Organization has been responsible for any alterations to the basic system. It publishes in the form of an atlas [Ref. 62] the definitions and photographs of the different types of clouds. Ten genera of clouds are arranged into four groups according to their height above the ground, as follows:

High-Altitude Clouds

1. Cirrus - Temperate Regions: 20,000 to 40,000 feet
 - Polar Regions: Close to ground up to 40,000 feet
2. Cirrostratus 20,000 to 40,000 feet
3. Cirrocumulus 20,000 to 40,000 feet

Middle-Altitude Clouds - 6000 feet up to 20,000 feet

4. Altocumulus

5. Altostratus

Low-Altitude Clouds - close to ground up to 6,000 feet

6. Stratocumulus

7. Stratus

8. Nimbostratus

Clouds with Vertical Development

9. Cumulus

a. Cumulus humilis (fair-weather cumulus)

Bases: 500 to 10,000 feet

Tops: 1,000 to 15,000 feet

b. Cumulus congestus

Bases: 1,000 to 6,000 feet

Tops: 6,000 to 15,000 feet

10. Cumulonimbus

Bases: 1,000 to 6,000 feet

Tops: 10,000 to 40,000 feet

While an airflow crossing a hill, mountain or ridge may cause orographic clouds to form that appear to be different than any of the ten genera, the physical constitution of an orographic cloud is actually similar to Altocumulus, Stratocumulus or Cumulus Clouds and they are therefore classified under one or other of the ten genera.

These ten types of clouds may be further subdivided into species and varieties according to their structure and transparency. An example of two common species of cumulus clouds is shown in the above listing.

The following definitions of the ten genera of clouds, including a description of their physical constitution are taken verbatim from Volume I of the World Meteorological Organization's 1956 International Cloud Atlas.

1. Cirrus

(1) Definition

Detached clouds in the form of white, delicate filaments, or white or mostly white patches or narrow bands. These clouds have a fibrous (hair-like) appearance, or a silky sheen, or both.

(2) Physical Constitution

Cirrus is composed almost exclusively of ice crystals. These crystals are in general very small, a fact which, together with their sparseness, accounts for the transparency of most Cirrus clouds.

Dense Cirrus patches or Cirrus in tufts may nevertheless contain ice crystals large enough to acquire an appreciable terminal velocity, so that trails of considerable vertical extent may form. Sometimes, though not very frequently, the ice crystals in the trails melt into small water droplets; the trails are then greyish, in contrast with their usual white appearance, and may give rise to the formation of a rainbow.

The trails curve irregularly or slant as a result of wind shear and of the variation in size of the constituent particles; consequently, Cirrus filaments near the horizon do not appear parallel to it.

Halo phenomena may occur; circular haloes almost never show a complete ring, owing to the narrowness of the Cirrus clouds.

2. Cirrocumulus

(1) Definition

Thin, white patch, sheet or layer of cloud without shading, composed of very small elements in the form of grains, ripples, etc., merged or separate, and more or less regularly arranged; most of the elements have an apparent width of less than one degree.

(2) Physical Constitution

Cirrocumulus is composed almost exclusively of ice crystals; strongly supercooled water droplets may occur but are usually rapidly replaced by ice crystals.

A corona or irisation may sometimes be observed.

3. Cirrostratus

(1) Definition

Transparent, whitish cloud veil of fibrous (hair-like) or smooth appearance, totally or partly covering the sky, and generally producing halo phenomena.

(2) Physical Constitution.

Cirrostratus is composed mainly of ice crystals. The smallness of these crystals, their sparseness and the fact that Cirrostratus has at most only a moderate depth, account for the transparency of this cloud through which the outline of the sun is visible, at least when the latter is not too close to the horizon.

In certain types of Cirrostratus, some of the ice crystals are large enough to acquire an appreciable terminal velocity, so that trailing filaments are formed, which give these Cirrostratus clouds a fibrous appearance.

Halo phenomena are often observed in thin Cirrostratus; sometimes the veil of Cirrostratus is so thin that a halo provides the only indication of its presence.

4. Altocumulus

(1) Definition

White or gray, or both white and grey, patch, sheet or layer of cloud, generally with shading, composed of laminae, rounded masses, vells, etc., which are sometimes partly fibrous or diffuse and which may or may not be merged; most of the regularly arranged small elements usually have an apparent width between one and five degrees.

(2) Physical Constitution

Altocumulus is, at least in the main, almost invariably composed of water droplets. This is evident from the fairly low transparency of the microscopic elements and from the fact that the latter show sharp outlines when separate. Nevertheless, when the temperature is very low, ice crystals may form. If the droplets then evaporate, the cloud becomes entirely an ice cloud and its macroscopic elements cease to present sharp outlines. The formation of ice crystals may take place in all species of Altocumulus; it occurs most frequently in Altocumulus castellanus and flaccus.

A corona or irisation is often observed in thin parts of Altocumulus. Parhelia or luminous pillars are sometimes seen in Altocumulus, indicating the presence of tubular-shaped ice crystals.

5. Altostratus

(1) Definition

Greyish or bluish cloud sheet or layer of striated, fibrous or uniform appearance, totally or partly covering the sky, and having parts thin enough to reveal the sun at least vaguely, as through ground glass. Altostratus does not show halo phenomena.

(2) Physical Constitution

Altostratus nearly always appears as a layer of great horizontal extent [several tens or hundreds of kilometers (several tens or hundreds of miles)] and fairly considerable vertical extent [several hundreds or thousands of meters (several hundreds or thousands of feet)]. It is composed of water droplets and ice crystals. In the most complete case, three superposed parts may be distinguished, namely:

- a. An upper part, composed wholly or mainly of ice crystals,
- b. A middle part, composed of a mixture of ice crystals, snow crystals or snowflakes and supercooled water droplets,
- c. A lower part, composed wholly or mainly of ordinary or supercooled water droplets or drops.

In some cases, the cloud may consist of only two parts, either:

- an upper part like (a) and a lower part like (c) or
- an upper part like (b) and a lower part like (c).

Less frequently, the entire cloud may also be like (a) or like (b) alone.

The constituent particles in the lower part of Altostratus are so numerous that the outline of the sun or moon is always dimmed and the surface observer never sees halo phenomena. In the thickest parts, the position of the luminary may be completely concealed.

Raindrops or snowflakes are often present in Altostratus and below its base. When precipitation reaches the ground, it is generally of the "continuous" type and in the form of rain, snow or ice pellets.

6. Nimbostratus

(1) Definition

Grey cloud layer, often dark, the appearance of which is rendered diffuse by more or less continuously falling rain or snow, which in most cases reaches the ground. It is thick enough throughout to blot out the sun.

Low, ragged clouds frequently occur below the layer, with which they may or may not merge.

(2) Physical Constitution

Nimbostratus generally covers a wide area and is of great vertical extent. It is composed of water droplets (sometimes supercooled) and raindrops, of snow crystals and snowflakes, or of a mixture of these liquid and solid particles. The high concentration of particles and the great vertical extent of the cloud prevent direct sunlight from being observed through it. The cloud produces rain, snow or ice pellets which, however, do not necessarily reach the ground.

7. Stratocumulus

(1) Definition

Grey or whitish, or both grey and whitish, patch, sheet or layer of cloud which almost always has dark parts, composed of tessellations, rounded masses, rolls, etc., which are non-fibrous (except for virga) and which may or may not be merged; most of the regularly arranged small elements have an apparent width of more than five degrees.

(2) Physical Constitution

Stratocumulus is composed of water droplets, sometimes accompanied by raindrops or snow pellets and, more rarely, by snow crystals and snowflakes. Any ice crystals present are usually too sparse to give the cloud a fibrous appearance; during extremely cold weather, however, Stratocumulus may produce abundant ice crystal virga which may be accompanied by a halo. When Stratocumulus is not very thick, a corona or irisation is sometimes observed.

8. Stratus

(1) Definition

Generally, grey cloud layer with a fairly uniform base, which may give drizzle, ice prisms or snow grains. When the sun is visible through the cloud, its outline is clearly discernible. Stratus does not produce halo phenomena except, possibly, at very low temperatures.

Sometimes Stratus appears in the form of ragged patches.

(2) Physical Constitution

Stratus is usually composed of small water droplets; this cloud may, when very thin, produce a corona round the sun or moon. At very low temperatures, Stratus may consist of small ice particles. The ice cloud is usually thin and may, on rare occasions, produce halo phenomena.

Stratus, when dense or thick, often contains drizzle droplets and sometimes ice prisms or snow grains, it may then have a dark or even a threatening appearance. Stratus with a low optical thickness, when observed at more than 90 degrees from the sun, often shows a more or less smoky, greyish tint like that of fog.

9. Cumulus

(1) Definition

Detached clouds, generally dense and with sharp outlines, developing vertically in the form of rising mounds, domes or towers, or which the bulging upper part often resembles a cauliflower. The sunlit parts of these clouds are mostly brilliant white; their base is relatively dark and nearly horizontal.

Sometimes Cumulus is ragged.

(2) Physical Constitution

Cumulus is composed mainly of water droplets. When of great vertical extent, Cumulus may release precipitation in the form of rain showers.

Ice crystals may form in those parts of a cumulus in which the temperature is well below 0°C; they grow at the expense of evaporating supercooled water droplets, thereby transforming the cloud into Cumulonimbus. In cold weather, when the temperature in the entire cloud is well below 0°C (32°F), this process leads to the degeneration of the cloud into diffuse trails of snow.

10. Cumulonimbus

(1) Definition

Heavy and dense cloud, with a considerable vertical extent, in the form of a mountain or high towers. At least part of its upper portion is usually smooth, or fibrous or striated, and nearly always flattened; this part often spreads out in the shape of an anvil or vast plume.

Under the base of this cloud which often is very dark, there are frequently low ragged clouds either merged with it or not, and precipitation sometimes in the form of virga.

(2) Physical Constitution

Cumulonimbus is composed of water droplets and, especially in its upper portion, of ice crystals. It also contains large raindrops and, often, snowflakes, snow pellets, ice pellets or hailstones. The water droplets and raindrops may be substantially supercooled.

All other atmospheric phenomena have been grouped under the heading of meteors. The World Meteorological Organization defines a meteor as a phenomenon, other than a cloud, observed in the atmosphere or on the surface of the earth, which consists of a precipitation, a suspension or a deposit of aqueous or non-aqueous liquid or solid particles, or a phenomenon of the nature of an optical or electrical manifestation. Meteors are divided into four groups, hydrometeors, lithometeors, photometeors, and electrometeors, according to the nature of their constituent particles or the physical processes involved in their occurrence. The following definitions are taken verbatim from the International Cloud Atlas of 1956:

(1) Hydrometeors

A hydrometeor is a meteor consisting of an ensemble of liquid or solid water particles, falling through or suspended in the atmosphere, blown by the wind from the earth's surface, or deposited on objects on the ground or in the free air.

Hydrometeors consisting of ensembles of falling particles (rain, drizzle, snow, snow pellets, snow grains, ice pellets, ice prisms), originate mostly in clouds; the particles may reach the earth's surface (precipitation) or they may completely evaporate during their fall (virga)

(a) Rain. Precipitation of liquid water particles, either in the form of drops of more than 0.5 mm (0.02 in.) diameter or of smaller widely scattered drops. Freezing rain is defined as rain the drops of which freeze on impact with the ground or with objects on the earth's surface or with aircraft in flight.

(b) Drizzle. Fairly uniform precipitation composed exclusively of fine drops of water [diameter less than 0.5 mm (0.02 in.)], very close to one another. Freezing drizzle is defined as drizzle, the drops of which freeze on impact with the ground or with objects on the earth's surface or with aircraft in flight.

(c). Snow. Precipitation of ice crystals, most of which are branched (sometimes star-shaped).

(d) Snow Pellets. Precipitation of white and opaque grains of ice. These grains are spherical or sometimes conical; their diameter is about 2-5 mm (0.1-0.2 in.).

(e) Snow Grains. Precipitation of very small white and opaque grains of ice. These grains are fairly flat or elongated; their diameter is generally less than 1 mm (0.04 in.).

(f) Ice Pellets. Precipitation of transparent or translucent pellets of ice, which are spherical or irregular, rarely conical, and which have a diameter of 5 mm (0.2 in.) or less.

(g) Hail. Precipitation of small balls or pieces of ice (hailstones) with a diameter ranging from 5 to 50 mm (0.2 to 2.0 in.) or sometimes more, falling either separately or agglomerated into irregular lumps.

(h) Ice Prisms. A fall of unbranched ice crystals, in the form of needles, columns, or plates, often so tiny that they seem to be suspended in the air. These crystals may fall from a cloud or from a cloudless sky.

Hydrometeors consisting of ensembles of particles suspended in the air (fog, mist) are similar to clouds. They are, however, considered as meteors, owing to their occurrence at or near the earth's surface.

(i) Fog. A suspension of very small water droplets in the air, generally reducing the horizontal visibility at the earth's surface to less than 1 km (5/8 mile).

(j) Ice Fog. A suspension of numerous ice crystals in the air, reducing the visibility at the earth's surface.

(k) Mist. A suspension in the air of microscopic water droplets or wet hygroscopic particles, reducing the visibility at the earth's surface.

The hydrometeors consisting of ensembles of particles blown by the wind from the earth's surface (drifting snow, blowing snow and spray) are generally confined to the lowest layers of the atmosphere.

(l) Drifting Snow. An ensemble of snow particles raised by the wind to small heights above the ground. The visibility is not sensibly diminished at eye level. Eye level is defined as 1.8 m (6 feet) above the ground.

(m) Blowing Snow. An ensemble of snow particles raised by the wind to moderate or great heights above the ground. The horizontal visibility at eye level is generally very poor.

(n) Spray. An ensemble of water droplets torn by the wind from the surface of an extensive body of water, generally from the crests of waves, and carried up a short distance into the air.

The hydrometeors in the form of deposits (dew, hoar-frost, rime and glaze) occur either in the form of aggregate of particles, more or less individually discernible in spite of the fact that they are often fused together (hoar-frost, rime), or as homogeneous and smooth layers in which no particle structure can be discerned (glaze).

(o) Dew. A deposit of water drops on objects at or near the ground, produced by the condensation of water vapor

from the surrounding clear air. White dew is a deposit of white frozen dew drops.

(p) Hoar-Frost. A deposit of ice having a crystalline appearance, generally assuming the form of scales, needles, feathers or fans.

(q) Rime. A deposit of ice, composed of grains more or less separated by trapped air, sometimes adorned with crystalline branches.

(r) Rime (clear ice). A generally homogeneous and transparent deposit of ice formed by the freezing of supercooled drizzle droplets or raindrops on objects the surface temperature of which is below or slightly above 0°C (32°F).

(s) Spout. A phenomenon consisting of an often violent whirlwind, revealed by the presence of a cloud column or inverted cloud core (funnel cloud), protruding from the base of a Cumulonimbus, and of a "bush" composed of water droplets raised from the surface of the sea or of dust, sand or litter, raised from the ground.

(2) Lithometeors

A lithometeor is a meteor consisting of an ensemble of particles most of which are solid and non-aqueous. The particles are more or less suspended in the air, or lifted by the wind from the ground.

The lithometeors which have more or less the character of suspensions in the atmosphere are haze, dust haze and smoke; they consist of very small dust particles, of sea-salt particles or of combustion products (e.g., from forest fires).

(a) Haze. A suspension in the air of extremely small, dry particles invisible to the naked eye and sufficiently numerous to give the air an opalescent appearance.

(b) Dust Haze. A suspension in the air of dust or small sand particles, raised from the ground prior to the time of observation by a dust storm or sandstorm.

(c) Smoke. A suspension in the air of small particles produced by combustion.

The lithometeors resulting from the action of the wind are drifting and blowing dust or sand, dust storm or sandstorm, and dust whirl or sand whirl.

(d) Drifting dust or drifting sand. Dust or sand, raised by the wind to small heights above the ground. The visibility is not sensibly diminished at eye level.

(e) Blowing Dust or Blowing Sand. Dust or sand, raised by the wind to moderate heights above the ground. The horizontal visibility at eye level is sensibly reduced.

(f) Dust Storm or Sandstorm. An ensemble of particles of dust or sand energetically lifted to great heights by a strong and turbulent wind.

(g) Dust Whirl or Sand Whirl. An ensemble of particles of dust or sand, sometimes accompanied by small litter, raised

from the ground in the form of a whirling column of varying height with a small diameter and an approximately vertical axis.

(3) Photometeors.

A photometeor is a luminous phenomenon produced by the reflection, refraction, diffraction or interference of light from the sun or the moon.

Photometeors are observed in more or less clear air (mirage, shimmer, scintillation, green flash, twilight colors), or on inside clouds (halo phenomena, coronae, irisation, glory) and on or inside certain hydrometeors or lithometeors (glory, rainbow, fog bow, Bishop's ring, crepuscular rays).

(4) Electrometeors

An electrometeor is a visible or audible manifestation of atmospheric electricity.

Electrometeors either correspond to discontinuous electrical discharges (lightning, thunder) or occur as more or less continuous phenomena (Saint Elmo's fire, polar aurora).

2.3 THE THERMODYNAMICS OF THE FORMATION OF ATMOSPHERIC AEROSOLS

The processes involved in the formation of a cloud are governed by the laws of thermodynamics and are functions of changes in the pressure, temperature and volume relationships of the atmosphere. While the composition of the atmosphere consists of a mixture of gases and solid and/or liquid particles, it is the minor constituent water vapor that plays the dominant role on the formation of clouds. The fundamental laws governing the behavior of real gases are based on the kinetic theory of an ideal gas and the empirical relationships derived by the early investigators of gaseous behavior.

One of the first fundamental experiments in gaseous behavior was performed by Robert Boyle in 1660. He found that if the temperature and mass of a gas were held constant while measuring its volume at several different pressures, the product of the pressure and volume remained approximately constant. That is, for a fixed mass of a real gas kept at a constant temperature

$$pV \approx \text{constant} \quad (1)$$

where p and V represent the pressure and volume. Since the behavior of real gases follows this pressure-volume relationship only approximately, it was mathematically convenient to define an ideal gas where for a fixed mass at a given temperature

$$pV = \text{constant} \quad (2)$$

This is referred to as Boyle's Law.

In 1802 Gay-Lussac presented his findings relating the changes in the volume of a gas to changes in the temperature while the pressure is held constant. Mathematically, if V_0 represents the volume at a reference temperature, t_0 ,

$$V = V_0 [1 + k(t - t_0)] \quad (3)$$

where V is the volume at temperature t and k is defined as the volume coefficient of expansion. It is found that if k was measured at 0°C for a number of gases at different pressures, its value remained very nearly constant for all the gases and approximately equal to $1/273$ per centigrade degree. Thus, at a reference temperature of 0°C , Equation (3) becomes

$$V \approx V_0 (1 + k_0 t) \quad (4)$$

where $k_0 \approx 1/273$ per centigrade degree.

As in Boyle's relationship, it was mathematically convenient to extend the definition of an ideal gas where $k_0 = 1/273$ per centigrade degree and

$$V = V_0 (1 + k_0 t) \quad (5)$$

This relation is referred to as Gay-Lussac's Law.

We can combine the laws of Boyle and Gay-Lussac to obtain an equation of state for an ideal gas expressed as a relationship among pressure, volume, and temperature. Consider a given mass of an ideal gas. If the temperature is varied from an initial value $t_0 = 0^\circ\text{C}$ to a value t at constant pressure p_0 , then according to Gay-Lussac's law, the volume at temperature t , V_t can be expressed as

$$V_t = V_0(1+k_0 t) \quad (6)$$

Now, according to Boyle's law, if we vary the pressure to a value p while holding the temperature constant at t , the new volume V can be expressed as

$$pV = p_0 V_t \quad (7)$$

Substituting the expression for V_t from Equation (6) gives

$$pV = p_0 V_0(1+k_0 t) \quad (8)$$

or

$$pV = p_0 V_0 k_0 (t+1/k_0) \quad (9)$$

If we assume $t_0 = 0^\circ\text{C}$ and $p_0 = 1 \text{ atm}$, then it can be easily shown that

$$p_0 V_0 k_0 = nR \quad (10)$$

where n is the number of gram molecules contained in the volume V_0 and R is defined as the universal gas constant.

Now, since $1/k_0 = 273^\circ\text{C}$, the term in parentheses represents a temperature of $t + 273$ degrees centigrade which defines the Kelvin temperature scale. With $T = t + 273$ where T is expressed in degrees Kelvin, Equation (9) can now be written as

$$pV = nRT \quad (11)$$

and is known as the equation of state of an ideal gas.

In deriving the equation of state for atmospheric air, it is preferable to express Equation (11) in other forms. Let m represent the mass and M the gram-molecular weight of the volume V , then by definition the density is given by

$$\rho = \frac{m}{V} \quad (12)$$

$$n = \frac{m}{M} \quad (13)$$

and the specific volume α can be written as

$$\alpha = \frac{1}{\rho} = \frac{V}{m} \quad (14)$$

The molecular volume v is defined as

$$v = \frac{V}{n} \quad (15)$$

Therefore, substituting these relationships into Equation (11) gives

$$pV = \frac{m}{M} RT \quad (16)$$

$$\text{or} \quad p = \rho \frac{R}{M} T \quad (17)$$

$$\text{or} \quad p\alpha = \frac{R}{M} T \quad (18)$$

$$\text{or} \quad pv = RT \quad (19)$$

It is impossible to measure or calculate the molecular weight of atmospheric air because in reality, an air molecule does not exist since air consists of a mixture of gases; however, for purposes of this study, air can be considered to be composed of the following two gases: (1) water vapor and (2) pure dry air (includes all atmospheric gases except water vapor). Now, we can assume that the total pressure exerted by the atmosphere is governed by Dalton's Law which states that the total pressure exerted by a mixture of gases is equal to the sum of the

pressures exerted by each constituent of the mixture. The individual pressures exerted by each constituent are called partial pressures. Dalton discovered that the partial pressure of each constituent is the same as would be the actual pressure of that constituent if it alone occupied the entire volume at the same temperature as the mixture.

We can now write the equation of state for water vapor as

$$p_w = \rho_w \frac{R}{M_w} T \quad (20)$$

Where the subscript w refers to water vapor and p_w is the partial pressure of the water vapor, ρ_w is the vapor density or absolute humidity (mass of water vapor per unit volume) and M_w is the molecular weight of water.

Similarly, for dry air, the equation of state can be written as

$$p_d = \rho_d \frac{R}{M_d} T \quad (21)$$

Where the subscript d refers to dry air and p_d is the sum of partial pressures of the constituent gases, ρ_d is the sum of the individual densities, and M_d is the mean molecular weight of the mixture.

Now, according to Dalton's Law, the total atmospheric pressure p is given by

$$p = p_w + p_d \quad (22)$$

When the expressions for p_w and p_d from Equations (20) and (21) are substituted in Equation (22), we obtain

$$p = \rho_w \frac{R}{M_w} T + \rho_d \frac{R}{M_d} T \quad (23)$$

which can be written

$$p = \frac{R}{M_d} \rho_d \left[1 + \left(\frac{\rho_w}{\rho_d} \right) \left(\frac{M_d}{M_w} \right) \right] T \quad (24)$$

Now, Substituting the relation $\rho = \rho_w + \rho_d$ into Equation (24), gives

$$p = \frac{R}{M_d} (\rho - \rho_w) \left[1 + \left(\frac{\rho_w}{\rho_d} \right) \left(\frac{M_d}{M_w} \right) \right] T \quad (25)$$

which can be written

$$p = \rho \frac{R}{M_d} \left(1 - \frac{\rho_w}{\rho} \right) \left[1 + \left(\frac{\rho_w}{\rho_d} \right) \left(\frac{M_d}{M_w} \right) \right] T \quad (26)$$

and is one representation of the equation of state for atmospheric air. While exact measurements indicate that the equation of state for atmospheric air is only approximately valid, it is sufficiently accurate for most meteorological calculations. And, therefore, the real gases of the atmosphere may be treated as ideal gases for most computational purposes.

We know from basic thermodynamics that a substance (system) may be caused to change state by the performance of work or the transfer of heat. The exact process involved in the change is dependent on the definition of the system and its surroundings. The expansion or compression of a gas is accomplished by the performance of work and whenever a substance such as H_2O changes phase (melts, freezes, evaporates, condenses or sublimates), the change of state is brought about by a transfer of heat. The kinetic theory of gases states that the internal (kinetic) energy of a gas is directly proportional to the mean velocity of the molecules and the velocity of these molecules can be increased (decreased) by either heating (cooling) or by compressing (expanding) the gas. In addition, the first law of thermodynamics states that a change in the internal energy of a gas can be accomplished by the

transfer of heat or by performing work on the gas, or by a combination of the two processes. We can therefore use the first law of thermodynamics to describe the processes involved in the formation of a cloud. If the formation of the cloud occurs sufficiently far above the ground so that there is no solid or liquid surface to add or remove heat, we can assume that the formation of the cloud is essentially an adiabatic process which is determined primarily by the pressure changes experienced by a parcel of air in vertical motion.

If we represent the change in heat content by dQ and the change in internal energy by dU , both positive for an increase and negative for a decrease, and $+dW$ represents the work done on the gas, then the first law of thermodynamics can be written as

$$dQ = dU + dW \quad (27)$$

It can easily be shown that for a system where work is performed by means of expansion or compression only (as in the atmosphere), then

$$dW = pdV \quad (28)$$

and

$$dQ = dU + pdV \quad (29)$$

In the atmosphere we are dealing with fixed masses of air, and if we divide Equation (29) by the mass of the system we obtain another form of the first law:

$$dq = du + p d\alpha \quad (30)$$

where dq is the change in heat content per unit mass, du is the specific internal energy, and $d\alpha$ is the change in specific volume.

Now, we know by definition that an ideal gas satisfies the perfect gas law. It can also be shown by the kinetic-molecular theory of gases

that the internal energy of an ideal gas is a function of temperature only. While no real gas obeys these two conditions exactly, the degree to which these conditions are satisfied has been determined experimentally for most real gases. The results of these experiments indicate that for most meteorological computations the gases of the atmosphere can be assumed to be ideal and that their internal energy is a function of temperature only.

The temperature of a gas can be changed by varying the pressure while the volume is held constant, by varying the volume while the pressure is held constant, or by simultaneously varying both the pressure and volume. In each situation the amount of heat necessary for the change is different; however, only the first two cases are of practical interest and by convention we denote the specific heat capacity of a gas at constant volume as c_v and the specific heat capacity at constant pressure as c_p . For a constant volume process, i.e., $dV = 0$, it has been shown experimentally that

$$dq = du = c_v dT \quad (31)$$

The value of c_v determined experimentally has been found to be constant and Equation (31) is accepted as the definition of the change in internal energy and may be used whether the volume is held constant or not. Now, if the experiment is repeated while holding the pressure constant (i.e. the same amount of the same gas used in the derivation of Equation (31) is heated to the same temperature by varying the volume while the pressure is held constant), we obtain the following expression

$$c_p dT = c_v dT + p d\alpha \quad (32)$$

To obtain a relationship between the two specific heats, Equation (32) may be written in the form

$$(c_p - c_v)dT = pd\alpha \quad (33)$$

and by substituting the equation of state Equation (18) in its differential form, i.e., by substituting

$$pd\alpha + \alpha dp = \frac{R}{M} dT \quad (34)$$

into Equation (33), we obtain

$$(c_p - c_v) = \frac{R}{M} \quad (35)$$

where $dp = 0$ for a constant pressure process. This relationship shows that the specific heat capacity at constant pressure is larger than at constant volume.

We are now in a position to express the first law of thermodynamics in terms of the easily measured atmospheric variables of temperature and pressure. Starting with the first law in its general form

$$dq = c_v dT + pd\alpha \quad (36)$$

we substitute the value for α from Equation (18), for $pd\alpha$ from Equation (34) and the relationship of Equation (35) to obtain

$$dq = c_p dT - \frac{R}{M} T \frac{dp}{p} \quad (37)$$

Equation (37) represents the first law of thermodynamics for air in terms of temperature and pressure only.

Since an adiabatic process, i.e., one in which $dq = 0$, is the dominant mechanism in the formation of atmospheric clouds Equation (37) can be simplified accordingly to obtain several important relationships that describe the formation process. A complete mathematical derivation is quite lengthy and will not be presented here. The reader is referred to basic and advanced textbooks on meteorology, such as Hess [Ref. 21]

or Byers [Ref. 10] for a comprehensive treatment of the formation of an atmospheric cloud. Briefly, the results of a comprehensive mathematical treatment show that a cloud is formed by the lifting of a parcel of moist air which is cooled by adiabatic expansion at the lower pressures to a temperature (dew point) where some of the water vapor begins to condense into a fog or cloud of water droplets.

Looking at Equation (26), we can now define several of the more important meteorological variables that are used to describe the thermodynamic conditions in a given region of the atmosphere. The following definitions are derived from measurements taken in air over a plane surface of pure water where the water and air space above it are at the same temperature.

1. Vapor pressure, p_w : The vapor pressure is simply the partial pressure exerted by the water vapor in the air space. When the vapor pressure equals the vapor tension of the water surface, the air is said to be saturated with water vapor. If the vapor pressure is less than the vapor tension, the air is unsaturated. For the state of saturation the vapor pressure is usually referred to as the saturation vapor pressure and it has been determined empirically that it is a function of temperature independent of pressure.

2. Absolute humidity, ρ_w : The absolute humidity is defined as the water vapor density, ρ_w .

3. Mixing ratio, ω : The mixing ratio is defined as the ratio of the mass of water vapor present in the total air mixture to the mass of the dry air alone. Thus

$$\omega = \frac{m_w}{m_d} \quad (38)$$

Since, from Dalton's Law, all the gases occupy the same volume and $\rho = m/V$, Equation (38) can be expressed as

$$\omega = \frac{\rho_w}{\rho_d} \quad (39)$$

4. Specific humidity, q : The specific humidity is defined as the ratio of the mass of water vapor present in the total air mixture to the total mixture. Thus

$$q = \frac{m_w}{m_w + m_d} \quad (40)$$

or

$$q = \frac{\rho_w}{\rho_w + \rho_d} \quad (41)$$

where the denominator represents the total density of the air, ρ .

It can be easily shown that the specific humidity is related to the mixing ratio by

$$q = \frac{\omega}{1 + \omega} \quad (42)$$

5. Relative humidity, h : The relative humidity is defined as the ratio of the mixing ratio of a sample of air taken at some temperature other than saturation to the saturation mixing ratio of the air at the same temperature t . Thus

$$h = \frac{\omega}{\omega_s} \quad (43)$$

where the subscript refers to the value at saturation. The relative humidity can also be expressed as

$$h = \frac{\rho_w}{\rho_{ws}} \quad (44)$$

and

$$h = \frac{p_w}{p_{ws}} \quad (45)$$

6. Dew-point temperature, T_{dp} : The dew-point temperature is defined as the temperature at which saturation is achieved for air cooled at a constant pressure and mixing ratio.

By substituting the relationships for the mixing ratio and the specific humidity Equation (26) can be written as

$$p = \rho \frac{R}{M_d} (1-q) \left[1 + \omega \left(\frac{M_d}{M_w} \right) \right] T \quad (46)$$

Now, the ratio M_d/M_w is a dimensionless constant which can be easily calculated ($M_d = 28.966$, $M_w = 18$) to be 1.609. By eliminating ω from Equation (46), we get

$$p = \rho \frac{R}{M_d} (1+.609q) T \quad (47)$$

which is known as the equation of state for air and is usually expressed as

$$p = \rho \frac{R}{M_d} T^* \quad (48)$$

where

$$T^* = (1+.609q) T \quad (49)$$

and is called the virtual temperature.

2.4 CONDENSATION IN PARTICLE-FREE AIR

Even though scientists had been seriously investigating the processes involved in the formation of clouds since early in the nineteenth century, they had evidently ignored the role played by nuclei until late in that century, when the results of John Aitken's [Ref. 2] research showed that some sort of nuclei are involved in the condensation process.

Aitken's first experiments consisted of blowing steam into a receptacle containing air which had been filtered through cotton wool. He found that a more dense cloud formed in unfiltered air than in filtered air and therefore concluded that the condensation of water vapor occurs on some sort of nuclei which he referred to as "dust" particles. He then constructed an expansion chamber fitted with a microscope for counting the number of particles per unit volume of air which has come to be known as Aitken's "dust" counter. The results of his experiments with the "dust" counter indicated that below saturation, condensation occurs first on those "dust" (nuclei) particles that are hygroscopic, i.e., the nuclei that have an affinity for water vapor. For hydrophobic, i.e., non-hygroscopic nuclei, some degree of supersaturation is required before condensation can occur. Since saturation is defined as 100 percent relative humidity, supersaturation is defined as the percent relative humidity above 100, i.e., a relative humidity of 102 percent corresponds to a supersaturation of 2 percent. Aitken also discovered that if the air was free of nuclei, it was still possible to produce condensation but only for an appreciable degree of supersaturation. These results indicated that condensation can occur in nuclei-free air by the joining of sufficient numbers of water molecules to form an initial nucleus. However, the results of Aitken's work were open to argument because of the possibility that the steam itself contained condensation nuclei and that the filtering process removed only those particles which exceeded a certain size. It was for this reason, together with the knowledge that the data from other researchers were very incomplete and contradictory, that C.T.R. Wilson [Ref. 58] in 1897

initiated his own research effort to determine what degree of supersaturation can be obtained in moist air without condensation taking place. Wilson's experimental apparatus was similar to Aitken's in that it too was an expansion chamber and was actually the prototype of what was later to become known as the Wilson Cloud Chamber. Wilson's approach to obtain an unequivocal relation between degree of saturation and condensation in nuclei-free air was to repeatedly expand the same sample of air while protecting it from contamination. He found that the first expansion always produced a fog if the air had not been allowed to settle as completely as possible before contracting to its original volume so that the nuclei could be removed by being carried down into the water surface below by the condensation droplets. For each successive expansion and removal of nuclei, the resulting fogs became progressively thinner and thinner, the droplets becoming fewer and larger until the fog passed into a fine rain. Generally, thereafter, only one more expansion was needed to remove the remainder of the nuclei and for any greater expansion, no visible effect was produced until an expansion ratio corresponding to a relative humidity of 420 percent (supersaturation of 320 percent) was achieved at a final temperature of -5.8°C . The initial temperature had been 20°C . With larger expansions, a shower of drops was invariably produced until at an expansion ratio corresponding to a supersaturation of 690 percent, a transition from rain-like to cloud-like condensation occurred. The temperature of the air at this point of change was -15.8°C . Wilson found that the nuclei responsible for rain-like condensation could not be removed by filtering the air through cotton wool nor did it produce any effect upon the

expansion required for condensation to begin. Wilson then irradiated the filtered air in his chamber with X rays and found that no condensation occurred until exactly the same minimum supersaturation levels as in his original experiments were reached. However, he did observe that a much denser cloud had formed. Then, as Wilson increased the supersaturation above this upper limit, the condensation increased with enormous rapidity with the result that there was no indications of any limit to the number of droplets that could be produced. Wilson calculated the size of the smallest drops which would be able to grow in a highly supersaturated vapor using a relationship between the equilibrium (saturation) vapor pressure p_{rs} over the surface of a droplet of pure water of radius r and equilibrium vapor pressure p_{ws} over a plane surface of pure water at the same temperature derived by Lord Kelvin to be

$$\log \frac{p_{rs}}{p_{ws}} = \frac{2\tau}{\rho_w R' T r} \quad (50)$$

where τ is the surface tension, R' is the individual gas constant ($R' = R/M_w$) and T is the temperature. Wilson found that between the limits of supersaturation already mentioned, the value for r varied from 6.4×10^{-8} to 8.7×10^{-8} cm. The diameter of a water molecule is 4×10^{-8} cm.

Wilson's experimental results and calculations have been confirmed by later researchers and the only conclusion that can be drawn from Wilson's work is that if in nuclei-free and ion-free air the relative humidity increases to 800 percent, water droplets occur spontaneously when water vapor molecules combine to form small aggregates of water molecules which then act as condensation nuclei.

2.5 THE NUCLEI OF ATMOSPHERIC CONDENSATION AND SUBLIMATION

While Wilson's experiments in the laboratory demonstrated that enormously large supersaturations are required to produce cloud-like condensation in nuclei-free air, atmospheric clouds are not formed in this manner because in the atmosphere both hygroscopic and nonhygroscopic particles and small ions are always present to act as condensation and sublimation nuclei when the air is only slightly supersaturated or in many occurrences, even when the relative humidity is less than 100 percent. The atmosphere contains a large variety of particles in a wide range of sizes and concentrations and while scientists agree that some sort of nuclei other than water molecules are involved in the formation of an actual cloud-droplet, identification of the nature and physical composition of the actual nucleus has proven very difficult and is the subject of considerable controversy.

In 1913, Wigand [Ref. 57] measured the number of nuclei in a sample of air with an Aitken counter before and after he added nonhygroscopic particles such as coal dust. He found no increase in the nuclei count as a result of the increased dust content and therefore concluded that nonhygroscopic dust particles are not suitable condensation nuclei. Wigand's results and conclusions were verified in 1926 by Boylan [Ref. 7]. In 1936, Junge [Ref. 26] performed similar experiments with a variety of nonhygroscopic particles such as coal dust, dirt, emery powder, ground-up clay, household dust, and pulverized paraffin oil. Using an Aitken counter, he, in contrast to Wigand and Boylan, measured an increase in nuclei count as a result of increased dust content, but only when there was a large concentration of particles

smaller than 20 microns diameter. Junge concluded that the ability of nonhygroscopic particles to act as condensation nuclei depends on the size of the individual particle and is generally independent of its chemical composition.

Many researchers have investigated the behavior of various hygroscopic particles both theoretically and experimentally to determine to what extent they serve as condensation nuclei. A theoretical expression showing how the radius of a droplet of solution varies with relative humidity was derived by Köhler [Ref. 32] and is based on Lord Kelvin's derivation for a pure water droplet [Equation (50)]. A modified version of Köhler's expression first proposed in 1936 by Wright [Ref. 63] was the accepted form used for most calculations until a slightly more useful form was introduced by Mason [Ref. 40]. Because scientists originally believed that sea-salt particles were the main source of cloud-droplet nuclei (and many still do), a large amount of theoretical and experimental data has been generated on sodium chloride (NaCl) crystals and solutions. In 1926, Owens [Ref. 45] found that NaCl crystals became deliquescent at a relative humidity of 79 percent. Experimental confirmation of the general theory and Owen's work was published in 1949 by a french physicist, H. Dessens [Ref. 14]. Dessens collected NaCl crystals on fine spider threads and measured the diameters of the droplets formed about the crystals while varying the relative humidity. He found that the crystals became droplets of saturated solution at a relative humidity of 78 percent. Again in 1952, Junge [Ref. 27] repeated Dessens' spider-thread approach for artificially produced nuclei and obtained the same results. He also conducted

experiments on particles consisting of a mixture of insoluble and soluble matter. From his results and Wright's [Ref. 64] observation that visibility is a function of humidity for relative humidities above 70 percent, Junge suggested that in addition to hygroscopic and nonhygroscopic nuclei, the atmosphere also contains condensation particles consisting of insoluble matter with a thin covering of some hygroscopic substance. He called these particles "mixed nuclei" in that at relative humidities above 70 percent, they react as hygroscopic nuclei, while at humidities below 70 percent, they behave as nonhygroscopic particles.

The chemical analysis and electron microscopy of rime, frost, rain water, fog and cloud droplets made by many other investigators tend to verify Junge's theory. Köhler [Ref. 33] reported an almost constant chloride content of rime deposited around Halde Observatory in Sweden. The results of Woodcock's [Ref. 60, 61] research, which in addition to laboratory research, included data collected from a lighthouse in Florida, and from an aircraft over the mainland and sea around Hawaii, indicated that sea-salt particles are present in the atmosphere up to 3,000 meters and the concentration and size distribution of the particles did not change appreciably for sea air that had penetrated inland up to 110 km. The first attempt to identify actual condensation nuclei with the electron microscope was made by Kuroiwa [Ref. 36] who collected fog and cloud droplets on the coast and in the mountains of Japan. Kuroiwa found that some droplet residues contained NaCl crystals with traces of $MgCl_2$, and $MgSO_4$ while many more contained nonhygroscopic particles such as carbon granules and a few consisted of "mixed nuclei." He therefore concluded that combustion products are the most abundant source of

condensation nuclei with sea salt making a secondary but numerous contribution. A similar study was performed by Ogiwara and Okita [Ref. 44] who compared the residues of fog and cloud droplets with those of haze nuclei, sea-salt nuclei, and artificially produced combustion products. Their results indicated that combustion products were the main source of condensation nuclei while the influence of sea-salt appeared to be negligible. The results of a later investigation by Yamamoto and Ohtake [Ref. 40] agreed more with Kuroiwa's findings. Junge [Ref. 28] compared the electron-diffraction patterns of condensation nuclei gathered from actual fogs with the patterns of known chemical compounds. The results of his work indicated that particles of ammonium sulphate $(\text{NH}_4)_2 \text{SO}_4$ may be an important source of condensation nuclei. He also performed a chemical analysis of actual fog droplets and found that droplets of a radius greater than one micron exhibited a high chloride content while the smaller particles contained a higher proportion of NH_4^+ and SO_4^{--} . Two similar methods for measuring the chemical composition of airborne particles from an aircraft were proposed by Seely [Ref. 50] and Lodge [Ref. 38]. Both methods are based on the chemical reaction between the airborne particles and specific chemical reagents and both produced the same results as other methods.

It is generally believed that the sublimation process requires some kind of solid particle to act as a nucleus because droplets of pure solution probably could not induce sublimation. Cloud droplets in the atmosphere have been observed in the liquid state at temperatures

well below 0°C and experimental results indicate ice crystals form more commonly by the freezing of these supercooled droplets than by direct sublimation.

While the exact nature and chemical composition of the particles which serve as condensation and sublimation nuclei is still the subject of considerable controversy, scientists generally agree that atmospheric nuclei can originate in the following ways: (a) by condensation and sublimation of the vapors produced from industrial and domestic combustion processes; (b) by condensation and sublimation of the vapors produced from gaseous reactions in the atmosphere; (c) by the disintegration of matter, such as the formation of mineral dust and sea spray; and (d) by the coagulation of nuclei. The major unanswered question is which process is the main source of condensation and sublimation nuclei.

2.6 THE GROWTH AND SIZE DISTRIBUTION OF CLOUD DROPLETS

As we have discussed earlier, the meteorological variables used for describing the thermodynamic conditions of the atmosphere are based on measurements taken in a closed volume of air over a plane surface of pure water, and while these measurements are sufficiently accurate for most meteorological purposes such as weather forecasting, a study of the processes involved in droplet growth must include the effects of a spherical surface of a solution of impure water. Wilson demonstrated that in nuclei and ion-free air, condensation nuclei formed from small aggregates of water molecules occur spontaneously at extremely high supersaturations. These nuclei will remain in the liquid state and grow into water droplets only if they attain a critical size determined by the relationship expressed in Equation (50). We rearrange Equation (50)

in a slightly different form, i.e.,

$$r = \frac{2\tau}{\rho_w R T \log \frac{p_{rs}}{p_{ws}}} \quad (51)$$

to emphasize the relationship that must be satisfied in order that a condensation nuclei survive and not evaporate. This expression for the equilibrium vapor pressure over a curved liquid surface of pure water was originally derived by Lord Kelvin [Ref. 29]. An atmospheric droplet is never composed entirely of pure water and an expression similar to Lord Kelvin's for the equilibrium vapor pressure over a curved liquid surface of pure solution was first derived by Kohler [Ref. 32] in 1921. While several variations of Köhler's expression have been proposed, only Wright's [Ref. 63] and Mason's [Ref. 40] versions have found general acceptance by most scientists. Wright's expression for the equilibrium vapor pressure over a droplet of solution may be written

$$\frac{p_{rs}}{p_{ws}} = \frac{\exp\left(\frac{2\tau M_w}{\rho_w R T r}\right) - i m M_w}{\frac{4}{3}\pi r^3 \rho_w M} \quad (52)$$

where m is the mass and M is the molecular weight of the solute (nucleus) and i is known as the van't Hoff factor which is a function of the chemical composition and degree of dissociation of the solute. Mason's expression, which is more comprehensive and lengthy, will not be presented here. A complete and vigorous derivation is given in Mason [Ref. 40].

If a nucleus droplet attains or exceeds the critical radius necessary to ensure that it will not evaporate during the early stages of its

formation, then the droplet will continue to grow if a sufficient degree of supersaturation is maintained. The growth from a nucleus droplet to a cloud droplet is accomplished by the diffusion of water vapor to, and its subsequent condensation upon, the surface of the droplet, and by collision and coalescence with other droplets.

From Fick's Law of diffusion the flux, F , of water vapor in a radial direction, R , toward the droplet, is given by

$$F = D \frac{d\rho_w}{dR} \quad (53)$$

and the growth of the droplet of diffusion is therefore

$$\frac{dm}{dt} = DA \frac{d\rho_w}{dR} = 4\pi R^2 D \frac{d\rho_w}{dR} \quad (54)$$

where $\frac{dm}{dt}$ is the time rate increase of droplet mass, $A = 4\pi R^2$ is the surface area of the droplet, D is the coefficient of diffusion of water vapor in air and $\frac{d\rho_w}{dR}$ is the radial gradient of vapor density which is assumed to be symmetrical around the drop. If we assume that steady-state conditions exist, then $\frac{dm}{dt}$ is a constant and Equation (54) can be integrated with respect to the radial distance from the surface of the droplet where the vapor density is ρ_r to infinity where it is ρ_w .

Therefore,

$$\frac{dm}{dt} \int_r^\infty \frac{dR}{R^2} = 4\pi D \int_{\rho_r}^{\rho_w} d\rho_w \quad (55)$$

which gives

$$\frac{dm}{dt} = 4\pi D r (\rho_w - \rho_r) \quad (56)$$

Now, we can also express the time rate change of droplet mass as

$$\frac{dm}{dt} = 4\pi\rho_l r^2 \frac{dr}{dt} \quad (57)$$

where ρ_l is the density of the droplet.

Equating Equation (56) and Equation (57) gives

$$rdr = \frac{D}{\rho_l} (\rho_w - \rho_r) dt \quad (58)$$

Integrating the resulting expression, assuming that as the radius of the droplet varies from its critical value r_c to r , the time goes from $t = 0$ to $t = t$ gives

$$r^2 = r_c^2 + \frac{2D}{\rho_l} (\rho_w - \rho_r) t \quad (59)$$

This expression can be written in terms of vapor pressure as

$$r^2 = r_c^2 + \frac{2DM_w}{\rho_l R} \left(\frac{p_w}{T} - \frac{p_r}{T_r} \right) t \quad (60)$$

where R is the universal gas constant, p_r and T_r are respectively the vapor pressure and temperature at the surface of the droplet and p_w and T are the ambient vapor pressure and temperature. We see that a necessary condition for droplet growth (condensation) is that the term in parentheses be positive. A negative term signifies a state of evaporation. And since the temperature decreases with increasing distance from the droplet, the necessary condition for droplet growth is that the ambient vapor pressure be greater than the pressure at the surface of the droplet.

In addition to the other factors which determine the growth rate of a droplet, the condensation of water vapor to or the evaporation from a droplet involves the addition or removal of heat from the

surrounding air and is given by

$$\frac{dQ}{dt} = L \frac{dm}{dt} = \pm 4\pi R^2 K \frac{dT}{dR} \quad (61)$$

Where $\frac{dQ}{dt}$ is the rate of latent heat transfer, L is the latent heat of condensation or evaporation, K is the thermal conductivity of air, $\frac{dT}{dR}$ is the temperature gradient and the choice of sign depends on whether heat is being added or removed from the air. This expression may be integrated in a similar manner to Equation (54) and for the condensation process (negative sign) we obtain

$$L \frac{dm}{dt} = 4\pi K r (T_r - T) \quad (62)$$

and as before, by substitution of Equation (57) we obtain

$$r \frac{dr}{dt} = \frac{K}{L\rho_l} (T_r - T) \quad (63)$$

which can be integrated in a similar manner as Equation (58).

Now we can see from Equation (58) that for a given gradient of vapor density, $\frac{dr}{dt}$ is inversely proportional to r and from Equation (62) we see that for a given increment of radius the rate of transfer of latent heat increases as the radius of the droplet increases, i.e., $\frac{dQ}{dt} \propto r$. Therefore, since $\frac{dm}{dt}$ is assumed constant, an increase in the radius of the droplet produces a decrease in the vapor gradient until the excess water vapor is exhausted and an equilibrium condition is reached. It is for these reasons that most researchers agree that the condensation process alone is unlikely to produce droplets of radii > 30 microns. Actual measurements of droplet sizes have shown that while large droplets with radii up to 100 microns (borderline between cloud drops and rain drops) exist, most cloud and fog droplets have

radii of less than 30 microns with peak concentrations somewhere between 1 and 10 microns. Condensation on very large nuclei may produce a few of the larger droplets; however, growth by condensation for the larger droplets requires several hours. It is believed that the growth to larger droplets and raindrops is accomplished by the collision and coalescence of droplets moving relative to each other. Theoretical calculations show that cloud and fog droplets grow more rapidly by condensation during the early stages of development and the droplets must attain a radius of at least 20 microns before the coalescence process begins to predominate. Experimental verification has been obtained by several researchers and an excellent discussion of their work is presented in Mason [Ref. 40].

Much effort has been devoted to developing experimental techniques and equipment for measuring the size and size distribution of atmospheric and laboratory simulated fog and cloud droplets. The development, however, of reliable, accurate, and rapid labor saving instruments to measure droplet size and distribution, especially in the 1-5 microns range is an urgent requirement for cloud physics research. Notably lacking, also, are suitable techniques and equipment for use in airborne research such as from an aircraft. The newest instrument, a laser disdrometer, in which holography is used for measuring size and distribution of droplets within a given volume is limited in its application and has not been adapted to airborne use. In addition, the illuminated volume is small which requires a large number of holographs to obtain a representative sample of the size distribution and an ever tedious drop-by-drop measurement is the only reliable technique presently

available for sorting the droplets. The most reliable data on actual droplet distributions were obtained primarily by simple methods where the droplets are caught on a specially prepared surface and the diameter of the droplets or their impressions are measured under the microscope. A summary of some of the more important parameters characterizing the size distribution of droplets in different types of clouds along with the appropriate reference is shown in Table 1. The parameters used in Table 1 are defined as follows:

- d_{\min} is the minimum diameter of the droplets
- d_m is the mean diameter (the sum of all droplet diameters divided by the total number of droplets)
- d_d is the mode diameter (the diameter corresponding to the maximum number of droplets)
- d_v is the predominant volume diameter (the diameter corresponding to the maximum volume of water)
- d_{\max} is the maximum diameter of the droplets

Much effort has been devoted to formulating an analytical expression that would provide a best fit for the many different empirical distributions obtained from the numerous droplet size measurement programs. Best [Ref. 5] examined the experimental data of several researchers [Refs. 15, 16, 17, 18] and found that most of the observed droplet size distributions could be represented by the expression

$$1 - F = \exp \left[\left(\frac{-x}{a} \right)^b \right] \quad (64)$$

where F is the fraction of liquid water in the air composed of drops of diameter less than x , a is a numerical factor dependent on the liquid water content and b is a constant with a mean value of 3.27. One of the first universally accepted distributions was formulated by Junge [Ref. 28] and is given by the expression

Table 1
Characteristics of Natural Fog and Cloud Droplets

Cloud-Type	d_{\min} (μ)	d_m (μ)	d_d (μ)	d_v (μ)	d_{\max} (μ)	Concentration (cm^{-3})	Reference
Altostratus	2	10	9	14	26	450	15, 16
Stratocumulus	2	8	7	13	24	350	15, 16
	6			20-40	50	500	17
Stratus		16				310	8,9
	2	12	8	18	44	260	15, 16
	4		14		80		43
Nimbostratus		10.6				664	8,9
	2	12	8	24	40	330	15, 16
		22				175	8,9
Cumulus Humilis	6	18	12	26	66	300	56
	2		7	13	20		15, 16
Cumulus Congestus	6	48	12	102	166	64	56
Cumulonimbus	4	40	10		200	72	56
Clouds				22		50-500	23, 24
Fog	2			40-50	130	1-10	23, 24
	9	15.6			34		18
			5				3

$$N(r) = cr^{-p} \quad (65)$$

Where $N(r)$ is the number of particles per cubic centimeter of size r and c and p are numerical constants. A more recent and widely accepted distribution proposed by Deirmendjian [Ref. 13] is a generalization of the distribution first proposed by Khrgian and Mazin which may be written

$$n(r) = ar^{\alpha} e^{-br^{\gamma}} \quad (66)$$

where $n(r)$ is the volume concentration at the radius r and a , α , b and γ are positive constants. While many other distributions have been proposed, the three distributions quoted here represent the most widely accepted forms. In general, the attempts of the many researchers to analytically describe the droplet size distribution have resulted in the conclusion that atmospheric aerosol distributions exist in considerable variety.

SECTION III

OPTICAL PROPERTIES OF ATMOSPHERIC AEROSOLS

3.1 INTRODUCTION

The propagation of electromagnetic energy through the atmosphere has been studied for many decades, and the quantity of available literature on the subject is immense. The subject has received the attention of people in astronomy, communications, radar, meteorology, physics, physical chemistry, optics, spectroscopy and many other fields of endeavor. In some cases, this high degree of documentation has been accompanied by ever-increasing precision. Yet in the case of atmospheric aerosols there is still controversy as to whether salt crystals, sulphuric acid or nitrous oxide plays the dominant role in the nucleation of clouds and fogs.

As we discussed in the previous chapter the atmosphere is composed of a mixture of gases and water vapor in which are suspended a variety of hygroscopic and hydrophobic substances some of which may act as condensation nuclei in the formation of a cloud. These chemical and particulate constituents of the atmosphere attenuate electromagnetic radiation resulting in a loss of intensity greater than that experienced in free space. The attenuation of the propagating beam is caused by two independent processes: (1) absorption, whereby energy is removed from the beam by converting the radiation to some other form of energy, and (2) scattering, whereby some of the beam energy is redirected from its original direction of propagation. The gases and water vapor cause the radiation to be absorbed and the scattering of radiation is caused by nonuniformities which may be due either to the presence of particulate matter, to

macroscopic variation in the index of refraction (atmospheric turbulence). or to fluctuations on a microscopic scale of the number of molecules per unit volume (molecular scattering). The total attenuation, then, is equal to the sum of the absorbed and scattered radiation and is a function of the wavelength of the propagating energy.

When a collimated beam of monochromatic electromagnetic radiation of intensity I propagates through the atmosphere, a small increment dI of the intensity will be attenuated in passing through an infinitesimal thickness, dx , so we may write

$$dI = -\sigma I dx \quad (67)$$

where σ is a measure of the loss per unit length and is called the extinction (attenuation) coefficient. For a wave propagating over a finite distance, x , Equation (67) can be integrated to give

$$I = I_0 e^{-\sigma x} \quad (68)$$

where I_0 is the incident intensity and I is the intensity at the distance x .

If we assume that the attenuation of the propagating beam is due to the two independent processes of absorption and scattering, then the extinction coefficient is the sum of an absorption coefficient, σ_a , and a scattering coefficient, σ_s , and Equation (68) becomes

$$I = I_0 e^{-(\sigma_a + \sigma_s)x} \quad (69)$$

Equations (68) and (69) are often referred to as Bouguer's Law named after the French scientist who in 1760 formulated the law by experiment.

Both the coefficients σ_a and σ_s are functions of the wavelength of the propagating wave, and a medium is arbitrarily called transparent

if the extinction distance (defined to be $1/\sigma$) is large compared to the path length of interest. In the hard X-ray region —.01 to .1 Angstroms (Å)— the attenuation is due both to molecular absorption and molecular scattering (because of the short wavelengths the air molecules themselves act as scatterers) and the extinction distance is greater than 30 meters. As the wavelength increases, the extinction distance decreases until in the 2 to 20Å region it is less than 10 centimeters. As the wavelength continues to increase from the X-ray region to the far ultraviolet (around 100Å) the extinction distance, due mostly to absorption, is still less than 10 centimeters. At 2100Å a window appears which for pure oxygen and nitrogen extends out into the far infrared (IR).

The extinction distance would be greater than 300 meters. However, water vapor produces strong absorption bands in the regions near 1.5, 1.9, 2.7 and 6.3 microns (μ) while carbon dioxide produces strong absorption bands at 2.7 and 4.3 μ . The presence of both of these gases in the atmosphere reduces the extinction distance to less than one meter in these regions. As the wavelength increases through the far IR into the millimeter wavelength region, the attenuation is due primarily to the scattering from particulate matter and decreases steadily until below X-band the atmospheric attenuation is essentially negligible.

In this investigation we will restrict ourselves to wavelengths within the regions of major atmospheric windows where the extinction length is much greater than the path lengths of interest and where two of the scattering mechanisms, atmospheric turbulence and molecular scattering, are essentially negligible. In atmospheric turbulence, the size of the disturbing elements is several orders of magnitude larger than

macroscopic variation in the index of refraction (atmospheric turbulence), or to fluctuations on a microscopic scale of the number of molecules per unit volume (molecular scattering). The total attenuation, then, is equal to the sum of the absorbed and scattered radiation and is a function of the wavelength of the propagating energy.

When a collimated beam of monochromatic electromagnetic radiation of intensity I propagates through the atmosphere, a small increment dI of the intensity will be attenuated in passing through an infinitesimal thickness, dx , so we may write

$$dI = -\sigma I dx \quad (67)$$

where σ is a measure of the loss per unit length and is called the extinction (attenuation) coefficient. For a wave propagating over a finite distance, x , Equation (67) can be integrated to give

$$I = I_0 e^{-\sigma x} \quad (68)$$

where I_0 is the incident intensity and I is the intensity at the distance x .

If we assume that the attenuation of the propagating beam is due to the two independent processes of absorption and scattering, then the extinction coefficient is the sum of an absorption coefficient, σ_a , and a scattering coefficient, σ_s , and Equation (68) becomes

$$I = I_0 e^{-(\sigma_a + \sigma_s)x} \quad (69)$$

Equations (68) and (69) are often referred to as Bouguer's Law named after the French scientist who in 1760 formulated the law by experiment.

Both the coefficients σ_a and σ_s are functions of the wavelength of the propagating wave, and a medium is arbitrarily called transparent

Scattering is probably responsible for the many attempts to formulate a similar relationship between the scattering coefficient and wavelength for atmospheric aerosols. However, the derivation of a theory describing the scattering mechanism in aerosols such as clouds and fogs is complicated by the many variables such as particle composition, concentration, size distribution, etc. Therefore, a straightforward relationship has not been found as in the case of Rayleigh scattering.

In 1908 a German meteorologist, Gustav Mie [Ref. 42], derived in terms of electromagnetic wave theory a solution for the electric and magnetic vectors describing the radiation scattered by a homogeneous sphere of any diameter situated in a homogeneous medium. While his work was originally in the field of colloidal chemistry, it is applicable to many other problems and Stratton and Houghton [Ref. 52] were the first researchers to apply the Mie Theory of Scattering to the problem of optical transmission in atmospheric aerosols.

3.2 THE MIE THEORY OF SCATTERING

In 1908 Gustav Mie [Ref. 42] derived the first rigorous solution for the diffraction of a linearly polarized monochromatic plane wave by a single homogeneous sphere of any description situated in a homogeneous medium. Mie approached the problem in terms of the electromagnetic wave theory of radiation in which a periodic wave incident on a homogeneous sphere of arbitrary size and composition induces a forced oscillation of the free and bound charges. These forced oscillations themselves generate a secondary field both inside and outside the sphere where the resultant field outside the sphere is the sum of the incident and secondary fields.

In 1909 Debye [Ref. 12] published a similar solution of the same problem where he used a pair of potential functions that have come to be known as Debye's potentials. While Mie's original work was concerned with the passage of light through a colloidal suspension of metallic particles, the Mie Theory of Scattering is of great practical value. Since then many researchers have applied the theory to a variety of problems. Stratton and Houghton [Ref. 52] appear to be the first writers to apply the theory to the transmission of light through clouds and fogs.

A thorough treatment of Mie's theory is beyond the scope of this paper and we shall therefore restrict ourselves to those parts of the theory that are directly applicable to our investigation. The reader is referred to Stratton [Ref. 53] or Born and Wolf [Ref. 6] for a vigorous mathematical treatment and to van de Hulst [Ref. 54] for a clear and comprehensive discussion.

Mie treated the scattering of light by a homogeneous sphere in terms of Maxwell's field relations and the corresponding wave equations. We know that an electromagnetic field which is a function of both space and time cannot, in general, be derived solely from a scalar function. For a solution to this problem the integration of Maxwell's equations can be reduced to deriving a vector and a scalar potential that both satisfy the same differential equation (commonly referred to as the inhomogeneous wave equation) as that obeyed by the fields. On the other hand Hertz [Ref. 20] has shown that an electromagnetic field can be expressed in terms of a single vector function. We shall show that an electromagnetic field within an isotropic, homogeneous, charge-free

conducting medium can be resolved into two partial fields, each derivable from separate Hertz vectors each of which satisfy the vector wave equation.

We begin by expressing Maxwell's time varying field relations for a homogeneous, isotropic, charge-free, conducting medium in the following form

$$\vec{\nabla} \times \vec{H} = (\sigma + \epsilon \frac{\partial}{\partial t}) \vec{E} \quad (70)$$

$$\vec{\nabla} \times \vec{E} = -\mu \frac{\partial \vec{H}}{\partial t} \quad (71)$$

$$\vec{\nabla} \cdot \vec{H} = 0 \quad (72)$$

$$\vec{\nabla} \cdot \vec{E} = 0 \quad (73)$$

where

\vec{H} = magnetic field intensity

\vec{E} = electric field intensity

σ = conductivity of the medium

ϵ = permittivity of the medium

μ = permeability of the medium

Since the \vec{H} field is solenoidal it can be represented by the curl of another vector \vec{A} , i.e.

$$\vec{H} = \vec{\nabla} \times \vec{A} \quad (74)$$

and it can be shown that the corresponding \vec{E} field is given by

$$\vec{E} = -\vec{\nabla}\psi - \frac{\partial \vec{A}}{\partial t} \quad (75)$$

Now since the \vec{E} field is also solenoidal an alternate solution can be derived in terms of a vector potential \vec{A}^* and a scalar potential ψ^* .

$$\vec{E} = -\frac{1}{c} \vec{\nabla} \times \vec{A}^* \quad (76)$$

$$\vec{H} = -\vec{\nabla}\psi^* - \frac{\partial \vec{A}}{\partial t}^* - \frac{\sigma}{\epsilon} \vec{A}^* \quad (77)$$

Now, if we let

$$\vec{A} = (\sigma + \epsilon \frac{\partial}{\partial t}) \vec{\Pi} \quad (78)$$

where $\vec{\Pi}$ is another vector potential then Equations (74) and (75) become

$$\vec{H} = (\sigma + \epsilon \frac{\partial}{\partial t}) \vec{\nabla} \times \vec{\Pi} \quad (79)$$

$$\vec{E} = -\vec{\nabla}\psi - (\sigma + \epsilon \frac{\partial}{\partial t}) \frac{\partial \vec{\Pi}}{\partial t} \quad (80)$$

Now, since the choice of the scalar potential ψ is arbitrary as long as it satisfies the wave equation, we can define it as

$$\psi = -\vec{\nabla} \cdot \vec{\Pi} \quad (81)$$

Equation (80) now becomes

$$\vec{E} = \vec{\nabla} \vec{\nabla} \cdot \vec{\Pi} - (\sigma + \epsilon \frac{\partial}{\partial t}) \frac{\partial \vec{\Pi}}{\partial t} \quad (82)$$

Upon substitution of Equations (79) and (82) into Equation (70) we obtain the vector equation

$$\vec{\nabla} \times \vec{\nabla} \times \vec{\Pi} - \vec{\nabla} \vec{\nabla} \cdot \vec{\Pi} + \mu \sigma \frac{\partial \vec{\Pi}}{\partial t} + \mu \epsilon \frac{\partial^2 \vec{\Pi}}{\partial t^2} = 0 \quad (83)$$

every solution of which determines an electromagnetic field given by

$$\vec{H} = (\sigma + \epsilon \frac{\partial}{\partial t}) \vec{\nabla} \times \vec{\Pi} \quad (84)$$

$$\vec{E} = \vec{\nabla} \times \vec{\nabla} \times \vec{\Pi} \quad (85)$$

An alternate solution satisfying Equations (76) and (77) can be constructed in terms of \vec{A}^* and ψ^* where

$$\vec{A}^* = \mu \epsilon \frac{\partial \vec{\Pi}^*}{\partial t} \quad (86)$$

$$\psi^* = -\vec{\nabla} \cdot \vec{\Pi}^* \quad (87)$$

Consequently,

$$\vec{H} = \vec{\nabla} \times \vec{\nabla} \times \vec{\Pi}^* \quad (88)$$

$$\vec{E} = -\mu \vec{\nabla} \times \frac{\partial \vec{\Pi}^*}{\partial t} \quad (89)$$

The general solution, then, for a time-varying electromagnetic field in a homogeneous, isotropic, charge-free, conducting medium can be expressed as the sum of two partial fields, each derivable from separate Hertz vectors ($\vec{\Pi}$ and $\vec{\Pi}^*$).

Thus,

$$\vec{E} = \vec{\nabla} \times \vec{\nabla} \times \vec{\Pi} - \mu \vec{\nabla} \times \frac{\partial \vec{\Pi}^*}{\partial t} \quad (90)$$

$$\vec{H} = \vec{\nabla} \times \vec{\nabla} \times \vec{\Pi}^* + \vec{\nabla} \times \left(\sigma + \epsilon \frac{\partial}{\partial t} \right) \Pi \quad (91)$$

Since the scattered fields represent outgoing spherical waves, Mie chose to represent Maxwell's equations, the incident radiation, and the scattered radiation in terms of the spherical coordinates, r , θ , and ϕ defined by

$$x = r \cos \theta \quad (92)$$

$$y = r \sin \theta \cos \phi \quad (93)$$

$$z = r \sin \theta \sin \phi \quad (94)$$

where x , y , and z represent a rectangular coordinate system with origin at the center of the sphere. The z -direction is taken as the direction of propagation of the incident wave with the x -direction in the direction of its electric field vector. In our derivation of Mie's formulas we modify Mie's geometry slightly and redefine the angle θ to be the angle

between the direction of propagation of the incident wave and the scattered wave. With this definition the angle θ is universally referred to as the scattering angle and the corresponding curvilinear coordinate system is defined as

$$x = r \sin\theta \cos\phi \quad (95)$$

$$y = r \sin\theta \sin\phi \quad (96)$$

$$z = r \cos\theta \quad (97)$$

where the plane of scattering is defined as the plane containing the axis of propagation and the radius vector from the center of the sphere to a point of observation. If we define the plane of oscillation as the plane containing the electric field vector of the incident wave and the axis of propagation, then the angle ϕ represents the angle between this plane and the plane of scattering (See Fig. 1).

In spherical coordinates, the curl of any vector \vec{A} is given by

$$\begin{aligned} \vec{\nabla} \times \vec{A} = & \left\{ \frac{1}{r \sin\theta} \left[\frac{\partial(\sin\theta A_\phi)}{\partial\theta} - \frac{\partial A_\theta}{\partial\phi} \right] \right\} \vec{a}_r \\ & + \left\{ \frac{1}{r} \left[\frac{1}{\sin\theta} \frac{\partial A_r}{\partial\phi} - \frac{\partial(r A_\phi)}{\partial r} \right] \right\} \vec{a}_\theta \\ & + \left\{ \frac{1}{r} \left[\frac{\partial(r A_\theta)}{\partial r} - \frac{\partial A_r}{\partial\theta} \right] \right\} \vec{a}_\phi \end{aligned} \quad (98)$$

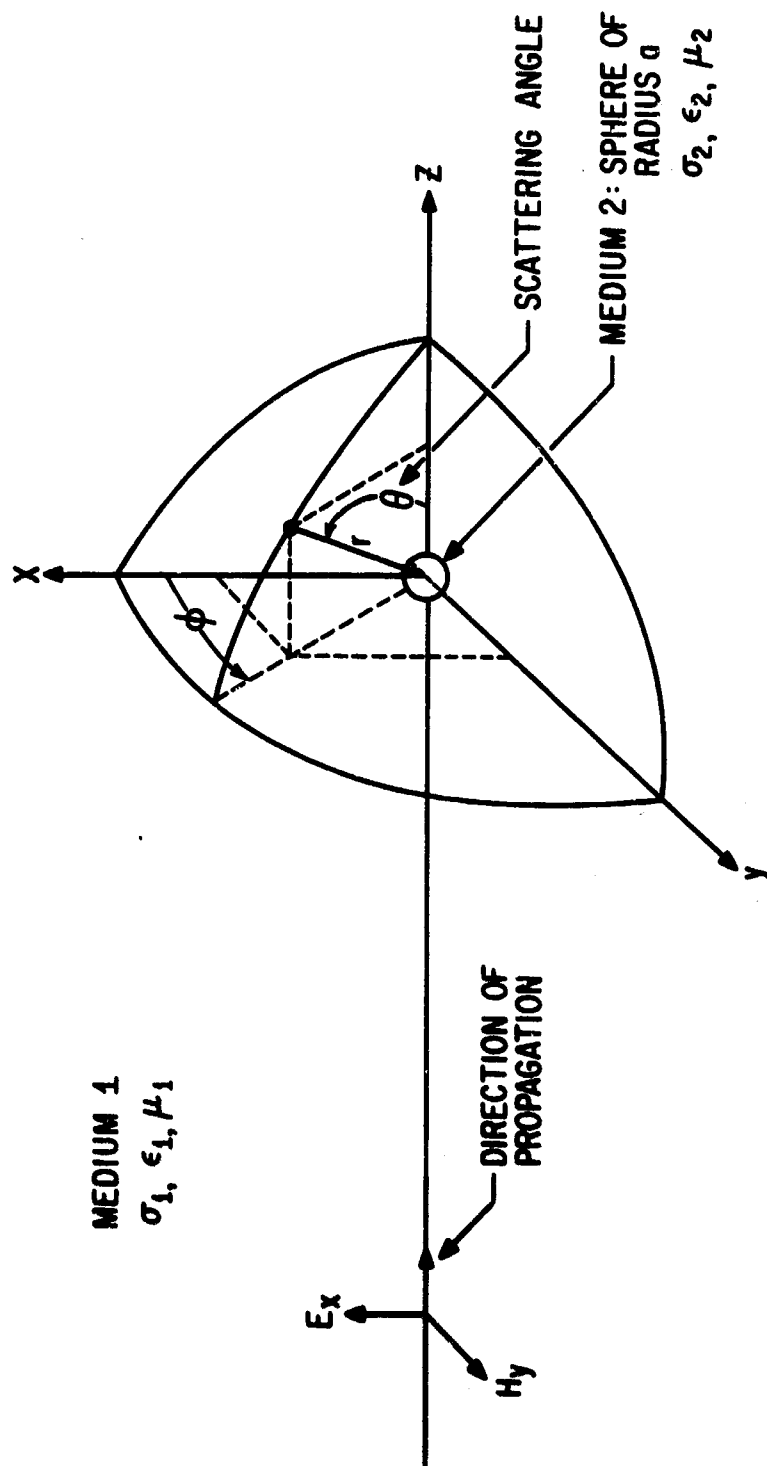


Figure 1. Geometry for Mie Scattering Problem

and

$$\begin{aligned}
 \vec{\nabla} \times \vec{\nabla} \times \vec{A} = & \left\{ \frac{1}{r^2 \sin \theta} \frac{\partial [\sin \theta (\frac{\partial A_\theta}{\partial r} - \frac{\partial A_r}{\partial \theta})]}{\partial \theta} \right. \\
 & - \frac{1}{r^2 \sin \theta} \frac{\partial [\frac{1}{\sin \theta} (\frac{\partial A_r}{\partial \phi} - \frac{\partial r \sin \theta A_\phi}{\partial r})]}{\partial \phi} \left. \right\} \vec{a}_r \\
 & + \left\{ \frac{1}{r \sin \theta} \frac{\partial [\frac{1}{r^2 \sin \theta} (\frac{\partial r \sin \theta A_\phi}{\partial \theta} - \frac{\partial r A_\theta}{\partial \phi})]}{\partial \phi} \right. \\
 & - \frac{1}{r \sin \theta} \frac{\partial [\sin \theta (\frac{\partial A_\theta}{\partial r} - \frac{\partial A_r}{\partial \theta})]}{\partial r} \left. \right\} \vec{a}_\theta \\
 & + \left\{ \frac{1}{r} \frac{\partial [\frac{1}{\sin \theta} (\frac{\partial A_r}{\partial \phi} - \frac{\partial r \sin \theta A_\phi}{\partial r})]}{\partial r} \right. \\
 & - \frac{1}{r} \frac{\partial [\frac{1}{r^2 \sin \theta} (\frac{\partial r \sin \theta A_\phi}{\partial \theta} - \frac{\partial r A_\theta}{\partial \phi})]}{\partial \theta} \left. \right\} \vec{a}_\phi \quad (99)
 \end{aligned}$$

where

\vec{a}_r = unit vector in r direction

\vec{a}_θ = unit vector in θ direction

\vec{a}_ϕ = unit vector in ϕ direction

Assuming a time dependence of the form $e^{i\omega t}$ Maxwell's equations can be expressed as

$$\frac{1}{r^2 \sin \theta} \left[\frac{\partial (r \sin \theta H_\phi)}{\partial \theta} - \frac{\partial (r H_\theta)}{\partial \phi} \right] = (\sigma + i\omega \epsilon) E_r \quad (100)$$

$$\frac{1}{r \sin \theta} \left[\frac{\partial H_r}{\partial \phi} - \frac{\partial (r \sin \theta H_\phi)}{\partial r} \right] = (\sigma + i\omega \epsilon) E_\theta \quad (101)$$

$$\frac{1}{r} \left[\frac{\partial(rH_\theta)}{\partial r} - \frac{\partial H_r}{\partial \theta} \right] = (\sigma + i\omega\epsilon) E_\phi \quad (102)$$

$$\frac{1}{r^2 \sin\theta} \left[\frac{\partial(r \sin\theta E_\phi)}{\partial \theta} - \frac{\partial(r E_\theta)}{\partial \phi} \right] = -i\omega\mu H_r \quad (103)$$

$$\frac{1}{r \sin\theta} \left[\frac{\partial E_r}{\partial \phi} - \frac{\partial(r \sin\theta E_\phi)}{\partial r} \right] = -i\omega\mu H_\theta \quad (104)$$

$$\frac{1}{r} \left[\frac{\partial(r E_\theta)}{\partial r} - \frac{\partial E_r}{\partial \theta} \right] = -i\omega\mu H_\phi \quad (105)$$

$$\frac{1}{r^2} \frac{\partial(r^2 H_r)}{\partial r} + \frac{1}{r \sin\theta} \frac{\partial(\sin\theta H_\theta)}{\partial \theta} + \frac{1}{r \sin\theta} \frac{\partial H_\phi}{\partial \phi} = 0 \quad (106)$$

$$\frac{1}{r^2} \frac{\partial(r^2 E_r)}{\partial r} + \frac{1}{r \sin\theta} \frac{\partial(\sin\theta E_\theta)}{\partial \theta} + \frac{1}{r \sin\theta} \frac{\partial E_\phi}{\partial \phi} = 0 \quad (107)$$

Mie represented the solution of these equations as a superposition of two linearly independent fields such that

$$E_r \neq 0, H_r = 0 \quad (108)$$

and

$$E_r = 0, H_r \neq 0 \quad (109)$$

Substituting Equation (108) into Equations (101) and (102) gives

$$(\sigma + i\omega\epsilon) E_\theta = -\frac{1}{r} \frac{\partial(r H_\phi)}{\partial r} \quad (110)$$

$$(\sigma + i\omega\epsilon) E_\phi = \frac{1}{r} \frac{\partial(r H_\theta)}{\partial r} \quad (111)$$

Upon substituting these equations in Equations (104) and (105) we obtain

$$\frac{(\sigma + i\omega\epsilon)}{\sin\theta} \frac{\partial E_r}{\partial \phi} = \frac{\partial^2(r H_\theta)}{\partial r^2} + k^2 r H_\theta \quad (112)$$

$$-(\sigma + i\omega\epsilon) \frac{\partial E_r}{\partial \theta} = \frac{\partial^2(r H_\phi)}{\partial r^2} + k^2 r H_\phi \quad (113)$$

where $k^2 = \omega^2 \mu \epsilon - i\omega \mu \sigma$

Similarly, for the relations of Equation (109) a solution to Maxwell's equations can be represented by

$$i\omega \mu H_\theta = \frac{1}{r} \frac{\partial(rE_\phi)}{\partial r} \quad (114)$$

$$i\omega \mu H_\phi = -\frac{1}{r} \frac{\partial(rE_\theta)}{\partial r} \quad (115)$$

and

$$-\frac{i\omega \mu}{\sin \theta} \frac{\partial H_r}{\partial \phi} = \frac{\partial^2(rE_\theta)}{\partial r^2} + k^2 r E_\theta \quad (116)$$

$$i\omega \mu \frac{\partial H_r}{\partial \theta} = \frac{\partial^2(rE_\phi)}{\partial r^2} + k^2 r E_\phi \quad (117)$$

It is not difficult to see that the relationships expressed in Equations (108) and (109) define a complementary pair of Hertz potentials $\vec{\Pi}$ and $\vec{\Pi}^*$ such that

$$\Pi_r \neq 0, \Pi_\theta = \Pi_\phi = 0 \quad (118)$$

and

$$\Pi_r^* \neq 0, \Pi_\theta^* = \Pi_\phi^* = 0 \quad (119)$$

For $\Pi_r \neq 0, \Pi_\theta = \Pi_\phi = 0$ we apply the vector expansions of Equation (98) and (99) to Equations (84) and (85) to obtain

$$E_r = -\frac{1}{r^2 \sin \theta} \frac{\partial(\sin \frac{\partial \Pi_r}{\partial \theta})}{\partial \theta} - \frac{1}{r^2 \sin^2 \theta} \frac{\partial^2 \Pi_r}{\partial \phi^2} \quad (120)$$

$$E_\theta = \frac{1}{r} \frac{\partial^2 \Pi_r}{\partial r \partial \theta} \quad (121)$$

$$H_\phi = \frac{1}{r \sin \theta} \frac{\partial^2 \Pi_r}{\partial r \partial \phi} \quad (122)$$

$$H_r = 0 \quad (123)$$

$$H_\theta = \frac{(\sigma + j\omega\epsilon)}{r \sin\theta} \frac{\partial \Pi_r}{\partial \phi} \quad (124)$$

$$H_\phi = - \frac{(\sigma + j\omega\epsilon)}{r} \frac{\partial \Pi_r}{\partial \theta} \quad (125)$$

If we now substitute from these equations into Equations (112) and (113) we obtain

$$\frac{\partial}{\partial \phi} \left[\frac{\partial^2 \Pi_r}{\partial r^2} + \frac{1}{r^2 \sin\theta} \frac{\partial(\sin\theta \frac{\partial \Pi_r}{\partial \theta})}{\partial \theta} + \frac{1}{r^2 \sin^2\theta} \frac{\partial^2 \Pi_r}{\partial \phi^2} + k^2 \Pi_r \right] = 0 \quad (126)$$

$$\frac{\partial}{\partial \theta} \left[\frac{\partial^2 \Pi_r}{\partial r^2} + \frac{1}{r^2 \sin\theta} \frac{\partial(\sin\theta \frac{\partial \Pi_r}{\partial \theta})}{\partial \theta} + \frac{1}{r^2 \sin^2\theta} \frac{\partial^2 \Pi_r}{\partial \phi^2} + k^2 \Pi_r \right] = 0 \quad (127)$$

The vanishing of the θ and ϕ derivatives may be satisfied by equating the expression within the brackets to zero, which gives

$$\frac{\partial^2 \Pi_r}{\partial r^2} + \frac{1}{r^2 \sin\theta} \frac{\partial(\sin\theta \frac{\partial \Pi_r}{\partial \theta})}{\partial \theta} + \frac{1}{r^2 \sin^2\theta} \frac{\partial^2 \Pi_r}{\partial \phi^2} + k^2 \Pi_r = 0 \quad (128)$$

Comparing this expression with Equation (120) we see that E_r may be written as

$$E_r = \frac{\partial^2 \Pi_r}{\partial r^2} + k^2 \Pi_r \quad (129)$$

In a similar manner for $\Pi_r^* \neq 0$, $\Pi_\theta^* = \Pi_\phi^* = 0$ we apply the vector expansions of Equations (98) and (99) to Equations (88) and (89) to obtain

$$E_r = 0 \quad (130)$$

$$E_\theta = - \frac{j\omega\mu}{r \sin\theta} \frac{\partial \Pi_r^*}{\partial \phi} \quad (131)$$

$$E_{\phi} = \frac{i\omega\mu}{r} \frac{\partial \Pi_r^*}{\partial \theta} \quad (132)$$

$$H_r = -\frac{1}{r^2 \sin \theta} \frac{\partial (\sin \theta \frac{\partial \Pi_r^*}{\partial \theta})}{\partial \theta} - \frac{1}{r^2 \sin^2 \theta} \frac{\partial^2 \Pi_r^*}{\partial \phi^2} \quad (133)$$

$$H_{\theta} = \frac{1}{r} \frac{\partial^2 \Pi_r^*}{\partial r \partial \theta} \quad (134)$$

$$H_{\phi} = \frac{1}{r \sin \theta} \frac{\partial^2 \Pi_r^*}{\partial r \partial \phi} \quad (135)$$

and upon substitution from these expressions into Equations (116) and (117) we obtain

$$\frac{\partial^2 \Pi_r^*}{\partial r^2} + \frac{1}{r^2 \sin \theta} \frac{\partial (\sin \theta \frac{\partial \Pi_r^*}{\partial \theta})}{\partial \theta} + \frac{1}{r^2 \sin^2 \theta} \frac{\partial^2 \Pi_r^*}{\partial \phi^2} + k^2 \Pi_r^* = 0 \quad (136)$$

Consequently,

$$H_r = \frac{\partial^2 \Pi_r^*}{\partial r^2} + k^2 \Pi_r^* \quad (137)$$

Now let $\Pi_r = r\psi$, then Equation (128) becomes

$$\frac{1}{r} \frac{\partial^2 (r\psi)}{\partial r^2} + \frac{1}{r^2 \sin \theta} \frac{\partial (\sin \theta \frac{\partial \psi}{\partial \theta})}{\partial \theta} + \frac{1}{r^2 \sin^2 \theta} \frac{\partial^2 \psi}{\partial \phi^2} + k^2 \psi = 0 \quad (138)$$

and for $\Pi_r^* = r\psi^*$ Equation (136) becomes

$$\frac{1}{r} \frac{\partial^2 (r\psi^*)}{\partial r^2} + \frac{1}{r^2 \sin \theta} \frac{\partial (\sin \theta \frac{\partial \psi^*}{\partial \theta})}{\partial \theta} + \frac{1}{r^2 \sin^2 \theta} \frac{\partial^2 \psi^*}{\partial \phi^2} + k^2 \psi^* = 0 \quad (139)$$

It is obvious that Equation (138) and (139) are only the scalar wave equations

$$\nabla^2 \psi + k^2 \psi = 0 \quad (140)$$

expressed in spherical coordinates.

Both scalar potentials ψ and ψ^* are solutions of Equation (140) and the complete solution of the electromagnetic field is obtained by adding the partial fields derived from ψ and ψ^* . Thus

$$E_r = \frac{\partial^2 r\psi}{\partial r^2} + k^2 r\psi \quad (141)$$

$$E_\theta = \frac{1}{r} \frac{\partial^2 r\psi}{\partial r \partial \theta} - \frac{i\omega\mu}{r \sin\theta} \frac{\partial r\psi^*}{\partial \phi} \quad (142)$$

$$E_\phi = \frac{1}{r \sin\theta} \frac{\partial^2 r\psi}{\partial r \partial \phi} + \frac{i\omega\mu}{r} \frac{\partial r\psi^*}{\partial \theta} \quad (143)$$

$$H_r = \frac{\partial^2 r\psi^*}{\partial r^2} + k^2 r\psi^* \quad (144)$$

$$H_\theta = \frac{1}{r} \frac{\partial^2 r\psi^*}{\partial r \partial \theta} + \frac{(\sigma + i\omega\epsilon)}{r \sin\theta} \frac{\partial r\psi}{\partial \phi} \quad (145)$$

$$H_\phi = \frac{1}{r \sin\theta} \frac{\partial^2 r\psi^*}{\partial r \partial \phi} - \frac{(\sigma + i\omega\epsilon)}{r} \frac{\partial r\psi}{\partial \theta} \quad (146)$$

Thus the problem of integrating Maxwell's equations has now been reduced to the problem of finding two mutually independent solutions of the scalar wave equation evaluated so as to satisfy the boundary conditions.

It is easily verified that these relations satisfy Maxwell's equations.

Many solutions of the scalar wave equation in spherical coordinates are available [Refs. 6, 35, 53, 54] and the discussion presented here will be based partially on Stratton's [Ref. 53] treatment. Equation (138) is the scalar wave equation in spherical coordinates, and since it is separable in the spherical coordinates r , θ and ϕ , integral solutions exist of the form

$$\psi = R(r) T(\theta) P(\phi) \quad (147)$$

where

$R(r)$ = a function of r only

$T(\theta)$ = a function of θ only

$P(\phi)$ = a function of ϕ only

Substituting this expression into Equation (138), we obtain

$$\frac{TP}{r} \frac{d^2(rR)}{dr^2} + \frac{RP}{r^2 \sin^2 \theta} \frac{d(\sin \theta \frac{dT}{d\theta})}{d\theta} + \frac{RT}{r^2 \sin^2 \theta} \frac{d^2 P}{d\phi^2} + k^2 RTP = 0 \quad (148)$$

Dividing by $\psi = RTP$ and multiplying by r^2 gives

$$\frac{r}{R} \frac{d^2(rR)}{dr^2} + \frac{1}{\sin^2 \theta} \frac{d(\sin \theta \frac{dT}{d\theta})}{d\theta} + \frac{1}{\sin^2 \theta} \frac{d^2 P}{d\phi^2} + k^2 r^2 = 0 \quad (149)$$

Now, setting all terms that are a function only of r equal to a constant, α^2 , we get

$$\frac{r}{R} \frac{d^2(rR)}{dr^2} + k^2 r^2 = \alpha^2 \quad (150)$$

and

$$r \frac{d^2(rR)}{dr^2} + (k^2 r^2 - \alpha^2) R = 0 \quad (151)$$

$$\text{If we let } \alpha^2 = n(n+1) \quad n = \text{an integer} \quad (152)$$

$$x = kr \quad (153)$$

$$\text{then } dx = kdr \quad (154)$$

and upon substituting these relations in Equation (151) we obtain

$$x^2 \frac{d^2 R}{dx^2} + 2x \frac{dR}{dx} + [x^2 - n(n+1)] R = 0 \quad (155)$$

Now, if we make the substitution $R = x^{-1/2} y$, Equation (155) becomes

$$x^2 \frac{d^2 y}{dx^2} + x \frac{dy}{dx} + [x^2 - n(n+1) - \frac{1}{4}] y = 0 \quad (156)$$

or

$$x^2 \frac{d^2 y}{dx^2} + x \frac{dy}{dx} + [x^2 - n(n + \frac{1}{2})^2] y = 0 \quad (157)$$

which is known in the literature as Bessel's differential equation of order $n + 1/2$.

The general solution is of the form

$$y = U J_{n+1/2}(x) + V N_{n+1/2}(x) \quad (158)$$

Now, since $R = x^{-1/2} y$ and $x = kr$, the general integral of Equation (151) becomes

$$R = \frac{U}{\sqrt{kr}} J_{n+1/2}(kr) + \frac{V}{\sqrt{kr}} N_{n+1/2}(kr) \quad (159)$$

where $J_{n+1/2}(kr)$ = Bessel function of the first kind

$N_{n+1/2}(kr)$ = Bessel function of the second kind

sometimes called the Neumann function

We can find an alternate solution in terms of spherical Bessel functions [Ref. 35] such that

$$R = u j_n(kr) + v n_n(kr) \quad (160)$$

where

$$j_n(kr) = \sqrt{\frac{\pi}{2kr}} J_{n+1/2}(kr)$$

$$n_n(kr) = -\sqrt{\frac{\pi}{2kr}} N_{n+1/2}(kr)$$

Now, by substituting Equation (150) into Equation (149) and upon multiplying the resultant expression by $\sin^2 \theta$, we obtain

$$\frac{\sin \theta}{T} \frac{d(\sin \theta \frac{dT}{d\theta})}{d\theta} + \frac{1}{P} \frac{d^2 P}{d\phi^2} + \alpha^2 \sin^2 \theta = 0 \quad (161)$$

The relationship expressed by this equation can be satisfied only if the second term is constant, i.e.

$$\frac{1}{P} \frac{d^2 P}{d\phi^2} = -m^2 \quad (162)$$

where m^2 is a constant. A single-valued solution of the form

$$P = a_m \cos(m\phi) + b_m \sin(m\phi) \quad (163)$$

exists over the range $0 \leq \phi \leq 2\pi$ for m an integer such that $n > |m|$

where $\alpha^2 = n(n+1)$.

Substituting Equation (162) into Equation (161) and multiplying by $T/\sin^2\theta$ gives

$$\frac{d^2 T}{d\theta^2} + \frac{1}{\tan\theta} \frac{dT}{d\theta} + \left(\alpha^2 - \frac{m^2}{\sin^2\theta} \right) T = 0 \quad (164)$$

which is known as the associated Legendre equation. The general solution is

$$T = f_n P_n^m(\cos\theta) + g_n Q_n^m(\cos\theta) \quad (165)$$

where $P_n^m(\cos\theta)$ = associated Legendre function of the first kind

$Q_n^m(\cos\theta)$ = associated Legendre function of the second kind

$Q_n^m(\cos\theta)$ has a singularity at the poles $\theta = 0$ and π ; consequently, since the fields exist at these poles, an associated Legendre function of the second kind does not apply to our problem. Therefore, g_n must equal zero and Equation (165) reduces to

$$T = f_n P_n^m(\cos\theta) \quad (166)$$

which vanishes for $|m| > n$.

Therefore, the general solution of the scalar wave equation can be

written as

$$\psi(r, \theta, \phi) = \sum_{n=0}^{\infty} \sum_{m=-n}^n [a_m \cos(m\phi) + b_m \sin(m\phi)] [C_n j_n(kr) + d_n N_n(kr)] [P_n^m(\cos\theta)] \quad (167)$$

where a_m , b_m , c_n and d_n are arbitrary constants.

We are now prepared to derive Mie's formulae assuming the incident radiation is linearly polarized with the x-axis in the plane of the electric field vector and the direction of propagation along the positive z axis. The origin is taken at the center of the sphere of radius a. We designate the medium surrounding the sphere as medium 1 defined by σ_1 , ϵ_1 , μ_1 and k_1 ; and the sphere is designated as medium 2 defined by σ_2 , ϵ_2 , μ_2 and k_2 . Thus, the incident linearly polarized radiation is defined as

$$E_x = E_0 e^{i(\omega t + k_1 z)} \quad (168)$$

$$H_y = H_0 e^{i(\omega t + k_1 z)} \quad (169)$$

$$E_y = E_z = H_x = H_z = 0 \quad (170)$$

We can immediately calculate the relationship between E_x and H_y from Maxwell's equations, i.e.

$$\frac{\partial E_x}{\partial z} = -\mu_1 \frac{\partial H_y}{\partial t} \quad (171)$$

Thus,

$$H_y = -\frac{ik_1}{i\omega\mu_1} E_x \quad (172)$$

For convenience, let

$$\alpha = \sigma + i\omega\epsilon \quad (173)$$

$$\beta = -i\omega\mu \quad (174)$$

where

$$k^2 = \alpha\beta = \omega^2\mu\sigma - i\omega\mu\sigma \quad (175)$$

Then H_y may be expressed as

$$H_y = \frac{ik_1}{\beta_1} E_0 e^{i(\omega t + k_1 z)} \quad (176)$$

Now, it is necessary to express E_x and H_y in terms of spherical coordinates. To transform any vector

$$\vec{A} = A_x \vec{a}_x + A_y \vec{a}_y + A_z \vec{a}_z \quad (177)$$

in the Cartesian coordinate system to the spherical coordinate system.

$$\vec{A} = A_r \vec{a}_r + A_\theta \vec{a}_\theta + A_\phi \vec{a}_\phi \quad (178)$$

we represent the position vector of any point as

$$\rho = x\vec{a}_x + y\vec{a}_y + z\vec{a}_z \quad (179)$$

substituting Equations (95) through (97) into Equation (179) gives

$$\rho = r\sin\theta\cos\phi\vec{a}_x + r\sin\theta\sin\phi\vec{a}_y + r\cos\theta\vec{a}_z \quad (180)$$

In the spherical coordinate system the unit vectors are defined as

$$\vec{a}_r = \frac{\frac{\partial \rho}{\partial r}}{\left| \frac{\partial \rho}{\partial r} \right|} = \sin\theta\cos\phi\vec{a}_x + \sin\theta\sin\phi\vec{a}_y + \cos\theta\vec{a}_z \quad (181)$$

$$\vec{a}_\theta = \frac{\frac{\partial \rho}{\partial \theta}}{\left| \frac{\partial \rho}{\partial \theta} \right|} = \cos\theta\cos\phi\vec{a}_x + \cos\theta\sin\phi\vec{a}_y - \sin\theta\vec{a}_z \quad (182)$$

$$\vec{a}_\phi = \frac{\frac{\partial \rho}{\partial \phi}}{\left| \frac{\partial \rho}{\partial \phi} \right|} = -\sin\phi\vec{a}_x + \cos\phi\vec{a}_y \quad (183)$$

Then solving these equations simultaneously for the unit vectors in the Cartesian system gives

$$\vec{a}_x = \sin\theta\cos\phi\vec{a}_r + \cos\theta\cos\phi\vec{a}_\theta - \sin\phi\vec{a}_\phi \quad (184)$$

$$\vec{a}_y = \sin\theta\sin\phi\vec{a}_r + \cos\theta\sin\phi\vec{a}_\theta + \cos\phi\vec{a}_\phi \quad (185)$$

$$\vec{a}_z = \cos\theta\vec{a}_r - \sin\theta\vec{a}_\theta \quad (186)$$

Substituting Equations (184) through (186) into Equation (177) we see that any vector \vec{A} expressed in the Cartesian coordinate system can be transformed to the spherical coordinate system according to

$$\begin{aligned} \vec{A} = & (A_x\sin\theta\cos\phi + A_y\sin\theta\sin\phi + A_z\cos\theta) \vec{a}_r \\ & + (A_x\cos\theta\cos\phi + A_y\cos\theta\sin\phi - A_z\sin\theta) \vec{a}_\theta \\ & + (-A_x\sin\phi + A_y\cos\phi) \vec{a}_\phi \end{aligned} \quad (187)$$

Thus, the components of the incident field can be expressed in the spherical coordinate system as

$$E_r = E_o e^{i(\omega t + k_1 r \cos\theta)} \sin\theta\cos\phi \quad (188)$$

$$E_\theta = E_o e^{i(\omega t + k_1 r \cos\theta)} \cos\theta\cos\phi \quad (189)$$

$$E_\phi = -E_o e^{i(\omega t + k_1 r \cos\theta)} \sin\phi \quad (190)$$

$$H_r = E_o \frac{ik_1}{\beta_1} e^{i(\omega t + k_1 r \cos\theta)} \sin\theta\sin\phi \quad (191)$$

$$H_\theta = E_o \frac{ik_1}{\beta_1} e^{i(\omega t + k_1 r \cos\theta)} \cos\theta\sin\phi \quad (192)$$

$$H_\phi = E_o \frac{ik_1}{\beta_1} e^{i(\omega t + k_1 r \cos\theta)} \cos\phi \quad (193)$$

Since these equations represent the total field, it is necessary to use Equation (141) through (146) to evaluate the scalar potentials ψ and ψ^* for the incident wave. For convenience in computation we choose

to work with Equation (141), i.e.

$$E_r = \frac{\partial^2 r\psi}{\partial r^2} + k^2 r\psi \quad (141)$$

Substituting for E_r from Equation (188) gives

$$E_o e^{i(\omega t + k_1 r \cos \theta)} \sin \theta \cos \phi = \frac{\partial^2 r\psi}{\partial r^2} + k_1^2 r\psi \quad (194)$$

Now, applying Bauer's formula [Ref. 55]

$$e^{i r \cos \theta} = \sum_{n=0}^{\infty} i^n (2n+1) j_n(r) P_n(\cos \theta) \quad (195)$$

we obtain

$$e^{i k_1 r \cos \theta} = \sum_{n=0}^{\infty} i^n (2n+1) j_n(k_1 r) P_n(\cos \theta) \quad (196)$$

If we differentiate this expression with respect to θ , i.e.

$$\frac{\partial}{\partial \theta} e^{i k_1 r \cos \theta} = \frac{\partial}{\partial \theta} \sum_{n=0}^{\infty} i^n (2n+1) J_n(k_1 r) P_n(\cos \theta) \quad (197)$$

we obtain

$$e^{i k_1 r \cos \theta} \sin \theta = \frac{1}{i k_1 r} \sum_{n=1}^{\infty} i^n (2n+1) J_n(k_1 r) P_n^{(1)}(\cos \theta) \quad (198)$$

where the associated Legendre functions of the first kind are defined in terms of the Legendre functions of the first kind by

$$P_n^m(\cos \theta) = \sin^m \theta \frac{d^m P_n(\cos \theta)}{d(\cos \theta)^m} \quad (199)$$

Thus, it can be readily verified that

$$\frac{dP_n(\cos \theta)}{d\theta} = -P_n^{(1)}(\cos \theta) \quad (200)$$

Now, E_r can be expressed as

$$E_r = E_o e^{i(\omega t + k_1 r \cos \theta)} \sin \theta \cos \phi =$$

$$E_o e^{i\omega t} \frac{\cos \phi}{k_1 r} \sum_{n=1}^{\infty} i^{n-1} (2n+1) j_n(k_1 r) P_n^{(1)}(\cos \theta) \quad (201)$$

Assuming a similar form for ψ , i.e.,

$$\psi = E_o e^{i\omega t} \frac{\cos \phi}{k_1} \sum_{n=1}^{\infty} K_n j_n(k_1 r) P_n^{(1)}(\cos \theta) \quad (202)$$

we obtain upon substituting it and Equation (201) into Equation (194) the relation

$$r \frac{\partial^2 j_n(k_1 r)}{\partial r^2} + [k_1^2 r^2 - \frac{i^{n-1} (2n+1)}{K_n}] j_n(k_1 r) = 0 \quad (203)$$

which is nothing but Bessel's equation where

$$K_n = i^{n-1} \frac{(2n+1)}{n(n+1)} \quad (204)$$

Therefore, for the incident wave the scalar electric potential is given by

$$\psi_i = \frac{E_o e^{i\omega t} \sin \phi}{k_1} \sum_{n=1}^{\infty} i^{n-1} \frac{(2n+1)}{n(n+1)} j_n(k_1 r) P_n^{(1)}(\cos \theta) \quad (205)$$

and similarly, for the magnetic potential

$$\psi_i^* = \frac{E_o e^{i\omega t} \sin \phi}{k_1} \sum_{n=1}^{\infty} i^n \frac{k_1}{8_1} \frac{(2n+1)}{n(n+1)} j_n(k_1 r) P_n^{(1)}(\cos \theta) \quad (206)$$

To determine the scalar field potentials for the scattered wave and for the wave within the sphere, it is necessary to determine the arbitrary constants of Equation (167) in such a way as to satisfy the boundary conditions and the conditions at the origin (center of the sphere) and at infinity. The conditions to be satisfied, then, are

a. The field within the sphere must be finite at the origin.

Since the spherical Bessel function of the second kind, $n_n(kr)$, has a singularity at $r = 0$ and becomes infinite there, $d_n = 0$ for the region within the sphere.

b. The scattered field must vanish at infinity. The function

$$n_n^{(2)}(kr) = j_n(kr) - i n_n(kr) = \sqrt{\frac{\pi}{2kr}} H_{n+1/2}^{(2)}(kr) \quad (207)$$

is known as the Hankel function of type 2 (or Bessel function of the third kind) and has the property that it vanishes at infinity. Therefore,

$c_n = 1$ and $d_n = -i$ in the solution of the scattered wave.

c. The required boundary conditions are that the tangential components of the electric field vector and the magnetic field vector must be continuous across the surface of the sphere, i.e., at $r = a$

$$E_{\theta 1} = E_{\theta 2} \quad (208)$$

$$E_{\phi 1} = E_{\phi 2} \quad (209)$$

$$H_{\theta 1} = H_{\theta 2} \quad (210)$$

$$H_{\phi 1} = H_{\phi 2} \quad (211)$$

If we assume that the form used to represent the incident wave dictates the form of the complete solution, then the scattered wave and the field within the sphere can be represented by the following scalar potentials:

a. Scattered wave outside of sphere

$$\psi_s = \frac{E_0 e^{i\omega t} \cos\phi}{k_1} \sum_{n=1}^{\infty} a_n h_n^{(2)}(k_1 r) P_n^{(1)}(\cos\theta) \quad (212)$$

$$\psi_s^* = \frac{E_o e^{i\omega t} \sin\phi}{k_1} \sum_{n=1}^{\infty} b_n \frac{ik_1}{\beta_1} h_n^{(2)}(k_1 r) P_n^{(1)}(\cos\theta) \quad (213)$$

b. Wave within the sphere

$$\psi_o = \frac{E_o e^{i\omega t} \cos\phi}{k_2} \sum_{n=1}^{\infty} w_n j_n(k_2 r) P_n^{(1)}(\cos\theta) \quad (214)$$

$$\psi_o^* = \frac{E_o e^{i\omega t} \sin\phi}{k_2} \sum_{n=1}^{\infty} x_n \frac{ik_2}{\beta_2} j_n(k_2 r) P_n^{(1)}(\cos\theta) \quad (215)$$

Now since we know that the total field outside the sphere is equal to the sum of the incident field and the scattered field, we apply the boundary conditions to Equations (142), (143), (145) and (146) to obtain

$$\frac{\partial r(\psi_i + \psi_s)}{\partial r} = \frac{\partial r\psi_o}{\partial r} \quad (216)$$

$$\frac{\partial r(\psi_i^* + \psi_s^*)}{\partial r} = \frac{\partial r\psi_o^*}{\partial r} \quad (217)$$

$$\alpha_1 [r(\psi_i + \psi_s)] = \alpha_2 (r\psi_o) \quad (218)$$

$$\beta_1 [r(\psi_i^* + \psi_s^*)] = \beta_2 (r\psi_o^*) \quad (219)$$

which are valid only at $r = a$. Upon substituting Equations (205) and (206) and Equations (212) through (215) into these boundary conditions where the derivatives of Bessel's and Hankel's functions are denoted by primes:

$$i^{n-1} \frac{(2n+1)}{n(n+1)} \frac{1}{k_1} j_n'(k_1 a) + a_n \frac{1}{k_1} h_n^{(2)'}(k_1 a) = w_n \frac{1}{k_2} j_n'(k_2 a) \quad (220)$$

$$i^n \frac{(2n+1)}{n(n+1)} \frac{1}{\beta_1} j_n'(k_1 a) + b_n \frac{1}{\beta_1} h_n^{(2)'}(k_1 a) = x_n \frac{1}{\beta_2} j_n'(k_2 a) \quad (221)$$

$$i^{n-1} \frac{(2n+1)}{n(n+1)} \frac{\alpha_1}{k_1} j_n(k_1 a) + a_n \frac{\alpha_1}{k_1} h_n^{(2)}(k_1 a) = w_n \frac{\alpha_2}{k_2} j_n(k_2 a) \quad (222)$$

$$i^n \frac{(2n+1)}{n(n+1)} j_n(k_1 a) + b_n i h_n^{(2)}(k_1 a) = x_n i j_n(k_2 a) \quad (223)$$

Upon eliminating w_n from the first and third equations and x_n from the remaining pair we obtain the following expressions for a_n and b_n :

$$a_n = i^{n-1} \frac{2n+1}{n(n+1)} \frac{\alpha_1 j_n(k_1 a) j_n'(k_2 a) - \alpha_2 j_n(k_2 a) j_n'(k_1 a)}{\alpha_2 j_n(k_2 a) h_n^{(2)}(k_1 a) - \alpha_1 j_n'(k_2 a) h_n^{(2)}(k_1 a)} \quad (224)$$

$$b_n = i^{n-1} \frac{2n+1}{n(n+1)} \frac{\beta_1 j_n(k_1 a) j_n'(k_2 a) - \beta_2 j_n(k_2 a) j_n'(k_1 a)}{\beta_2 j_n(k_2 a) h_n^{(2)}(k_1 a) - \beta_1 j_n'(k_2 a) h_n^{(2)}(k_1 a)} \quad (225)$$

Similarly,

$$w_n = i^{n-1} \frac{2n+1}{n(n+1)} \frac{k_2 \alpha_1 j_n'(k_1 a) h_n^{(2)}(k_1 a) - k_2 \alpha_1 j_n(k_1 a) h_n^{(2)}(k_1 a)}{k_1 \alpha_1 j_n'(k_2 a) h_n^{(2)}(k_1 a) - k_2 \alpha_2 j_n(k_2 a) h_n^{(2)}(k_1 a)} \quad (226)$$

$$x_n = i^{n-1} \frac{2n+1}{n(n+1)} \frac{\beta_2 j_n'(k_1 a) h_n^{(2)}(k_1 a) - \beta_2 j_n(k_1 a) h_n^{(2)}(k_1 a)}{\beta_1 j_n'(k_2 a) h_n^{(2)}(k_1 a) - \beta_2 j_n(k_2 a) h_n^{(2)}(k_1 a)} \quad (227)$$

We have now determined the unknown constants of Mie's problem and we can finally calculate the field at any point inside or outside the sphere. For our problem we are only interested in the behavior of the scattered wave and on substituting Equation (212) and (213) into Equations (141) through (146) we can derive expressions for the components of the field vectors of the scattered wave. In deriving the radial components, E_r and H_r , it is necessary to evaluate the first and second derivatives of Equation (207) and while it is a tedious job, the use of the following recurrence formulas readily facilitate the calculations:

$$a. \frac{dJ_x(y)}{dy} = \frac{x}{y} J_x(y) - J_{x+1}(y) \quad (228)$$

$$b. \frac{dJ_x(y)}{dy} = -\frac{x}{y} J_x(y) + J_{x-1}(y) \quad (229)$$

where $J_x(y)$ = Bessel function of the first, second or third kind of order

x (may be fractional, integral or complex) and argument y

Thus, we obtain the following expressions for the radial components of the field:

$$E_r = \frac{E_0 e^{i\omega t} \cos\phi}{k_1 r^2} \sum_{n=1}^{\infty} n(n+1) a_n h_n^{(2)}(k_1 r) P_n^{(1)}(\cos\theta) \quad (230)$$

$$H_r = \frac{iE_0 e^{i\omega t} \sin\phi}{\beta_1 r^2} \sum_{n=1}^{\infty} n(n+1) b_n h_n^{(2)}(k_1 r) P_n^{(1)}(\cos\theta) \quad (231)$$

In deriving the tangential components of the field it is convenient to make the substitution

$$z_n^{(2)}(k_1 z) = \sqrt{\frac{\pi k_1 r}{2}} H_{n+1/2}^{(2)}(k_1 r) \quad (232)$$

This gives

$$E_\theta = -\frac{E_0 e^{i\omega t} \cos\phi}{k_1 r} \left[\sum_{n=1}^{\infty} a_n z_n^{(2)}(k_1 r) P_n^{(1)}(\cos\theta) \sin\theta - i b_n z_n^{(2)}(k_1 r) P_n^{(1)}(\cos\theta) \frac{1}{\sin\theta} \right] \quad (233)$$

$$E_\phi = -\frac{E_0 e^{i\omega t} \sin\phi}{k_1 r} \left[\sum_{n=1}^{\infty} a_n z_n^{(2)}(k_1 r) P_n^{(1)}(\cos\theta) \frac{1}{\sin\theta} - i b_n z_n^{(2)}(k_1 r) P_n^{(1)}(\cos\theta) \sin\theta \right] \quad (234)$$

$$H_{\theta} = - \frac{E_0 e^{i\omega t} \sin\phi}{\beta_1 r} \left[\sum_{n=1}^{\infty} a_n z_n^{(2)}(k_1 r) P_n^{(1)}(\cos\theta) \frac{1}{\sin\theta} \right. \\ \left. + i b_n z_n^{(2)}(k_1 r) P_n^{(1)}(\cos\theta) \sin\theta \right] \quad (235)$$

$$H_{\phi} = \frac{E_0 e^{i\omega t} \cos\phi}{\beta_1 r} \left[\sum_{n=1}^{\infty} a_n z_n^{(2)}(k_1 r) P_n^{(1)}(\cos\theta) \sin\theta \right. \\ \left. + i b_n z_n^{(2)}(k_1 r) P_n^{(1)}(\cos\theta) \frac{1}{\sin\theta} \right] \quad (236)$$

The primes denote the derivative of a function with respect to its argument. We have now completed the solution of Mie's problem. While the solution was derived for a single sphere, the results apply to any optically thin medium containing many spherical particles of the same composition and of the same or different sizes if the distance between particles is large compared to the wavelength of the incident radiation. We can then assume that there is no multiple scattering and, therefore, the total intensity scattered is equal to the sum of the intensities scattered by each particle.

In summary, we have derived the formulas for the electric and magnetic field components which describe the scattered field arising from a linearly polarized monochromatic plane wave incident upon a spherical particle of arbitrary composition and size. We see from Equations (230) and (231) that in the far field (i.e., at distances very much greater than the wavelength of the incident radiation) the radial components of the scattered wave vanish as the inverse square of the distance from the origin, while the tangential components diminish as the inverse of the distance. Thus in the far field the

radial components may be neglected in comparison with the tangential components and the fields can, therefore, be assumed to be transverse to the direction of propagation. Furthermore, the scattered radiation from the sphere is, in general, elliptically polarized except in the planes of scattering defined by $\phi = 0$ and $\phi = \frac{\pi}{2}$, i.e. the xz and the yz planes. We see from Equations (233) and (234) that E_ϕ vanishes for $\phi = 0$ and, alternately, $E_\theta = 0$ for $\phi = \frac{\pi}{2}$; consequently, the scattered radiation is linearly polarized for all scattering angles, θ , when the plane of scattering is parallel or perpendicular to the electric field vector. This polarization characteristic provides the basis for the cloud/target discrimination technique described in the next chapter.

3.3 APPLICATION OF MIE THEORY TO ATMOSPHERIC AEROSOLS

Many investigators have considered the consequences of Mie's theory in terms of the physical parameters, such as the wavelength of the incident radiation, the index of refraction of the sphere and the surrounding medium, the composition, density, size and size distribution of the scattering particles, etc. In addition, there is an immense amount of literature on the application of the theory to other fields of research. We, therefore, refer the reader interested in a complete coverage of the theory and all of its aspects to the publications already referenced. For purposes of our research we are primarily interested in the extinction coefficient, σ , and the angular volume scattering coefficient, $\beta(\theta)$ defined as the ratio of the flux scattered into a unit solid angle by a unit volume of a homogeneous medium containing particles of different radii in the direction θ , to the flux incident on the unit cross section of this volume.

Both σ and $\beta(\theta)$ are defined mathematically for the far field where the spherical Bessel function $h_n^{(2)}(kr)$ converges very rapidly for large values of its argument and can, therefore, be approximated by

$$h_n^{(2)}(kr) \approx \frac{i^{n+1}}{kr} e^{-ikr} \quad (237)$$

Substituting this expression into Equations (212) and (213) gives

$$\psi_s = \frac{iE_o e^{i(\omega t - k_1 r)} \cos\phi}{k_1^2 r} \sum_{n=1}^{\infty} i^{n+1} a_n P_n^{(1)}(\cos\theta) \quad (238)$$

$$\psi_s^* = \frac{iE_o e^{i(\omega t - k_1 r)} \sin\phi}{k_1 \beta_1 r} \sum_{n=1}^{\infty} i^{n+1} b_n P_n^{(1)}(\cos\theta) \quad (239)$$

and accordingly the tangential field components become

$$E_\theta = \frac{iE_o e^{i(\omega t - k_1 r)} \cos\phi}{k_1 r} \left\{ \sum_{n=1}^{\infty} i^{n+1} [a_n P_n^{(1)}(\cos\theta) \sin\theta + b_n P_n^{(1)}(\cos\theta) \frac{1}{\sin\theta}] \right\} \quad (240)$$

$$E_\phi = \frac{iE_o e^{i(\omega t - k_1 r)} \sin\phi}{k_1 r} \left\{ \sum_{n=1}^{\infty} i^{n+1} [a_n P_n^{(1)}(\cos\theta) \frac{1}{\sin\theta} + b_n P_n^{(1)}(\cos\theta) \sin\theta] \right\} \quad (241)$$

$$H_\theta = - \frac{E_o e^{i(\omega t - k_1 r)} \sin\phi}{\beta_1 r} \left\{ \sum_{n=1}^{\infty} i^{n+1} [a_n P_n^{(1)}(\cos\theta) \frac{1}{\sin\theta} + b_n P_n^{(1)}(\cos\theta) \sin\theta] \right\} \quad (242)$$

$$H_\phi = \frac{E_o e^{i(\omega t - k_1 r)} \cos\phi}{\beta_1 r} \left\{ \sum_{n=1}^{\infty} i^{n+1} [a_n P_n^{(1)}(\cos\theta) \sin\theta + b_n P_n^{(1)}(\cos\theta) \frac{1}{\sin\theta}] \right\} \quad (243)$$

Now, Equations (240) and (243) can be rewritten as

$$E_\theta = \frac{iE_o e^{i(\omega t - k_1 r)} \cos\phi}{k_1 r} \{A_{II}(\theta)\} \quad (244)$$

$$E_{\phi} \approx \frac{iE_0 e^{i(\omega t - k_1 r)} \cos \phi}{k_1 r} \{A_{\perp}(\theta)\} \quad (245)$$

$$H_{\theta} \approx - \frac{E_0 e^{i(\omega t - k_1 r)} \sin \phi}{\beta_1 r} \{A_{\perp}(\theta)\} \quad (246)$$

$$H_{\phi} \approx \frac{E_0 e^{i(\omega t - k_1 r)} \sin \phi}{\beta_1 r} \{A_{\parallel}(\theta)\} \quad (247)$$

where $A_{\parallel}(\theta)$ and $A_{\perp}(\theta)$ are called amplitude functions and are equal to

$$A_{\parallel}(\theta) = \sum_{n=1}^{\infty} i^{n+1} [b_n \xi_n(\cos \theta) - a_n \zeta_n(\cos \theta)] \quad (248)$$

$$A_{\perp}(\theta) = \sum_{n=1}^{\infty} i^{n+1} [a_n \xi_n(\cos \theta) - b_n \zeta_n(\cos \theta)] \quad (249)$$

where we let

$$\zeta_n(\cos \theta) = \frac{dP_n^{(1)}(\cos \theta)}{d\theta} = -\sin \theta \frac{dP_n^{(1)}(\cos \theta)}{d(\cos \theta)} \quad (250)$$

$$\xi_n(\cos \theta) = P_n^{(1)}(\cos \theta) \frac{1}{\sin \theta} \quad (251)$$

We introduce the intensity functions, i_{\parallel} and i_{\perp} , defined by Mie to be

$$i_{\parallel} = |A_{\parallel}(\theta)|^2 \quad (252)$$

$$i_{\perp} = |A_{\perp}(\theta)|^2 \quad (253)$$

where i_{\parallel} is proportional to the angular component of the scattered field whose electric vector is in the plane of scattering and i_{\perp} is proportional to the component whose electric vector is perpendicular to the plane of scattering.

We now state without proof the expression for the angular volume scattering coefficient $\beta(\theta)$ for a medium containing spherical particles

of different radii

$$\beta(\theta) = \frac{\lambda^2}{8\pi^2} \sum_a N(a) \Delta a (i_{||} + i_{\perp}) \quad (254)$$

and the extinction coefficient assuming negligible absorption, i.e.,

$\sigma_s = \sigma$, is obtained by integrating this expression over all directions;

thus

$$\sigma_s = \int_0^{2\pi} \int_0^{\pi} \beta(\theta) \sin\theta d\theta d\phi \quad (255)$$

$$= 2\pi \int_0^{\pi} \beta(\theta) \sin\theta d\theta \quad (256)$$

SECTION IV

THE DERIVATION OF THE CLOUD/TARGET POLARIZATION DISCRIMINATION TECHNIQUE

4.1 QUALITATIVE DESCRIPTION OF THE DISCRIMINATION TECHNIQUE

The general solution for the scattered fields (includes refracted, reflected, and diffracted fields) arising from an electromagnetic wave incident on a smooth (plane) interface between two media is well-known and in the preceeding chapter we discussed an exact solution for one such problem. On the other hand, neither a general nor an exact solution has been determined as yet for similar problems involving a rough interface between media where "rough interface" is defined as a surface that will diffusely scatter the radiation of an incident plane wave. Correspondingly, then, a smooth interface is defined as a surface that will reflect the incident radiation specularly. The degree of roughness (or smoothness) is dependent on the wavelength and angle of incidence of the incident radiation, and can be described in terms of a widely accepted roughness criterion attributed to Lord Rayleigh. Briefly stated, Rayleigh's roughness criterion arbitrarily considers a surface to be smooth if either the ratio

$$\frac{t}{\lambda} \rightarrow 0 \quad (257)$$

or the angle of incidence, γ , measured from the normal to the surface approaches 0, i.e.,

$$\gamma \rightarrow 0 \quad (258)$$

where λ is the wavelength of the incident radiation and t is the height of the surface irregularities (See Fig. 2).

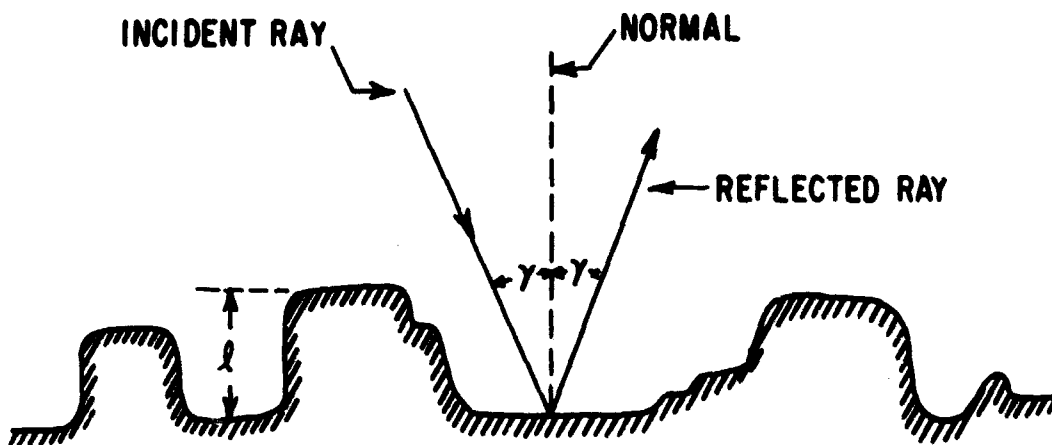


Figure 2. Geometry for Rayleigh's Roughness Criterion

While the general problem of describing the amplitude and phase relationships of the field components reflected from rough surfaces has received considerable attention from several writers, very little effort has been devoted to determining whether or not the polarization of the scattered wave is the same as that of the incident wave. A thorough treatment of rough-surface scattering is beyond the scope of this paper and the reader is referred to Beckmann and Spizzichino's book [Ref. 4] for a clear and comprehensive discussion. They have shown that, in general, the scattered wave arising from an arbitrarily polarized plane wave, incident on an arbitrarily inclined rough surface of arbitrary conductivity whose radii of curvature is large compared to the wavelength, will be depolarized.

We have now discussed the resultant phenomenon arising from the interaction of a linearly polarized, monochromatic electromagnetic plane wave incident on (1) a homogeneous medium containing a size distribution of spherical particles the radii of which are on the same order of magnitude as the wavelength of the incident radiation, and (2) an arbitrarily inclined rough surface of arbitrary conductivity as defined by Rayleigh's roughness criterion. For the first case the Mie theory of scattering shows that in the far field ($r \gg \lambda$) the scattered radiation in planes either parallel or perpendicular to the electric field vector of the incident wave is linearly polarized for all scattering angles. And for the second case Beckmann and Spizzichino have shown that, in general, the scattered radiation will be depolarized if the radius of curvature of the surface variations is comparable to the wavelength of the incident radiation.

As we discussed in Section I the primary limitation to the use of the laser in many atmospheric applications is the severe path loss due to absorption by atmospheric gases and/or scattering by cloud and fog particles. Furthermore, in detection and ranging applications the cloud and fog particles may scatter the transmitted radiation toward the receiver, thus producing a false return which must be distinguished from the target return. It is this latter situation that we are most concerned with, i.e., the problem of distinguishing between a cloud return and a target return. Since the majority of useful lasers emit radiation in the visible or near infrared portion of the electromagnetic spectrum, atmospheric clouds or fogs actually represent Mie scattering media and most targets — earth terrain including man-made irregularities, airborne objects such as aircraft, etc., — can be considered to have rough surfaces at these wavelengths. It is obvious, then, that one possible method of distinguishing a cloud return from a target return could be based on the difference in the polarization characteristics of each return.

A qualitative description of a possible cloud/target polarization discrimination technique is illustrated in Fig. 3. The output of the laser is plane polarized with the plane of vibration of its electric vector (represented by the dots) perpendicular to the page and a direction of propagation as illustrated. A polarizer is placed at the receiver input that will transmit only those components whose electric vectors (represented by the arrows) vibrate at right angles to the direction of the electric vector of the transmitted wave and will eliminate those that vibrate parallel to this direction. When used in this

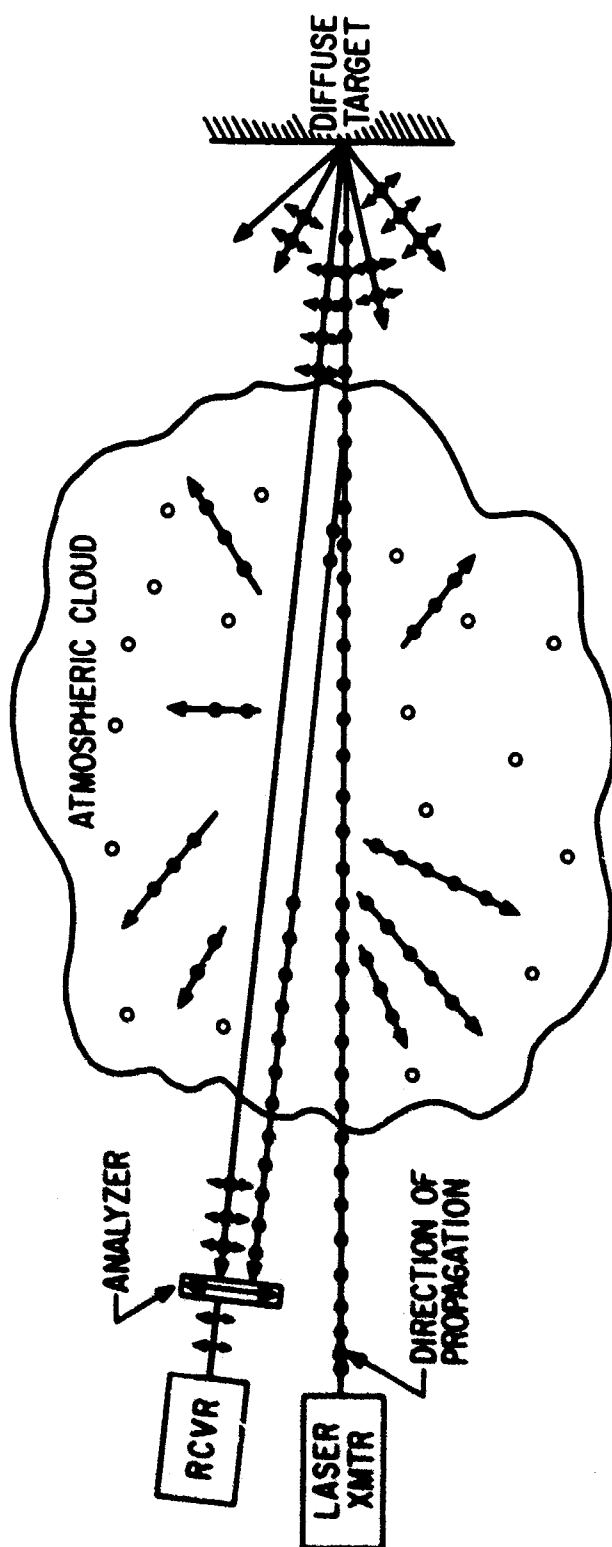


Figure 3. Qualitative Illustration of the Cloud/Target Polarization Discrimination Technique

manner the polarizer is usually called an analyzer. We see then that, according to the Mie theory of scattering, those portions of the transmitted wave that are scattered by the spherical cloud particles are of the same polarization as the transmitted wave. The radiation reflected from a diffuse target, however, is depolarized (represented as a combination of a dot and an arrow) according to the rough surface theory of scattering. We assume that any depolarization effects due to multiple scattering are negligible. Therefore, the receiver will "see" only those components of the radiation reflected from the target whose electric vectors vibrate at right angles to the electric vector of the transmitted wave while all returns due to scattering from cloud particles will be eliminated by the analyzer. We use the term "eliminated" to arbitrarily represent the attenuation of optical energy by any one of the processes of absorption, reflection, refraction, or scattering.

4.2 MATHEMATICAL DERIVATION OF THE DISCRIMINATION TECHNIQUE

The purpose of this section is to derive a mathematical expression analogous to the radar range equation for a ladar system. In addition, we will derive an expression for the radiation scattered by a cloud in the direction of the ladar receiver. Finally, we will evaluate the effectiveness of the discrimination technique in terms of the signal-to-noise (target return-to-cloud return) ratio. We chose the signal-to-noise ratios as our criterion because it is the basic system parameter which determines the minimum detectable signal necessary to achieve a specified probability of detection without exceeding a specified probability of false alarm. Strictly speaking, the return from a cloud represents a range ambiguity rather than a noise factor limiting receiver sensitivity; however, if we define "noise" as unwanted electromagnetic

energy which interferes with the ability of the receiver to detect and recognize the target return, then we can consider the return from a cloud as noise.

We know that the energy of electromagnetic radiation (i.e., radiant energy) emitted or reflected per unit time by an object is commonly referred to as radiant flux or radiant power. The physical quantity radiant flux is considered as a fundamental concept from which other physical concepts called "radiometric quantities" have been derived. An analogous set of concepts referred to as "photometric quantities" has been derived for the visible part of the spectrum. This system is psychophysical in nature being based on the effect of light on the eye. Since the radiometric quantities refer to radiation in general, we will use this system in our development. An excellent treatise on both radiometric and photometric concepts is presented by Middleton [Ref. 41]. The definitions of the radiometric quantities we will use are given in Table 2. Note that the irradiance, E , has the dimensions of power density and for a point source alternate expressions can be derived that are valid in the far field.

$$E = \frac{dF}{ds} \quad (259)$$

$$= \frac{Id\omega}{ds} \quad (260)$$

$$= \frac{I \frac{ds}{x^2}}{ds} \quad (261)$$

$$= \frac{I}{x^2} \quad (262)$$

TABLE 2

Definition of Radiometric Quantities

Quantity	Definitions	Defining Symbol	Defining Equation	M.K.S. Units
1. Radiant Flux (Radiant Power)	The radiant energy per unit time emitted or reflected	P		Watts
2. Radiant Intensity	The radiant energy per unit time emitted or reflected per unit solid angle	I	$I = \frac{dP}{d\omega}$	watts steradian ⁻¹
3. Irradiance	The radiant energy per unit time incident on or passing through a real or projected surface per unit area	E	$E = \frac{dP}{ds}$	watts meter ⁻²
4. Radiance	The radiant energy per unit time emitted or reflected per unit solid angle, per unit area normal to the direction of observation	B	$B = \frac{d^2P}{d\omega ds \cos\psi}$	watts meter ⁻² steradian ⁻¹

4.2.1 DERIVATION OF THE LADAR RANGE EQUATION

If the linear dimensions of the source are small compared to the distance between the transmitter and the target, the energy may be assumed to be radiating from a point source. Furthermore, assuming that the target is far enough away so that the transmitted rays can be considered parallel to the line of incidence between the transmitter and the target, the radiant intensity, I , at the target is

$$I = I_0 e^{-\sigma r} \quad (263)$$

Let ds in Fig. 4 represent an infinitesimal area of the target surface whose normal makes an angle γ with the line segment r to the transmitter and an angle δ with the line segment $\ell = \sqrt{r^2 + d^2}$ to the receiver. The solid angle, $d\omega$, subtended by ds at the source is

$$d\omega = \frac{ds \cos \gamma}{r^2} \quad (264)$$

From Table 2, the radiant intensity of the source can be written as

$$I = \frac{dP}{d\omega} \quad (265)$$

Therefore, the radiant flux incident on the area ds is

$$dP = I d\omega = \frac{I \cos \gamma ds}{r^2} \quad (266)$$

and on substituting Equation (263) into Equation (266) we obtain

$$dP = \frac{I_0 e^{-\sigma r} \cos \gamma ds}{r^2} \quad (267)$$

The target surface has a reflective efficiency represented by its reflection coefficient ρ . The radiant flux, dP_t , reflected from the surface element ds is

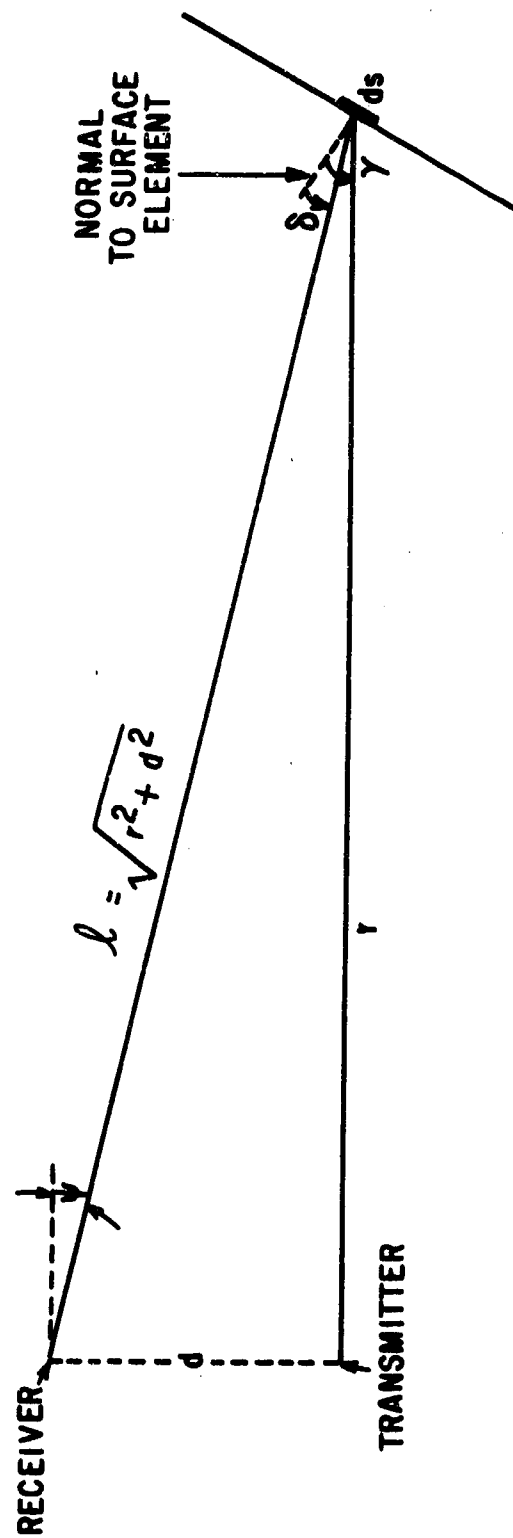


Figure 4. Geometry for Derivation of Ladar Range Equation

$$dP_t = \rho dP = \frac{\rho I_o e^{-\sigma r} \cos \gamma ds}{r^2} \quad (268)$$

Assuming the target surface to be a diffuse scatterer, Lambert's cosine law states that the total radiant flux reflected from a surface element into a hemisphere is

$$dP_t \approx \pi B ds \quad (269)$$

Thus,

$$B \approx \frac{\rho I_o e^{-\sigma r} \cos \gamma}{\pi r^2} \quad (270)$$

In addition, according to Lambert's law the radiant intensity, dI_t , reflected by the surface element ds in the direction of the receiver is defined as

$$dI_t = B \cos \delta ds \quad (271)$$

and on combining Equations (270) and (271) we obtain

$$dI_t = \frac{\rho I_o e^{-\sigma r} \cos \gamma \cos \delta}{\pi r^2} ds \quad (272)$$

Assuming the infinitesimal surface area ds approximates a point source, the irradiance, dE_R , of ds incident on the receiving aperture is, according to Equation (262),

$$dE_R = \frac{dI_R}{\ell^2} \quad (273)$$

where the radiant intensity, dI_R , at the receiver is given by

$$dI_R = dI_t e^{-\sigma \ell} \quad (274)$$

Thus,

$$dE_R = \frac{\rho I_o d^{-\sigma(r+l)} \cos \gamma \cos \delta}{\pi r^2 l^2} ds \quad (275)$$

and the receiver power (radiant flux) based on the infinitesimal target surface area is

$$dP_R = A_R dE_R \quad (276)$$

$$= \frac{\rho I_o A_R e^{-\sigma(r+l)} \cos \gamma \cos \delta}{\pi r^2 l^2} ds \quad (277)$$

or

$$dP_R = \frac{\rho I_o A_R e^{-\sigma(r+\sqrt{r^2+d^2})} \cos \gamma \cos \delta}{\pi r^2 (r^2+d^2)} ds \quad (278)$$

where A_R is the area of the receiving aperture.

Equation (278) is but one form of the general expression for the ladar range equation and if the separation, d , between the transmitter and receiver is very small compared to the distance to the target, Equation (278) reduces to

$$dP_R = \frac{\rho I_o e^{-2\sigma r} \cos^2 \gamma A_R}{\pi r^4} ds \quad (279)$$

or

$$P_R = \frac{\rho I_o e^{-2\sigma r} \cos^2 \gamma A_R}{\pi r^4} \int_s ds \quad (280)$$

Since, in general, the output power, P_T , and the beamwidth, θ_T , of a laser source is known, the radiant intensity, I_o , is

$$I_o = \frac{4P_T}{\pi \theta_T^2} \quad (281)$$

and with this substitution Equation (279) becomes

$$dP_R = \frac{4\rho P_T e^{-2\sigma r} \cos^2 \gamma A_R}{\pi^2 \theta_T^2 r^4} ds \quad (282)$$

When the target can be represented by a flat plane whose area A_t is smaller than the laser beam

$$P_R = \frac{4\rho P_T A_R A_t e^{-2\sigma r} \cos^2 \gamma}{\pi^2 \theta_T^2 r^4} \quad (283)$$

If the target can be regarded as a flat plane larger than the laser beam, and the variation of r over the illuminated region can be justifiably ignored,

$$A_t = \frac{\pi \theta_T^2 r^2}{4 \cos \gamma} \quad (284)$$

and

$$P_R \approx \frac{\rho P_T A_R e^{-2\sigma r} \cos \gamma}{\pi r^2} \quad (285)$$

Thus, we see that the fourth power range relationship of radar systems is also valid for ladar systems. Furthermore, in cases where the target is larger than the transmitter beam, the target return varies as the range squared.

4.2.2 DERIVATION OF THE CLOUD RETURN EQUATION

In deriving an expression for the radiant flux at the receiver (which is now assumed to be located at the transmitter) due to scattering from the cloud, we consider an infinitesimal element of volume of the cloud (Fig. 5) where

$$dv = dA dx \quad (286)$$

$$= d\omega x^2 dx \quad (287)$$

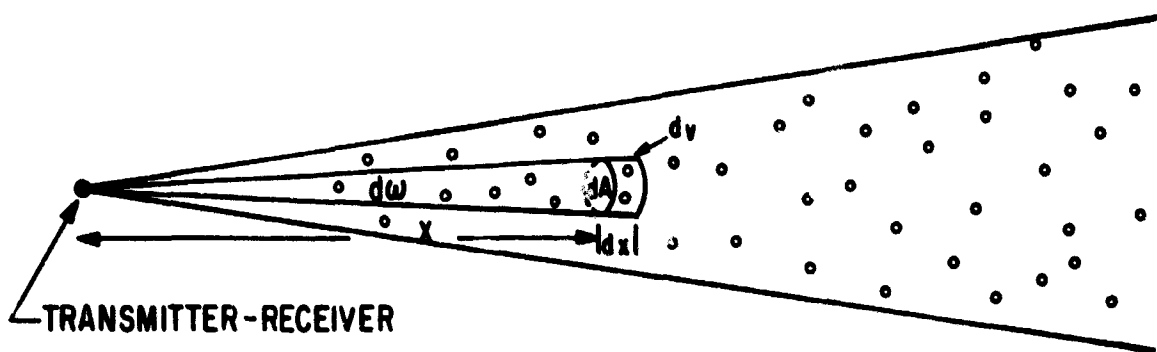


Figure 5. Geometry for Derivation of Cloud Return

The irradiance, E , of the source incident on this infinitesimal volume of cloud particles is

$$E = \frac{I_0 e^{-\sigma x}}{x^2} \quad (288)$$

If we can assume the radiation scattered from the element of volume, dv , as coming from a point source of which the intensity is proportional to the number of particles, then the radiant intensity, I_c , for any scattering angle, θ , is given by

$$dI_c = \beta(\theta) E dv \quad (289)$$

In the direction of the receiver, i.e., for $\theta = \pi$, the radiant intensity is

$$dI_c = \beta(\pi) E dv \quad (290)$$

$$= \frac{\beta(\pi) I_0 e^{-\sigma x}}{x^2} dv \quad (291)$$

Accordingly, then, the irradiance, dE_R , at the receiver is

$$dE_R = \frac{dI_R}{x^2} \quad (292)$$

where

$$dI_R = dI_c e^{-\sigma x} \quad (293)$$

Thus,

$$dE_R = \frac{\beta(\pi) I_0 e^{-2\sigma x}}{x^4} dv \quad (294)$$

and the total power received from the element of volume is

$$dP_R = A_R dE_R \quad (295)$$

$$= \frac{\beta(\pi) A_R I_0 e^{-2\sigma x}}{x^4} dv \quad (296)$$

On substituting Equation (287) into Equation (296) we obtain

$$dP_R' = \beta(\pi) A_R I_o d\omega \frac{e^{-2\sigma x}}{x^2} dx \quad (297)$$

$$= \beta(\pi) A_R I_o 2\pi(1 - \cos \frac{\theta_R}{2}) \frac{e^{-2\sigma x}}{x^2} dx \quad (298)$$

where $\frac{\theta_R}{2}$ is the half-angle of the receiver's field of view. Therefore, the radiant flux (power) at the receiver is

$$P_R' = \beta(\pi) A_R I_o 2\pi(1 - \cos \frac{\theta_R}{2}) \int_{r_o}^r \frac{e^{-2\sigma x}}{x^2} dx \quad (299)$$

The complicated integration process suggested by Equation (299) is beyond the scope of this paper. An excellent coverage of integrals of this type (usually called exponential integrals depending on the limits of integration) is given in Appendix I of Kourganoff's book [Ref. 34]. The omission of the solution will not affect the results of our derivation. For convenience, then, we let

$$E_2(2\sigma) = \int_{r_o}^r \frac{e^{-2\sigma x}}{x^2} dx \quad (300)$$

Thus, Equation (299) becomes

$$P_R' = \beta(\pi) A_R I_o 2\pi(1 - \cos \frac{\theta_R}{2}) E_2(2\sigma) \quad (301)$$

4.2.3 SIGNAL-TO-NOISE ANALYSIS

In the derivation of Equations (280) and (301) nothing was said about the state of polarization of the transmitted, reflected or scattered waves. We simply assumed the output radiation of the laser to be

unpolarized where ρ is the reflection coefficient for unpolarized radiation and $\beta(\pi)$ is the volume backscatter coefficient for unpolarized radiation. We begin our evaluation of the polarization discrimination technique by repeating Equations (280) and (301):

$$P_R = \frac{\rho A_R I_o e^{-2\sigma r} \cos^2 \gamma}{\pi r^4} \int_s ds \quad (280)$$

$$P'_R = \beta(\pi) A_R I_o 2\pi (1 - \cos \frac{\theta_R}{2}) E_2(2\sigma) \quad (301)$$

If we now insert a linear polarizer at the transmitter and an analyzer at the receiver we obtain

$$P_{R\perp} = \frac{\eta^2}{2} \frac{\rho_{\perp} A_R I_o e^{-2\sigma r} \cos^2 \gamma}{\pi r^4} \int_s ds \quad (302)$$

$$P'_{R\parallel} = \frac{\eta^2}{2} \beta_{\parallel}(\pi) A_R I_o 2\pi (1 - \cos \frac{\theta_R}{2}) E_2(2\sigma) \quad (303)$$

where the subscript "1" refers to the fraction of the plane-polarized transmitted wave which is reflected with its polarization vector orthogonal to that of the transmitted radiation. Similarly, the subscript "II" refers to radiation with its polarization vector parallel to that of the transmitted wave; η is the transmission efficiency of the polarizers (assumed to be the same for both). The 1/2 represents the reduction in transmitter output due to the polarization process.

We now define the signal-to-noise ratio for the situation where the output of the transmitter is unpolarized as the ratio of Equation (280) to (301), i.e.,

$$SNR_+ = \frac{P_R}{P'_R} \quad (304)$$

where the subscript "+" denotes that the transmitted radiation is unpolarized. Similarly, the signal-to-noise ratio for the system whose transmitter output is plane polarized is

$$\text{SNR} = \frac{P_{R1}}{P_{R11}} \quad (305)$$

Now, by making the obvious substitutions, it can be easily shown that

$$\text{SNR} = \left[\frac{\beta(\pi)}{\beta_{11}(\pi)} \right] \left(\frac{\rho_1}{\rho} \right) \text{SNR}_+ \quad (306)$$

Upon careful scrutiny of Equation (306) we observe that while the value of the term in parenthesis can never be greater than unity (and is usually much less), the value of the term within the brackets can be very large if it should turn out that $\beta_{11}(\pi)$ can be reduced to a very small value by the use of a perfect analyzer at the receiver. We see, then, that the signal-to-noise ratio for the "cross-polarized" system will be much greater than that of the unpolarized system where the degree of improvement is given by the polarization discrimination coefficient, defined as

$$\text{PDC} = \left[\frac{\beta(\pi)}{\beta_{11}(\pi)} \right] \quad (307)$$

We have neglected the effects of other noise sources in our development because they, in general, limit the ability of the receiver to detect the wanted signal rather than its ability to discriminate between wanted and unwanted signals. However, for situations where the effects of other noise sources are not negligible, the appropriate expressions should be modified accordingly.

This completes the quantitative analysis of our cloud/target polarization discrimination technique.

SECTION V

THE LABORATORY SIMULATION OF THE FORMATION OF ATMOSPHERIC AEROSOLS

5.1 INTRODUCTION

The practical application of the cloud/target discrimination technique developed in the preceding section is dependent on the experimental verification of the technique both in the laboratory and in the field. A high degree of confidence in any conclusion based on the resultant data from such an effort can be realized only if quantitative descriptions can be obtained of both the target and the cloud. In order to satisfy these "conditions for confidence" in the laboratory it is necessary to create an artificial cloud that best represents the atmospheric variety. Even though a laboratory cloud generation system cannot reproduce all of the natural processes involved in the actual formation and evolution of an atmospheric cloud, an adequate laboratory model can be created by a system possessing the following characteristics:

- a. Individual control of the following parameters:
 - (1) Temperature
 - (2) Humidity
 - (3) Volume
 - (4) Pressure
 - (5) Dispersion of Condensation Nuclei
- b. Environmental conditions well controlled, instrumented, and repeatable.
- c. Minimum interference from walls of container.

It is our purpose, then, in this section to describe the design, fabrication, and instrumentation of a laboratory cloud chamber and the

corresponding characteristics of the simulated cloud used for the cloud/target polarization discrimination experiments.

5.2 THE CLOUD CHAMBER

The cloud is generated in a chamber constructed of modular sections which can be coupled together to form a convenient length. Each module was fabricated from 1/4-inch-thick sheet aluminum in the form of a cube with two opposite sides open. The internal dimensions of each module are 1 meter x 1 meter x 1 meter. Aluminum edge strips were welded to the outside of the open ends to provide rigidity and to serve as gasket surfaces to obtain an airtight and watertight seal when coupling one module to another or for attaching a door. Two 1-meter x 1-meter doors were fabricated from 1/4-inch-thick sheet aluminum. Viewing ports 10 centimeters in diameter were installed in the center of each door. Additional viewing ports were installed in the center of one side of the modules (see Fig. 6). The inside of each module is painted with nonreflecting flat black (camouflage) paint and the outside (top, bottom, and sides) is insulated with two layers of 2-inch-thick beadboard. The doors are similarly insulated. The modules are supported on a specially built 1-inch-thick plywood-top table and can be coupled together (with the doors attached to the end modules) to form a variable-length cloud chamber.

Each module is provided with an independent water vapor injection system at the bottom and independent cooling coils at the top. The water vapor in the form of steam is generated outside the chamber in a steam boiler (Model MB-6L, Automatic Steam Products Corp., N.Y., N.Y.). The steam is injected into each module via a 3/8-inch O.D. copper tube

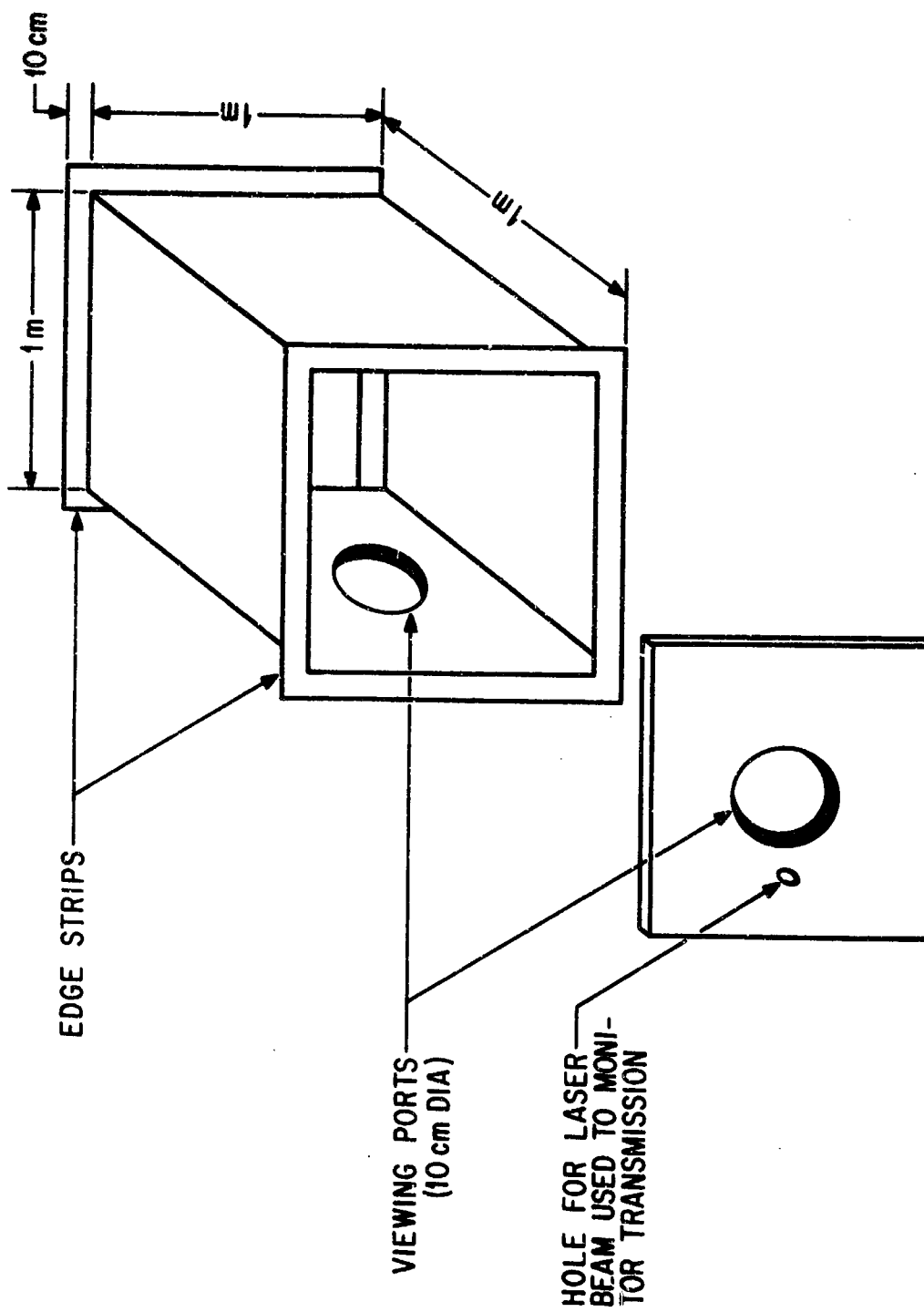


Figure 6. Overall Dimensions of Cloud Chamber Module

through an electric solenoid valve (Type GL-181, Series 500, Atkomatic Valve Co., Inc., Indianapolis, Indiana) into a needle valve control. The needle valve control is mounted along the center line and 2 inches above the chamber floor in the wall opposite the side containing the viewing port. An independent set of serpentine cooling coils made from 1/2 inch I.D. copper tubing is mounted inside of each module. The coils are attached directly to the top section which thus acts as a giant cooling fin. To avoid heating the laboratory air and to maintain minimum noise and vibration levels, the compressors, 1-1/2 horsepower heavy duty air-conditioning units (Model AH-16H, Dunham-Bush Inc., West Hartford, Connecticut), are mounted outside the laboratory. The refrigerant (Freon-12) is pumped to each module through 3/8-inch O.D. copper tubing, and through a thermostatic expansion valve (Type CFE-1-1/2 C, Sporlan Valve Co., St. Louis, Missouri) mounted at the top of the outside wall opposite the side with the viewing port. Combination filter-drier units (Catch-All Series, Sporlan Valve Co., St. Louis, Missouri) are installed in the liquid line ahead of the expansion valve and in the suction line to remove moisture and foreign material from the system. The thermostats are set to maintain the temperature in the modules between -8°C and -5°C.

The original design concept for the cloud chamber provided for the injection of liquid nitrogen and compressed air at varying rates confluent with the steam to (a) offset the steam heatload and (b) provide some measure of variability in particle size distributions that can be produced. Additionally, the compressed air injection system was to deliver (relatively) dry air over the cooling coils to prevent ice from forming

on the coils. We observed, however, during the initial operation of the chamber, that the compressors handled the steam heatload adequately and variable particle size distributions could be generated by varying the steam injection rates and the steady state temperature of the chamber. We observed, also, that blowing compressed air over the cooling coils produced undesirable turbulence within the cloud. We, therefore, omitted the liquid nitrogen and compressed air injection systems in the final design.

Remote sensing thermometers are used to monitor the room temperature and the coil and air temperature of each modular section. A probe type absorption hygrometer based on electrical changes produced by the absorption of water on conducting materials (Model W611A, Minneapolis Honeywell, Minneapolis, Minnesota) is used to monitor the relative humidity within the chamber while a membrane type absorption hygrometer (Bacharach Industrial Instruments Co., Pittsburgh, Pennsylvania) is used to monitor the relative humidity within the laboratory.

Provision has been made in the design for the insertion of transparent baffle plates between sections for the creation of different conditions in selected portions of the chamber to more realistically simulate actual clouds. It would then be possible to have the cloud localized near the detector, near the target, or at some intermediate point.

A cut-away view of a modular section is shown in Fig. 7.

5.3 CLOUD GENERATION TECHNIQUES

As we discussed in Section II, an atmospheric cloud is the result of either lowering the temperature of a volume of air to a point where its capacity for water vapor is greatly reduced or of adding water vapor to the

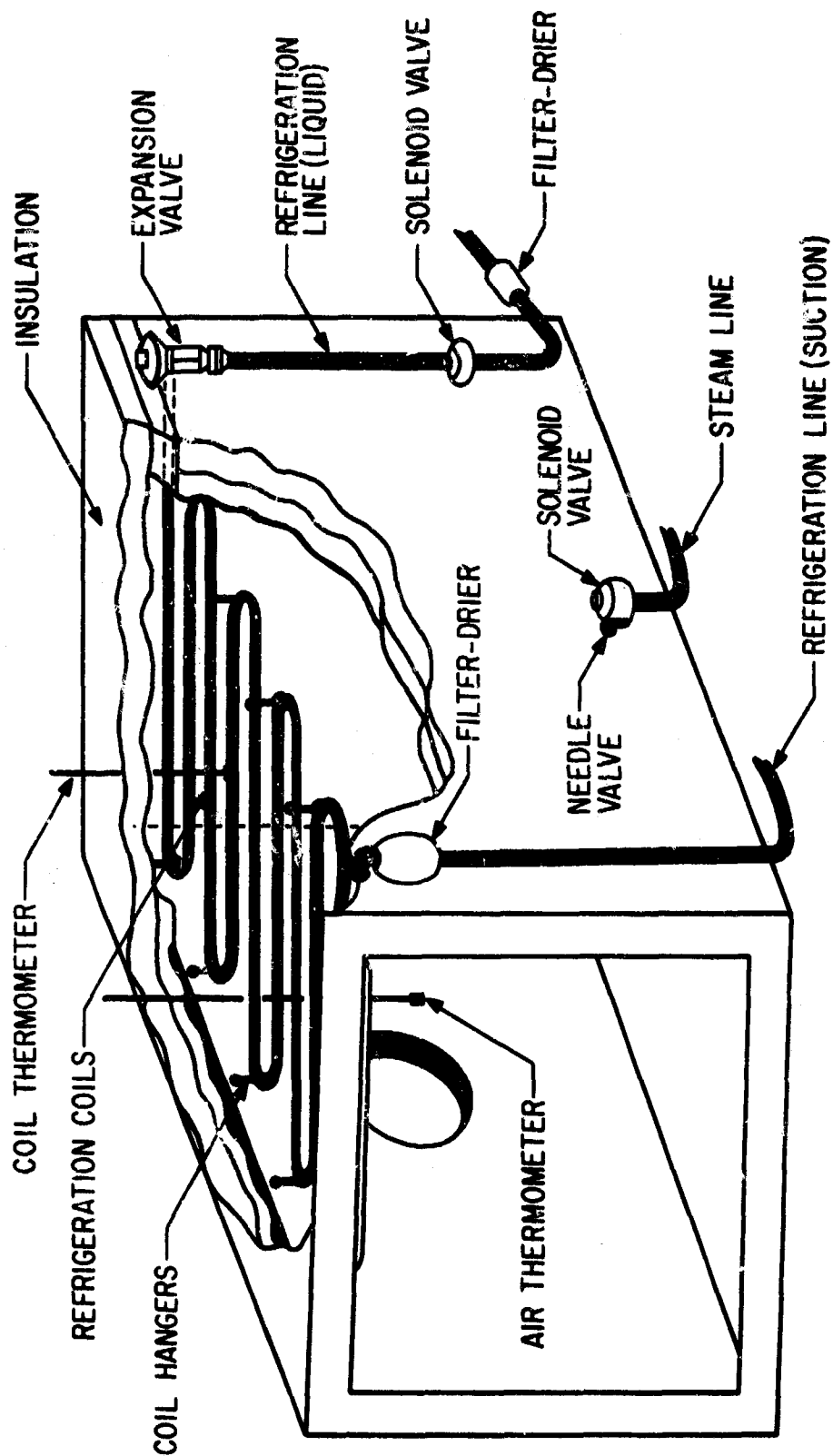


Figure 7. Cut-Away View of Cloud Chamber Module

air to the extent necessary to increase the content to the maximum capacity possible at the prevailing temperature. A combination of these processes may also result in the formation of a cloud.

Two basically different techniques are used to produce artificial clouds in the laboratory: the mechanical technique and the thermodynamic technique. In the mechanical process, water under pressure is forced through a tiny orifice and mixed with high pressure air. The mixture is then expanded to form a fine spray. In the thermodynamic process, one of the parameters (pressure or temperature) of the cloud generation system is varied, resulting in the condensation of water vapor contained in the saturated atmosphere within the system. Controlled cloud production utilizes variations or combinations of these two methods. We chose to use a combination of the two techniques in our chamber facility.

We begin the cloud generation process by sealing off the chamber from the laboratory environment (primarily accomplished by covering viewing ports with quartz plates) and then lowering the temperature of the air within the chamber from approximately 25°C (room temperature) to -8°C thereby increasing the relative humidity within the chamber from about 23 per cent to 60 per cent. During this phase, the pressure within the chamber is assumed constant and equal to the atmospheric pressure. We now inject steam under pressure through the individual orifices in each section. The transmissivity of the cloud is continuously monitored and recorded on a strip chart recorder (Hewlett-Packard Model 680) using a 100 mw He-Ne (helium-neon) gas laser (Model 125, Spectra-Physics, Palo Alto, California) modulated with a KDP (potassium dihydrogen phosphate) crystal at a pulse repetition frequency of 1 kHz

that is beamed into a photomultiplier tube over a one-way path through the length of the cloud chamber. Steady state conditions appear to occur when the chamber temperature is between -5°C and 0°C and the relative humidity in the chamber reaches 90 percent. During this steady state phase we have been able to hold the transmissivity to 20 percent for two hours with only five to ten percent fluctuations. The corresponding droplet diameters as monitored with microscopic photography techniques indicate particle size distributions which peak (mode diameter) at 5 to 6 microns with mean droplet diameters ranging from 8.9 to 9.1 microns in good agreement with the distributions of Table 1 for stratus type clouds (includes fog which is defined as a stratus cloud that touches the ground). For the temperature range between 0 and $+5^{\circ}\text{C}$ the droplet size distribution indicates that the cloud resembles a warm temperature coastal fog (mode diameter: 8 - 10 microns, mean diameter: 12 - 15 microns). The transmissivity of the cloud is greater (40 - 60 percent) for this phase indicating a less dense cloud which is another characteristic of a coastal fog. Additionally, the transmissivity fluctuates considerably over long periods of time and is impossible to hold constant for longer periods than 15 minutes.

The original design concept for the chamber provided for the injection of condensation nuclei to facilitate cloud formation. However, we have had phenomenal results using the nuclei present in the natural air in the chamber and carried by the steam. The existence of nuclei is indicated by the fact that the relative humidity within the chamber never increases above 92 percent. If the process of producing a cloud, and then allowing it to dissipate, is repeated several times,

the resulting clouds become successively less dense, requiring increasingly longer time intervals in which to form.

5.4 CLOUD SAMPLING TECHNIQUES

It is surprising, indeed, that while much effort has been devoted to developing experimental techniques for measuring the size and concentration distributions of cloud droplets, we still do not have an entirely satisfactory technique for accurately and reliably measuring the size distribution without physically disturbing the cloud and that does not require extremely tedious drop-by-drop measurements. The following are the most commonly used methods used for measuring droplet sizes within a cloud or fog:

a. An optical technique based on the diffraction theory of Airy [Ref. 1] which depends on the measurement of the distribution of light intensity (coronas) produced by the diffraction of a beam of light. Wilson [Ref. 59] has argued mathematically that this method of sampling favors the larger diameter droplets (>20 microns) and is useful only in homogeneous fogs.

b. Kneusel [Ref. 30] built an apparatus to observe the rate of fall of atmospheric fog particles in undisturbed air. Assuming this velocity of fall was due to the earth's gravitational force of attraction, he calculated the corresponding droplet sizes. His distributions, however, appear to favor the smaller droplets.

c. An electrostatic precipitation method first devised by Panthenier and Brun [Ref. 46] uses a metal cylinder lined with a special absorbent paper dyed with methylene blue. The droplets within the cylinder are precipitated onto the paper by an electrostatic field and

produce impressions, the diameters of which are proportional to the actual particle diameters.

d. Köhler [Ref. 31] attempted to collect fog droplets on fine wire but was unable to correct for the effects of evaporation. On the other hand, Dessens [Ref. 14] and later Arnulf and Bricard [Ref. 3] obtained results (see Table 1) using spiders' webs.

e. Probably the most reliable technique employed by the majority of researchers involves the collection of the droplets on suitably prepared surfaces and the subsequent photographing of the droplets or their impressions under a darkfield microscope. In one method employed by many researchers, a microscope slide is coated with a greasy substance (usually petroleum jelly) while in an equally popular method, the slide is covered with oil (mineral oil, kerosene, etc.). According to Houghton [Ref. 22] droplets caught on slides coated with petroleum jelly flatten out to the point where the droplet radius measured from the slide is almost twice as large as that of the original droplet; those caught on slides covered with oil, however, sink and remain essentially spherical [Ref. 8]. An alternate method is to coat a slide with magnesium oxide in which the droplets produce impressions, the diameters of which are proportional to the actual particle diameters.

f. Laser holographic techniques have been developed that provide a three-dimensional view of fog droplets in a specific volume of space. However, the use of this technique is limited in application, due to stringent stability and alignment requirements.

g. Aerosol counters are commercially available that determine the size distribution and concentration of aerosol particles by measuring

the intensity of the light scattered by a single particle which is illuminated by a visible light source.

After careful consideration of these methods with regard to the availability of resources (money, personnel, equipment, materials, laboratory space, etc.) and the reliability and accuracy of the resulting data, we chose to measure and compare the size distribution by two separate methods: microscopic-slide photography and a light-scattering aerosol counter. The aerosol counter has the additional capability of providing concentration data.

5.4.1 MICROSCOPIC SAMPLING TECHNIQUE

The microscopic sampling technique consists of thoroughly cleaning suitable microscope slides and then applying melted petroleum jelly to the slide surface to form a very thin film. A drop of mineral oil or kerosene is next applied to the jelly surface. The slide is cooled to the ambient temperature of the chamber and then submerged in the cloud for a finite time. The droplets sink through the kerosene and barely rest on the petroleum jelly, the buoyancy of the kerosene preventing them from flattening out on or penetrating into the jelly. The validity of this technique is indicated (when viewing a sample under the microscope) by the fact that while the droplets do not appear to evaporate they do wander and collide to some extent. The corresponding degree of coalescence is, however, very small with never a complete merging of droplets; that is, occasionally a smaller droplet will appear to be "stuck" to a larger droplet. The slide is removed from the chamber and photographed under a darkfield microscope (Bausch and Lomb Dynazoom Flat Field Binocular Body Microscope, Bausch and Lomb, Rochester, New York). We

have observed, using the petroleum jelly kerosene mixture, that the captured droplets do not begin to evaporate or coalesce for about 30 minutes at room temperature. If maintained at the ambient temperature of the chamber, their size and concentration distributions remain essentially unchanged. The photomicrograph is then magnified under a measuring microscope (Carl Zeiss Tool Makers Microscope) and the diameter of each particle is measured with an accuracy of 1 micron in 125 millimeters. The measured values of the droplet diameters are then sorted into size groups and recorded in increments of 0.1 micron.

In determining the size distribution and the corresponding degree of repeatability of our artificial cloud, we compared the data collected by two different sampling techniques:

a. In the first method we prepare seven slides with the petroleum jelly kerosene mixture in the manner described in the preceding paragraph and then place them in a narrow covered tray extending across the cross sectional width of the chamber. The slides are allowed to cool to the ambient temperature of the chamber before being exposed to the cloud. When steady state conditions exist within the cloud for a particular transmissivity, the tray is uncovered and the slides are exposed to the cloud for a finite time. At the end of this sampling time the first slide is removed from the chamber and immediately photographed under the microscope. The remaining slides are left in the chamber with their surfaces exposed to the cloud and are subsequently removed and photographed in turn.

This sampling method was used to collect data for clouds of different densities for the temperature ranges -5° to 0°C and 0° to $+5^{\circ}\text{C}$.

The density of the individual clouds was continuously monitored as a function of the transmissivity. While the individual size distributions did not appear to vary as a function of density (as indicated by the transmissivity) within either of the temperature intervals, there was a definite difference in size distributions and corresponding densities of the clouds obtained for the two temperature intervals. For the temperature interval -5° to 0°C , the mode diameter, d_d , was 5 microns and the corresponding mean diameter, d_m , was 8.9 microns, while for the temperature interval 0° to $+5^{\circ}\text{C}$, d_d was 8 microns and d_m was 12.3 microns. In the lower temperature interval the transmissivity ranged from 20 to 100 percent while in the higher temperature interval the transmissivity ranged from 40 to 100 percent. We conclude, then, from the increase in droplet size coupled with a decrease in density (indicated by an increase in transmissivity) that the density of the clouds in the temperature interval above 0°C is less than that of the clouds in the interval below 0°C . The resultant size distributions for arbitrary density (transmissivity) as a function of temperature are shown in Figs. 8 and 9.

b. In the second sampling technique the slide surfaces are prepared and exposed to the cloud in the same manner as previously described. But at the end of the sampling interval when the first slide is removed for photographing the remaining slides are covered and thusly isolated at the ambient temperature of the chamber and are subsequently removed and photographed.

This sampling method was used to collect data as a function of cloud density and chamber temperature in the same manner as in the first method. Again, the results indicated a temperature dependence

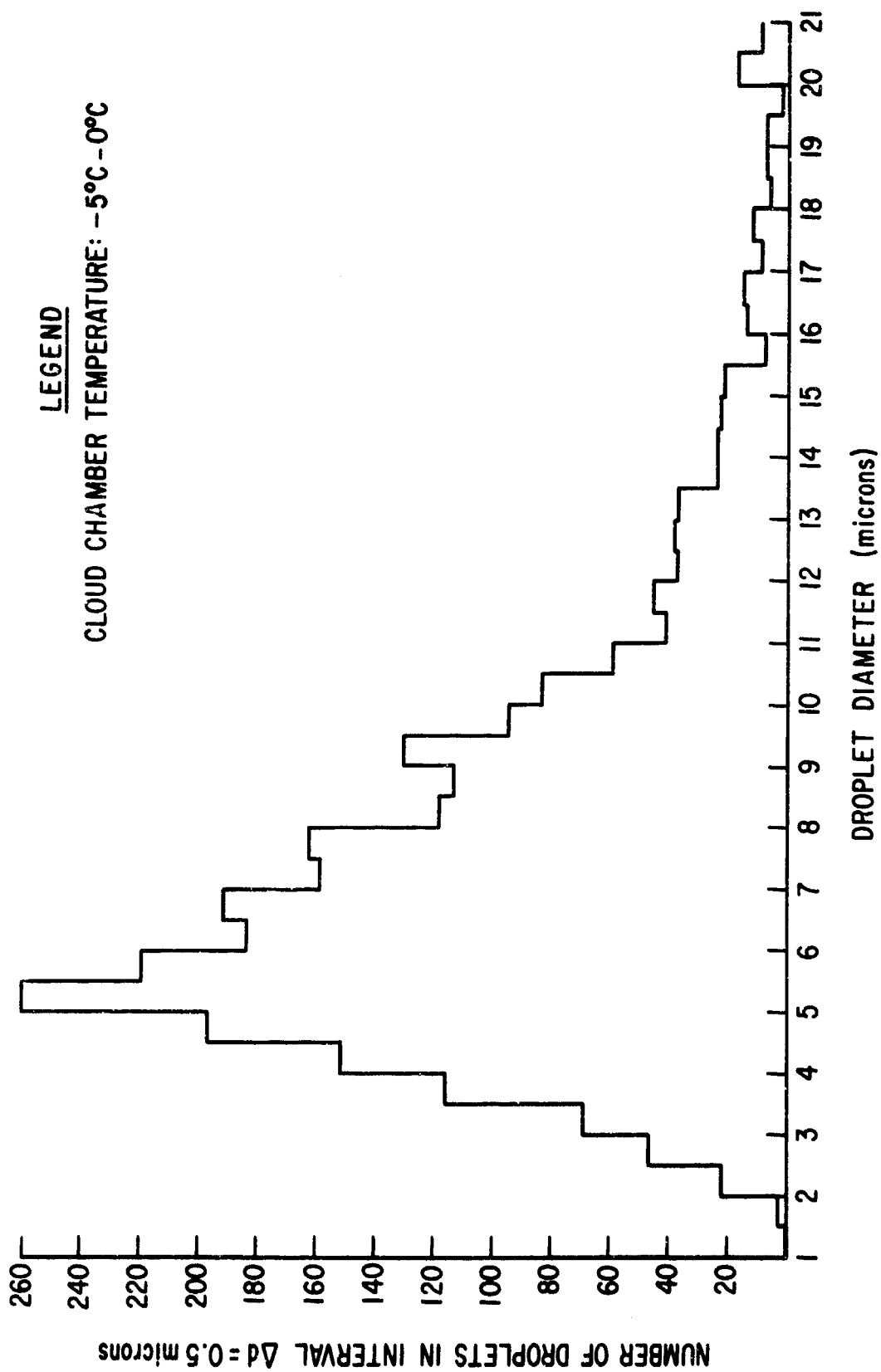


Figure 8. Histogram of Droplet Diameters for First Sampling Method (Temperature: $-5^{\circ}\text{C} - 0^{\circ}\text{C}$)

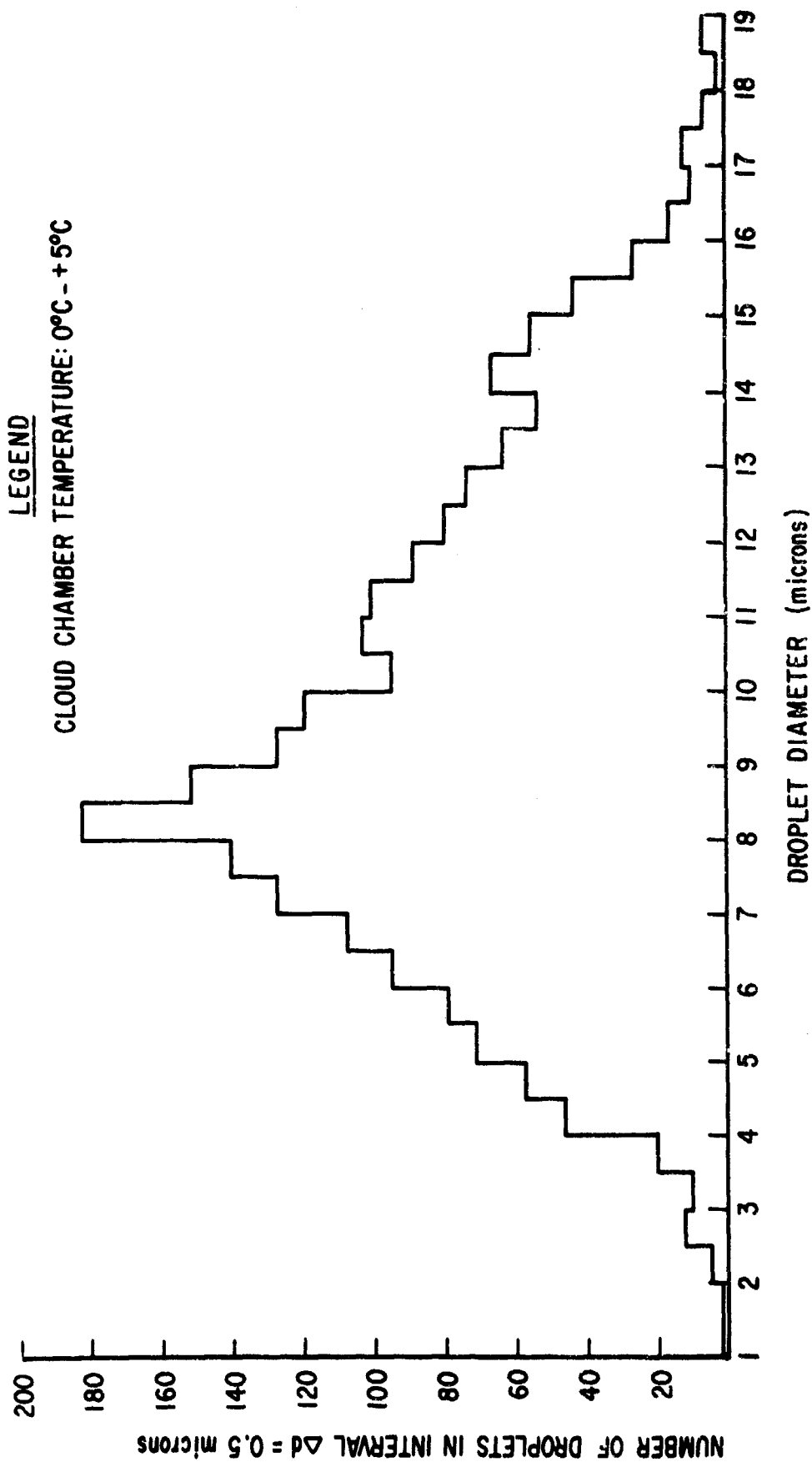


Figure 9. Histogram of Droplet Diameters for First Sampling Method (Temperature: 0°C - +5°C)

while a variation in the density (transmissivity) did not indicate a change in size distribution. The resultant size distributions are shown in Figs. 10 and 11. For the temperature interval -5° to 0°C , $d_d = 6$ microns and $d_m = 9.2$ microns; for the interval 0° to $+5^{\circ}\text{C}$, $d_d = 10$ microns and $d_m = 15$ microns.

Examples of the photomicrographs from which the temperature dependent size distributions were derived are shown in Figs. 12 and 13.

A comparison of the results obtained by the two sampling techniques show that, while the mode diameters differ by about 20 percent, the mean diameters differ by only 3.5 percent. We assume that the distributions obtained by the first method more realistically represent the actual cloud because almost twice as many particles were collected by the first method. The sampling intervals (based on the first slide) were equal for the two methods and when this interval was doubled using the second method of sampling in subsequent experiments, the resultant distributions corresponded to those obtained by the first method.

5.4.2 PARTICLE MONITOR-SAMPLING TECHNIQUE

The particle monitor-sampling technique consists of using a light-scattering aerosol counter for determining the size distribution and concentration of aerosol particles. A light-scattering aerosol counter (Model 202, Royco Instruments, Menlo Park, California) determines the size distribution and number concentration of aerosol particles by measuring the intensity of visible light scattered by a single particle in the range of scattering angles from 75° to 105° . The air (containing the aerosol particles) being monitored, is blown through a volume illuminated by the radiation of a white light source of color temperature

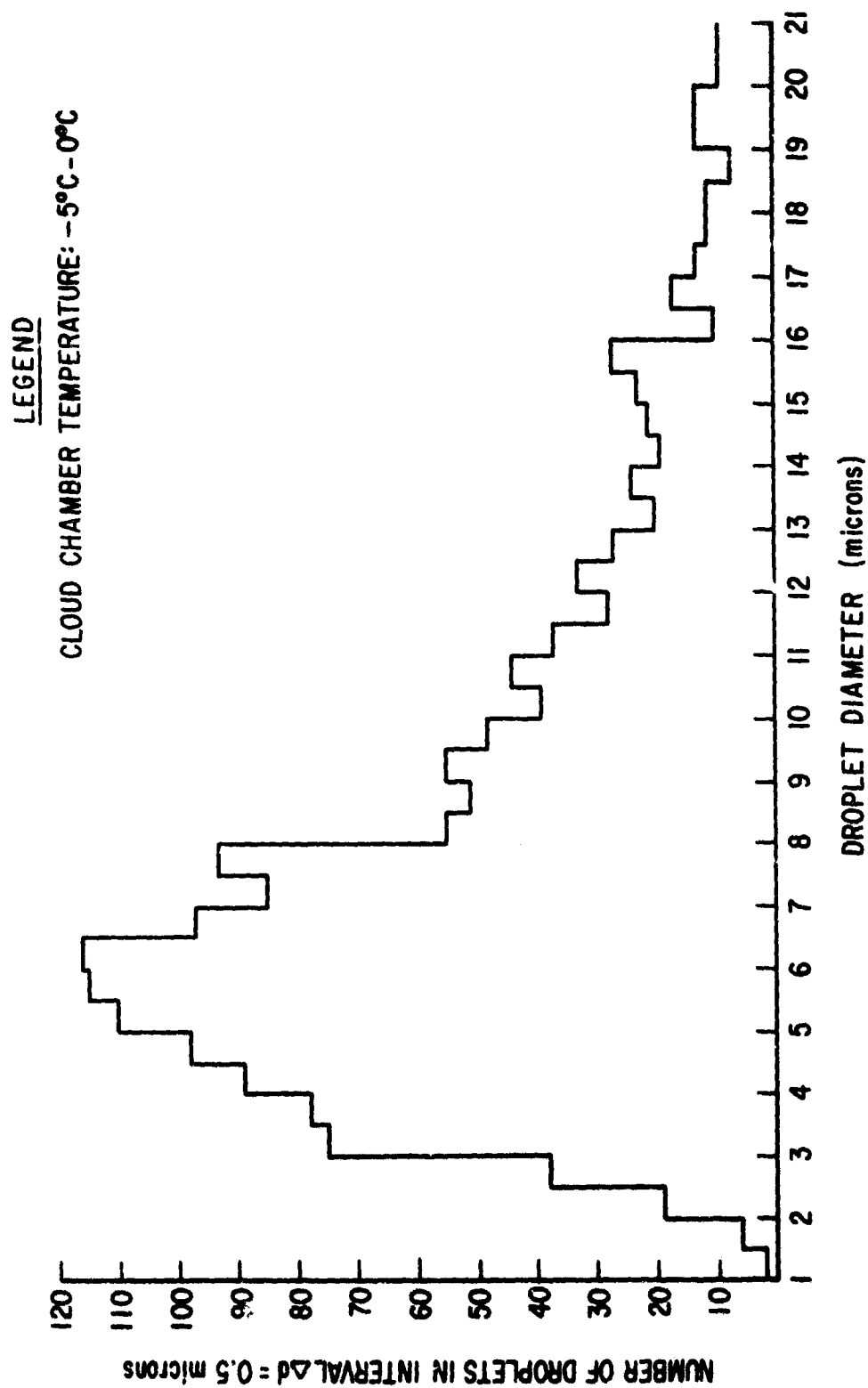


Figure 10. Histogram of Droplet Diameters for Second Sampling Method (Temperature: $-5^{\circ}\text{C} - 0^{\circ}\text{C}$)

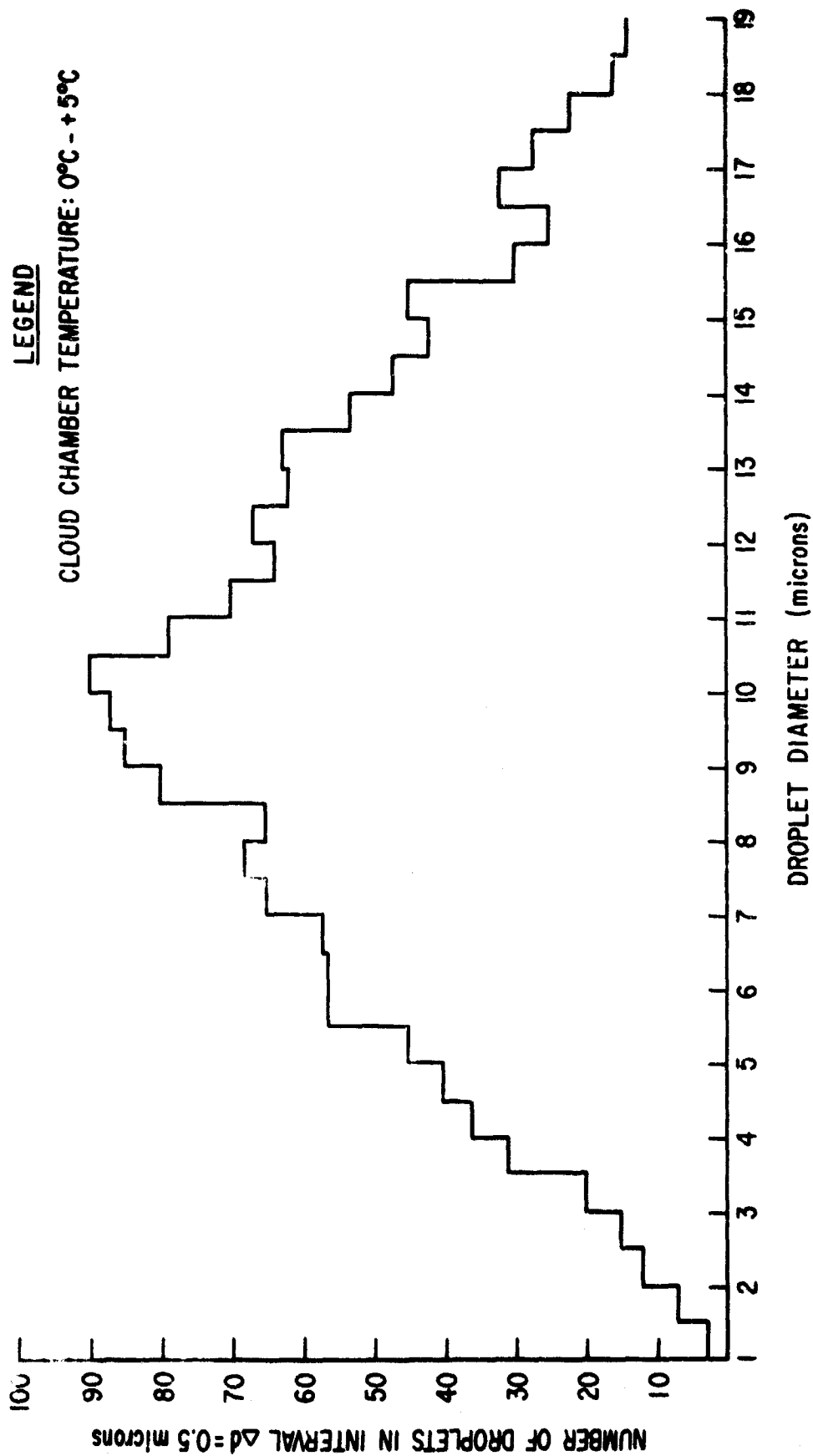


Figure 11. Histogram of Droplet Diameters for Second Sampling Method (Temperature: 0°C - +5°C)

NOT REPRODUCIBLE

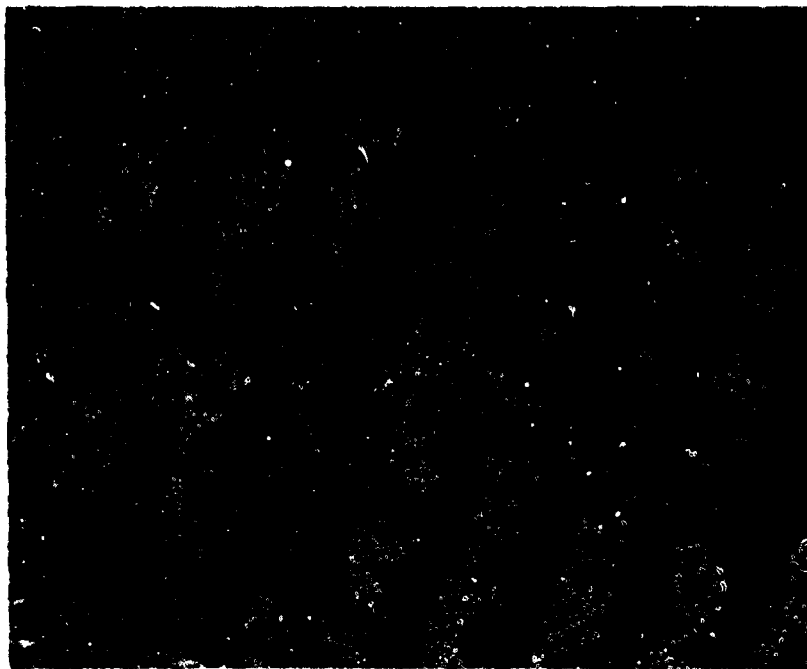


Figure 12. Photomicrograph (X400) of Laboratory
Generated Cloud Droplets

NOT REPRODUCIBLE

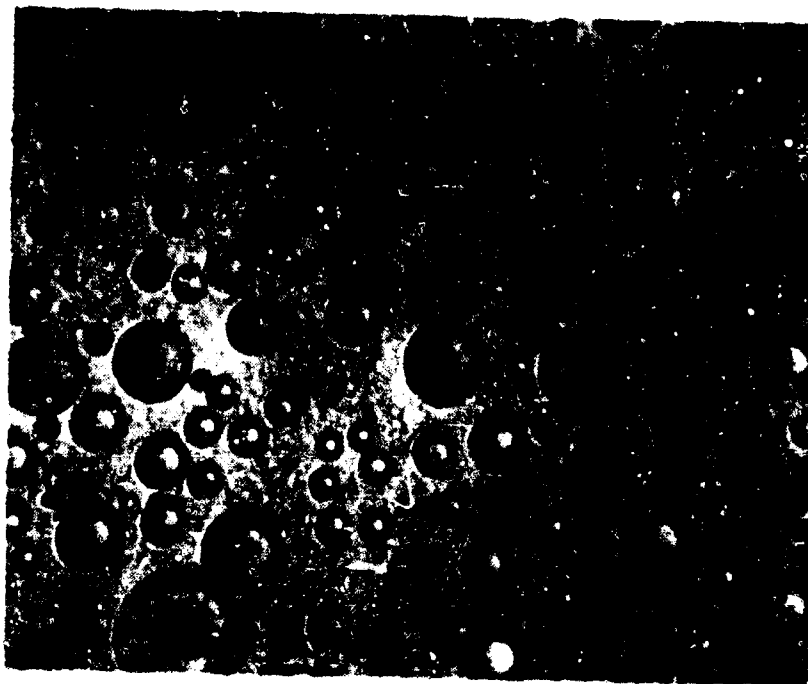


Figure 13. Photomicrograph (X400) of Laboratory
Generated Coastal Fog Droplets

2800° K. The detector is a photomultiplier tube. Each particle remains within the illuminated volume for a short time only and the magnitude of its electrical signal depends on its size. The signals are electronically classified according to their magnitude in a narrow interval. The number of the impulses in each interval is counted and printed out in definite time intervals.

The size distributions obtained from the aerosol counter differed greatly from those obtained from the microscope-slide photography technique. In fact, the particle counter scarcely indicated the presence of any particles, while at the same time approximately 10,000 droplets were collected on the slides. We believe the reason that the particle counter does not give a true representation of the size distribution is because the droplets evaporate before they can be measured due to the large temperature difference between the droplet and the interior of the counter. The validity of this argument is indicated by the fact that the counter appears to operate satisfactorily when counting "steam particles," i.e., for steam injected into the chamber when the temperature of the chamber was approximately 25°C (room temperature) before steam injection.

SECTION VI

EXPERIMENTAL VERIFICATION OF THE CLOUD/TARGET POLARIZATION DISCRIMINATION TECHNIQUE

6.1 INTRODUCTION

In this chapter we present the results of our experimental research program to determine the validity of the cloud/target polarization discrimination technique. The program is divided into a laboratory verification phase and a field evaluation phase. In the laboratory verification phase of the investigation we measured the signal returns from a reference target and various clouds generated in the cloud chamber facility described in Section V as a function of cloud transmissivity. The polarization properties of the return signals were then compared using the plane of vibration of the electric field vector of the transmitted wave as a reference. In this respect we define the following symbols assuming the transmitted wave to be linearly polarized:

"+" signifies unpolarized radiation

"||" signifies radiation whose electric field vector vibrates parallel to that of the transmitted wave

"⊥" signifies radiation whose electric field vector vibrates orthogonally to that of the transmitted wave

A qualitative verification of the polarization discrimination technique is depicted in the series of photographs shown in Figs. 15 and 17. These photographs present a visual record of the scattering phenomena we observed when the output of a linearly polarized He-Ne (helium-neon) gas laser was transmitted through a laboratory generated cloud and was incident on a diffusely reflecting target. The wavelength, λ , of the laser radiation was in the visible (red) portion of the electromagnetic

spectrum and equal to 6328 Angstroms (10^4 Angstroms = 1 micron). A 3 in. x 5 in. piece of fine grain sandpaper sprayed with white paint was used as the diffuse target. A 35mm Nikon F camera was used to photograph the radiation scattered from the cloud and the target. An analyzer was positioned in front of the camera and mounted so that it could be easily removed and replaced in its original position. Schematic diagrams of the experimental arrangements used in obtaining the photographic illustrations of Figs. 15 and 17 are shown in Figs. 14 and 16, respectively.

The experimental arrangement illustrated in Fig. 14 was used to obtain the photographs shown in Fig. 15. For this situation the laser beam was transmitted along the long dimension of the cloud chamber and impinged upon the diffuse target which was placed at the far end of the chamber. The camera was positioned coaxial to that portion of the transmitted beam being propagated through the cloud chamber. The analyzer was not used for the photograph shown in Fig. 15a. The large circle in the center of the photograph is the viewing port. The smaller red circle within the viewing port represents the sum of (a) the radiation reflected from the target at the far end of the chamber and (b) the radiation back-scattered from the cloud along the length of the chamber. The diameter of the viewing port is 10 centimeters; and while the diameter of the transmitted laser beam is only one centimeter, the diameter of the red circle is approximately six centimeters. The apparent increase in the diameter of the transmitted beam was, in reality, caused by a halo of scattered light surrounding the beam. This halo of light was primarily composed of the radiation scattered out of the transmitted beam by the cloud particles. The black annular ring surrounding the red circle represents that portion

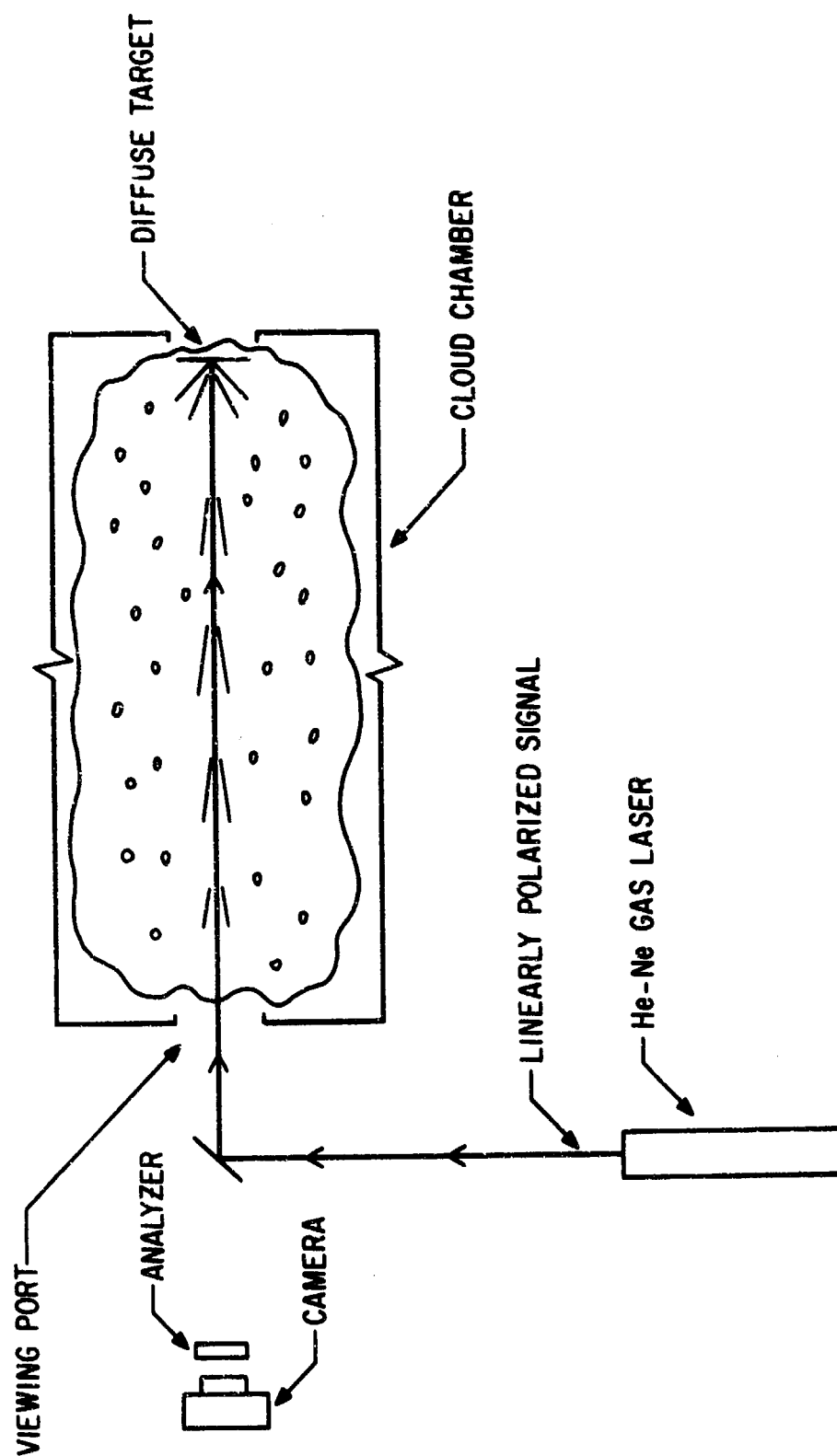


Figure 14. Experimental Arrangement for Photographs of Fig. 15



(a)



(b)

Figure 15. Photographic Illustration of the Cloud/Target Polarization Discrimination Technique. (a) Laser Output Linearly Polarized, No Analyzer on Camera; (b) Laser Output Linearly Polarized, Plane of Polarization of Analyzer (Located at Camera) Orthogonal to That of Transmitted Beam.

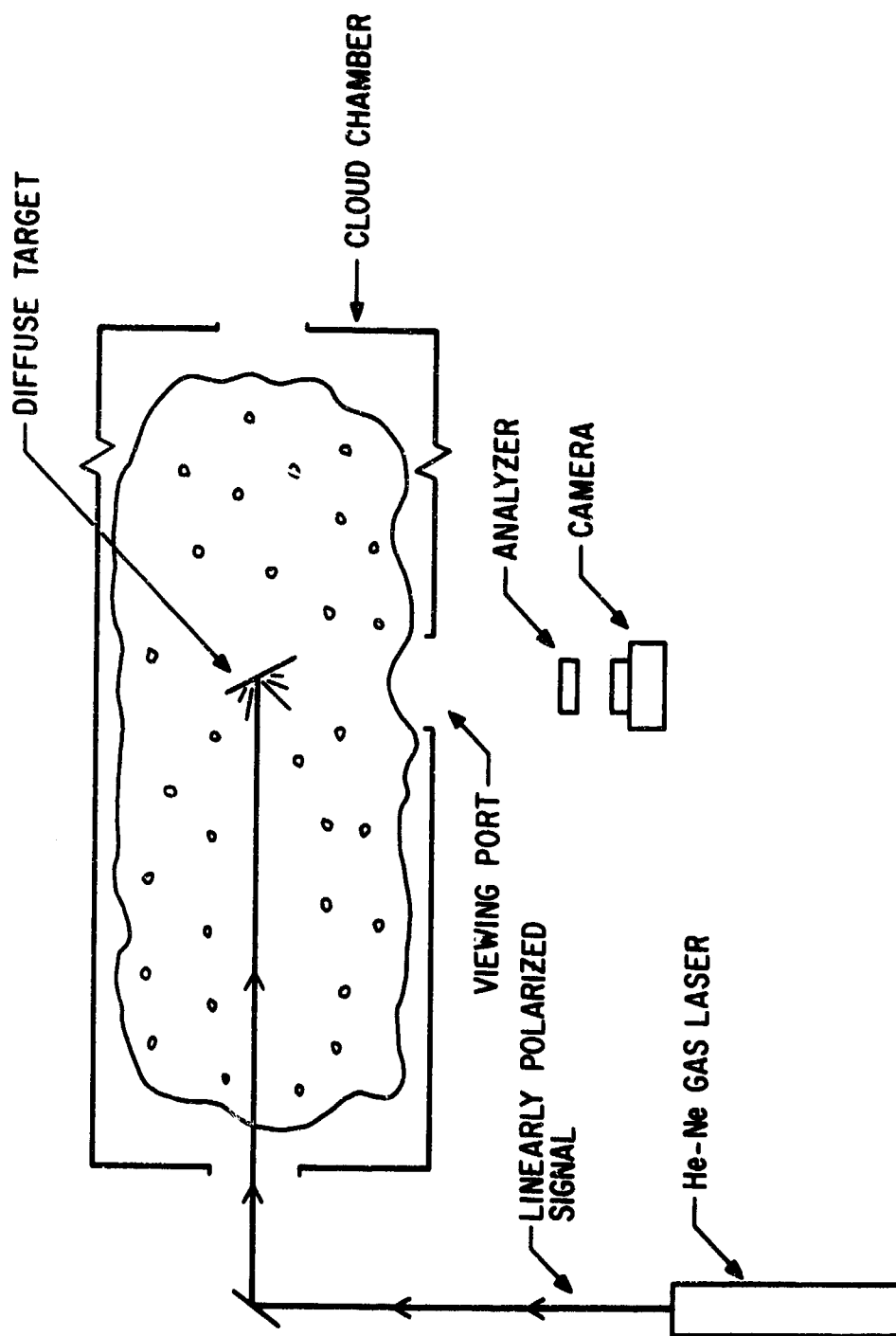
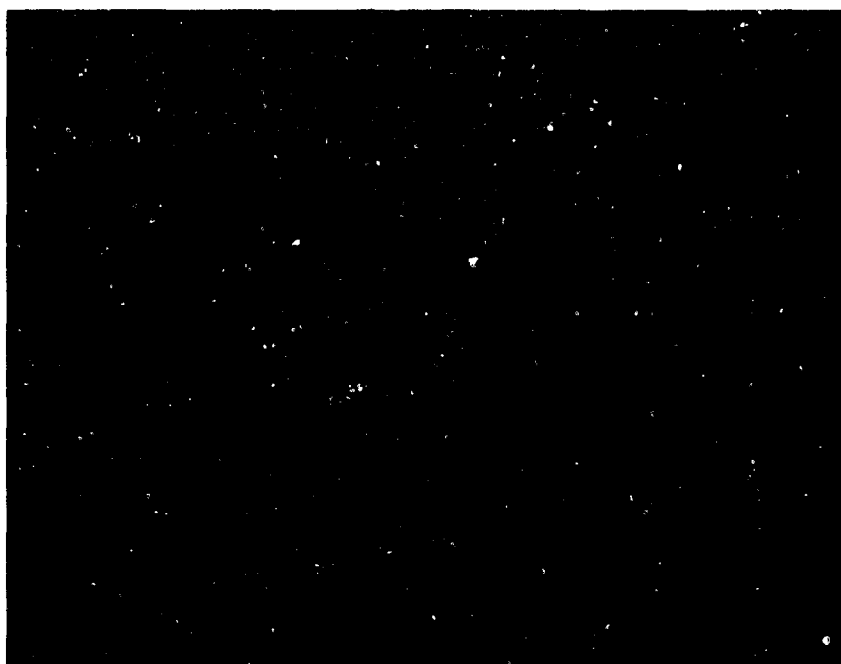


Figure 16. Experimental Arrangement for Photographs of Fig. 17



(a)



(b)

Figure 17. Photographic Illustration of the Cloud/Target Polarization Discrimination Technique. (a) Laser Output Linearly Polarized, No Analyzer on Camera; (b) Laser Output Linearly Polarized, Plane of Polarization of Analyzer (Located at Camera) Orthogonal to That of Transmitted Beam.

Beam enters at left side of each photograph. Target holder visible in lower part of each photograph.

of the cloud (as seen through the viewing port) that is not illuminated by the laser beam. The photograph shown in Fig. 15b was taken with the analyzer positioned in front of the camera and oriented so that its plane of polarization was perpendicular to the plane of polarization of the transmitted beam. The small, irregularly shaped red spot in the center of the photograph represents the sum of (a) those components of the radiation reflected from the target whose plane of polarization was orthogonal to that of the transmitted wave, (b) a negligible amount of multiple scattered radiation whose plane of polarization is orthogonal to that of the transmitted wave, and (c) a negligible amount of radiation whose plane of polarization is parallel to that of the transmitted wave (some of the radiation with parallel polarization is not completely attenuated by the non perfect analyzer).

A more vivid and explicit representation of the discrimination technique is depicted in the photographs shown in Fig. 17. The experimental arrangement illustrated in Fig. 16 was used to obtain the photographs shown in Fig. 17. For this situation the laser beam was transmitted along the long dimension of the cloud chamber and impinged upon the diffuse target which was placed opposite a side viewing port. The target was mounted on a tubular holder and inclined at an angle of 45° with respect to the transmitted beam. The camera was positioned opposite the side viewing port as shown in Fig. 16. Again, as in the previous set of photographs, the analyzer was placed in front of the camera with its plane of polarization perpendicular to that of the transmitted wave. The transmitted beam enters at the left side of each photograph (not visible in Fig. 17b). The target holder is visible in the lower part of

each photograph. In Fig. 17a we see that when no polarizer was used, the intensity of the scattered radiation completely concealed the target from view. However, in Fig. 17b we observe that the use of the analyzer attenuated the scattered radiation seen by the camera to such an extent that the target is partially visible.

The series of photographs shown in Figs. 15 and 17 clearly verify the validity of the polarization discrimination concept. According to the Mie theory of scattering, if a linearly polarized electromagnetic plane wave is incident on a spherical particle of arbitrary composition and size, then the scattered radiation is also linearly polarized for all scattering angles (i.e. $0^\circ \leq \theta \leq 180^\circ$) in the XZ and YZ planes defined in Fig. 1. On the other hand, the radiation reflected (scattered) from a diffuse (rough) surface will, in general, be depolarized. For the photographs shown in Fig. 15 the camera was in the XZ plane and $\theta = 180^\circ$. We see, then, that the observed scattering phenomena shown in Fig. 15a and b are in good agreement with the Mie and rough surface theory of scattering. For the photographs shown in Fig. 17 the camera was in the YZ plane; and while the point of observation was on a line normal to the direction of propagation of the transmitted wave, we can assume that the scattering angle varied over a wide range of values. This can be seen from a comparison of Fig. 17a and Fig. 17b. Figure 17a is a photograph of the sum of the individual electromagnetic waves scattered out of the beam (within the field of view of the camera) along the direction of propagation of the transmitted signal. Each of these component waves had a different direction of propagation (scattering angle) in the YZ plane which was determined by the location and size of the scattering particles. As shown in Fig. 17b, the analyzer (its plane of polarization

crossed with respect to that of the transmitted signal) completely attenuated the scattered radiation surrounding the beam while transmitting the perpendicular component of the radiation reflected from the target. We can assume, then, that the scattered radiation was of the same polarization as that of the transmitted signal and was independent of the scattering angle (direction of observation). This series of photographs, then presents a qualitative justification for our experimental program.

Originally, the experimental verification phase of this effort was to be performed primarily in the laboratory and if the results warranted, would be expanded to include a flight test program in the field evaluation phase of the effort. However, since the initiation of the laboratory effort, an aerial tramway facility was constructed in the Sandia Mountains at Albuquerque, New Mexico. This facility has provided an exceptional opportunity for performing laboratory experiments in an actual atmospheric environment. The program was justifiably expanded to include tramway experiments and the results, to date, are presented in section 6.3.

6.2 CLOUD CHAMBER EXPERIMENTS

The experimental arrangement shown in Fig. 18 was used for the He-Ne laser polarization discrimination experiments. The well collimated light ($\lambda = 6328$ Angstroms) output from a He-Ne gas laser was beamed into an electro-optic (KDP crystal) modulator, the output of which was directed through a Glan-Thompson prism and special mirror into and along the long dimension of the cloud chamber. Even though the output of the laser is linearly polarized, we used the Glan-Thompson prism to ensure a high degree of polarization. The ratio of the intensities of the orthogonally polarized and parallel polarized components (I_{o1}/I_{p1}) at the output of the Glan-Thompson prism was measured to be 5.2×10^{-4} . The special mirror

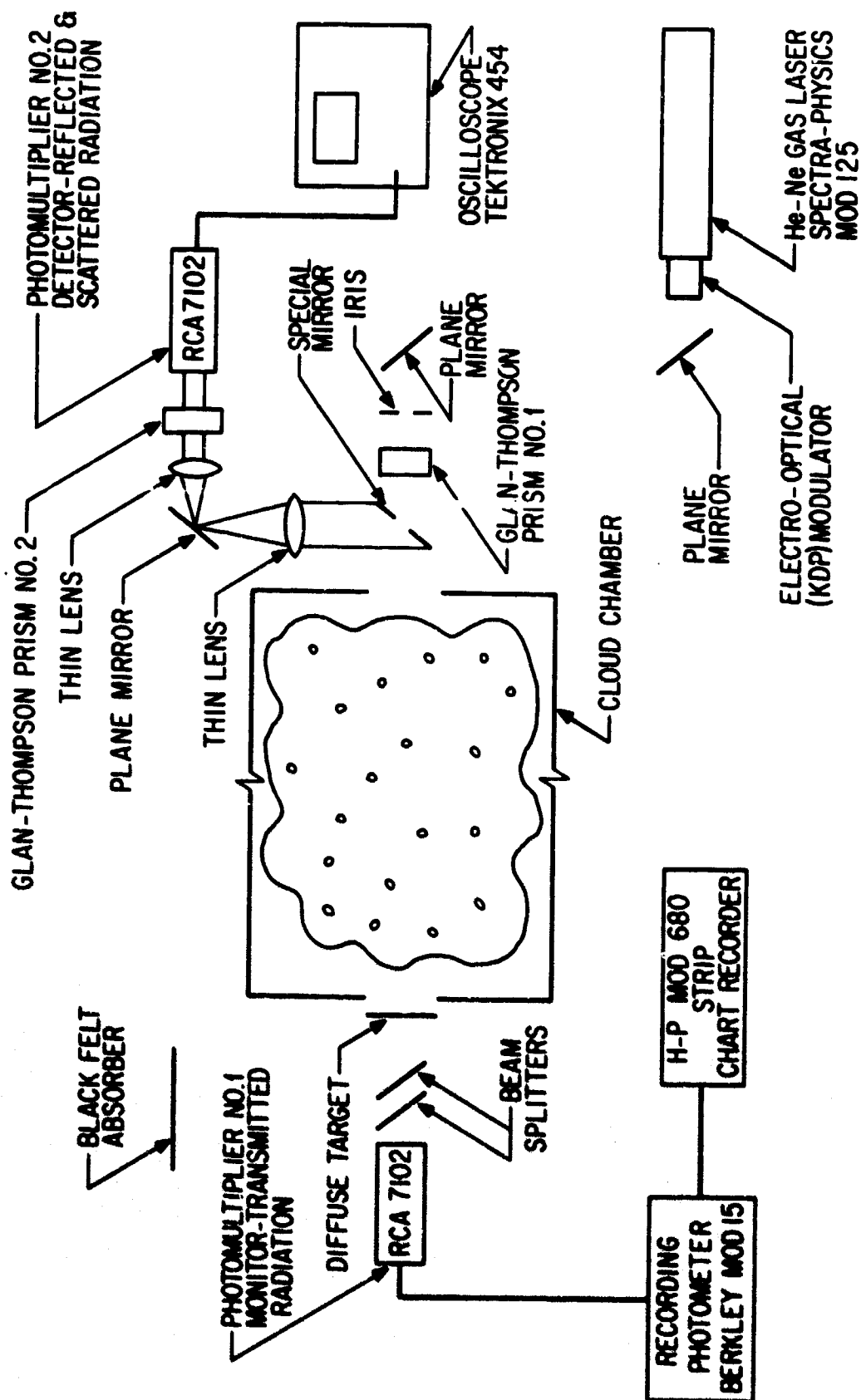


Figure 18. Experimental Arrangement for He-Ne Laser Cloud Scattering Experiments

is just an optical flat with a hole cut through it to allow the passage of the transmitted beam. The intensity of the transmitted beam is monitored at the target end of the chamber by a collimated transmission detector (RCA PMT No. 7102) and is continuously displayed on a strip-chart recorder (Hewlett-Packard Model 680). Two beam splitters are used to attenuate (by reflection) the signal so as to prevent any saturation of the detector. They each have a rated transmission of 5 percent. The black felt absorber is inclined at 45° with respect to the direction of propagation of the reflected beams and is used to prevent the energy reflected by the beam splitters from entering the detection system. The reflected radiation from the target and the backscattered radiation from the cloud were collected on the special mirror, collimated by the thin lenses, and directed through another Glan-Thompson prism onto the photocathode of an S-1 photomultiplier tube (RCA No. 7102) the output of which was monitored and photographed on a Tektronix Model 454 oscilloscope.

We chose a MgO (magnesium oxide) coated surface as a standard target because of the high and almost perfectly diffuse reflectance of MgO. For our particular MgO target, the coefficient of reflection $\rho = 0.98$ and the average value of the ratio of the measured intensities of the orthogonally polarized and parallel components ($I_{\perp} / I_{\parallel}$) was equal to 0.324. In all experiments where the target was used, the target intercepted all of the incident beam (which was well collimated at the input of the chamber).

For every experiment the total intensity (I_{tot}) and the individual intensities of the orthogonally polarized (I_{\perp}) and parallel polarized (I_{\parallel}) components of the radiation scattered from the target were measured before generating a cloud, and again after the cloud had completely dissipated. The average values of these measured intensities were used as a

standard reference for all cloud return measurements. In measuring the total intensity, I_{t+} , Glan-Thompson prism No. 2 was removed and the measured value had to be corrected for a 7 percent loss in the prism.

In preliminary experiments we attempted to determine the relationship between the target return and the transmissivity of the cloud. Theoretically, the transmissivity, τ , is defined from Equation (68) as

$$\tau = \frac{I}{I_0} = e^{-\sigma x} \quad (308)$$

Thus, if the target is a perfect diffuser, we see from Section IV and specifically Equation (285) that the received signal (assuming the receiver is located adjacent to the transmitter) is proportional to τ^2 . The experimental verification of the theory is shown in Fig. 19. The plane of polarization of Glan-Thompson prism No. 2 was oriented orthogonal to that of prism No. 1 to reduce the cloud return to a minimum. The transmissivity of the cloud was continuously monitored and when steady-state conditions were reached for a specific value of transmissivity, the MgO target was positioned as shown in Fig. 18 (which causes a momentary interruption in the monitoring of the transmission) and the amplitude of the target return was recorded from the oscilloscope. The target was then removed and the return from the cloud was recorded along with the transmissivity as read from the strip-chart recorder. Assuming a negligible contribution due to multiple scattering, the log of the difference in the oscilloscope readings is plotted against the log of the corresponding τ . It is evident from the resultant slope that the experimental data are in close agreement with theory and therefore we used the value τ^2 for subsequent calculations and comparisons.

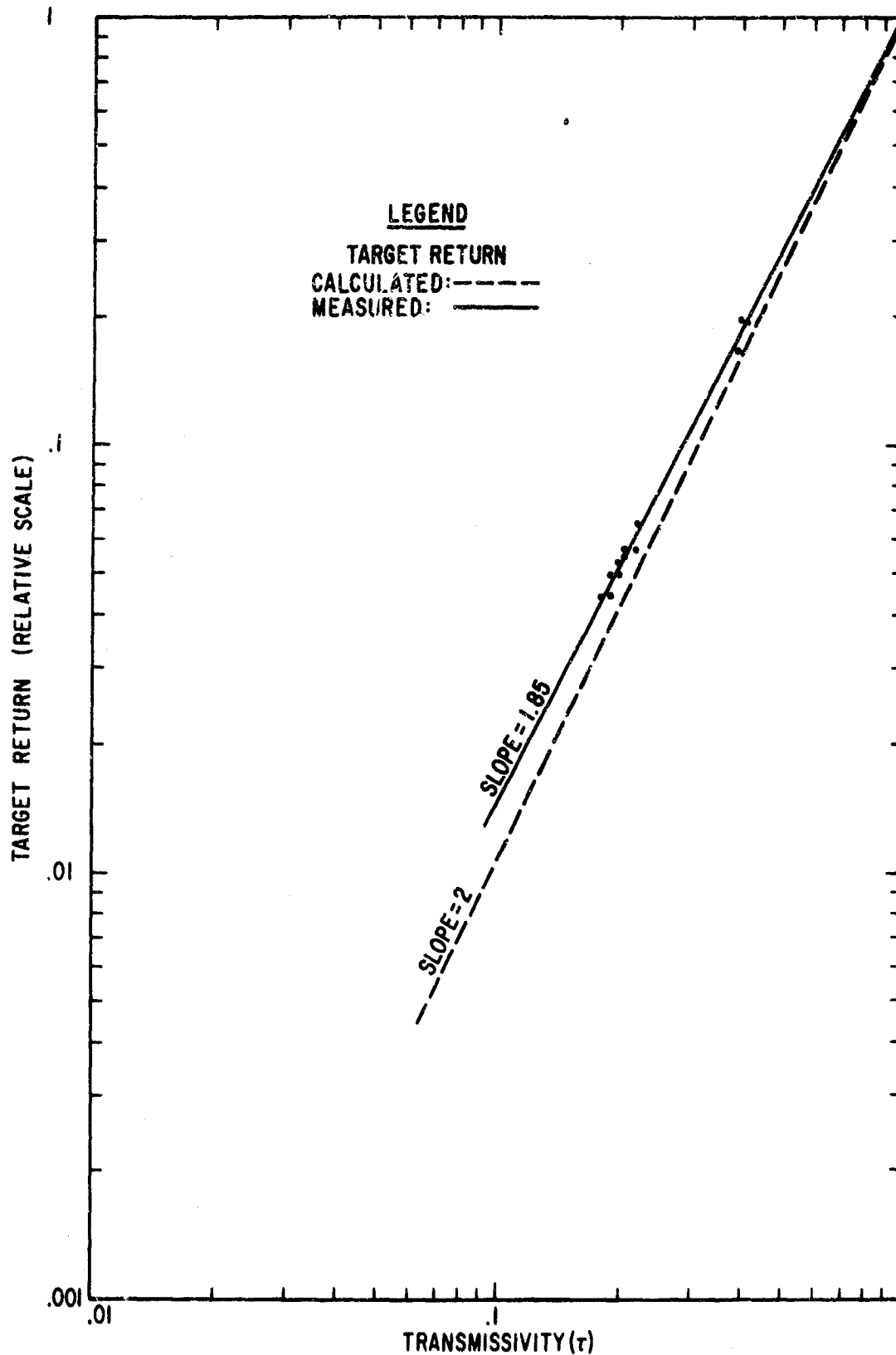


Figure 19. Target Return vs. Cloud Transmissivity

For the polarization discrimination experiments reference measurements (I_{t+} , $I_{t\perp}$, $I_{t\parallel}$) of the target return were made as previously discussed and then the target was removed. A cloud was generated and the individual pulse returns corresponding to the total intensity I_{c+} and the component intensities $I_{c\perp}$ and $I_{c\parallel}$ of the radiation scattered from the cloud were photographed on the oscilloscope. The corresponding value of τ was appropriately marked on the strip chart. The amplitudes of the photographed returns (both target and cloud) were measured, tabulated, and corrected for Glan prism losses when appropriate. All values were then normalized to a clear air ($\tau = 1$) target return where $I_{t+} = 1$, $I_{t\parallel} = 0.55$, and $I_{t\perp} = 0.245$. These ratios were calculated from the relationships $I_{t+} = I_{t\perp} + I_{t\parallel}$ and $I_{t\perp}/I_{t\parallel} = 0.324$. Plots of $\log I$ vs. $\log \tau$ for the cloud returns and their corresponding target returns are shown in Figs. 20 through 22. A composite plot is shown in Fig. 23.

It is easily seen from Figs. 20, 21, and 23 that, when no analyzer was used on the receiver or when the plane of polarization of the analyzer was parallel to that of the transmitted signal, the cloud return was greater than the target return for $\tau < 0.5$ (approximately). On the other hand, even though the intensity of the target return was much lower when the plane of polarization of the analyzer was orthogonal to that of the transmitted signal, the cloud return was reduced over an order of magnitude and was greater than the target return only when $\tau < 0.28$. We see from Figs. 22 and 23 that for decreasing values of τ there was a corresponding increase in $I_{c\perp}$. This continuous increase in $I_{c\perp}$ was due to the partial depolarization of the scattered radiation caused by an increase in multiple scattering at the higher cloud densities.

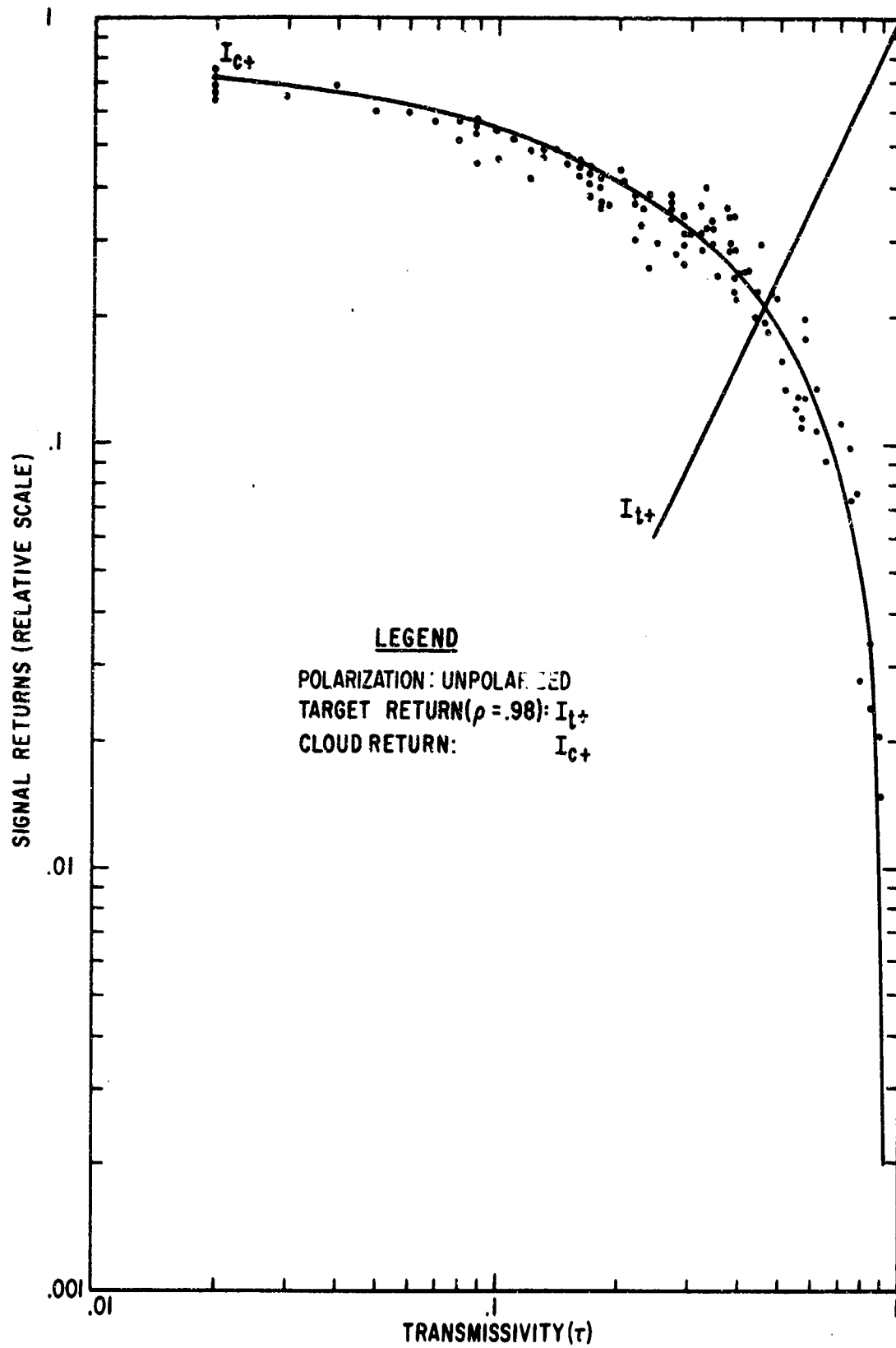


Figure 20. Target and Cloud Returns vs. Cloud Transmissivity

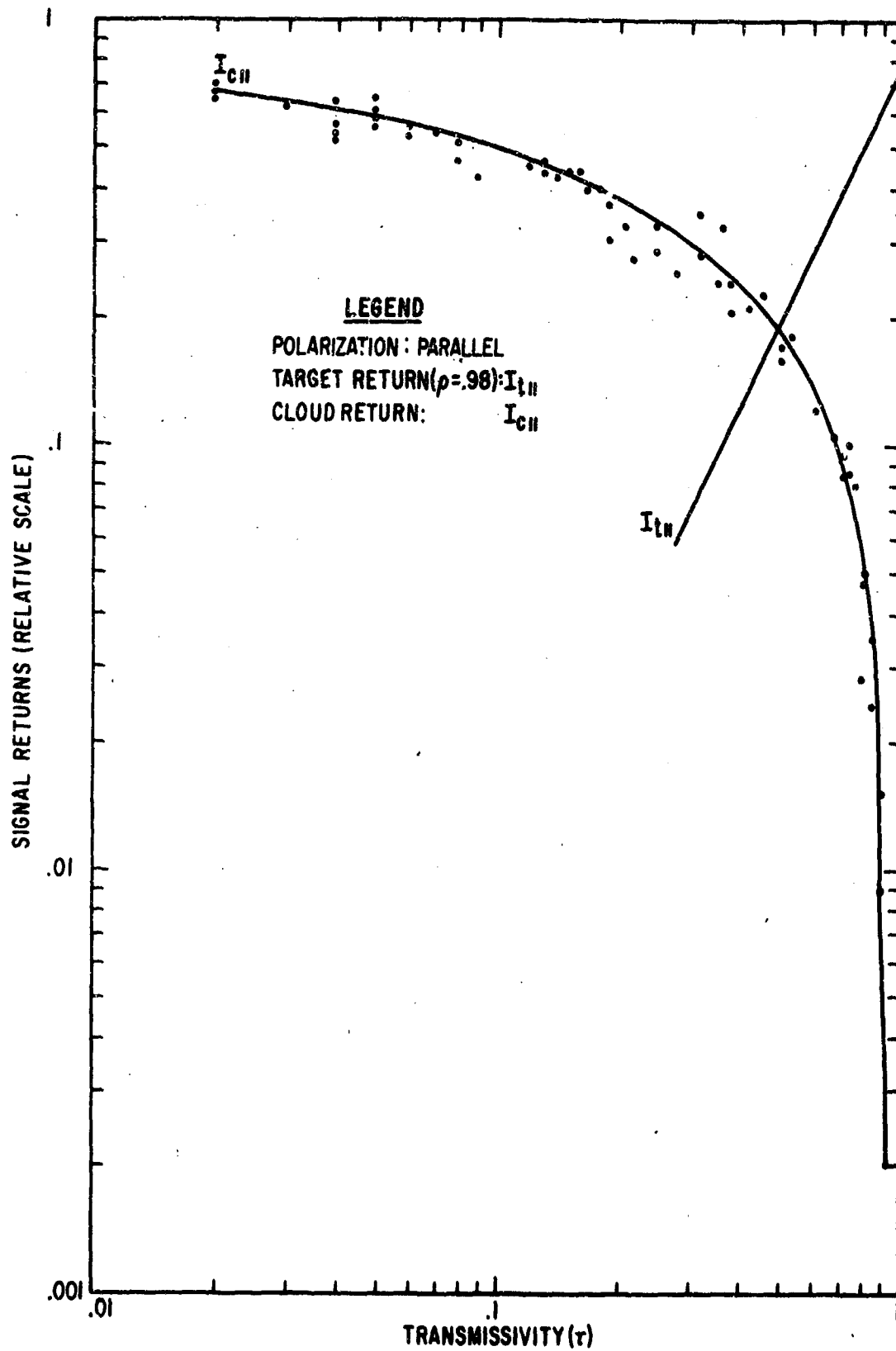


Figure 21. Target and Cloud Returns vs. Cloud Transmissivity

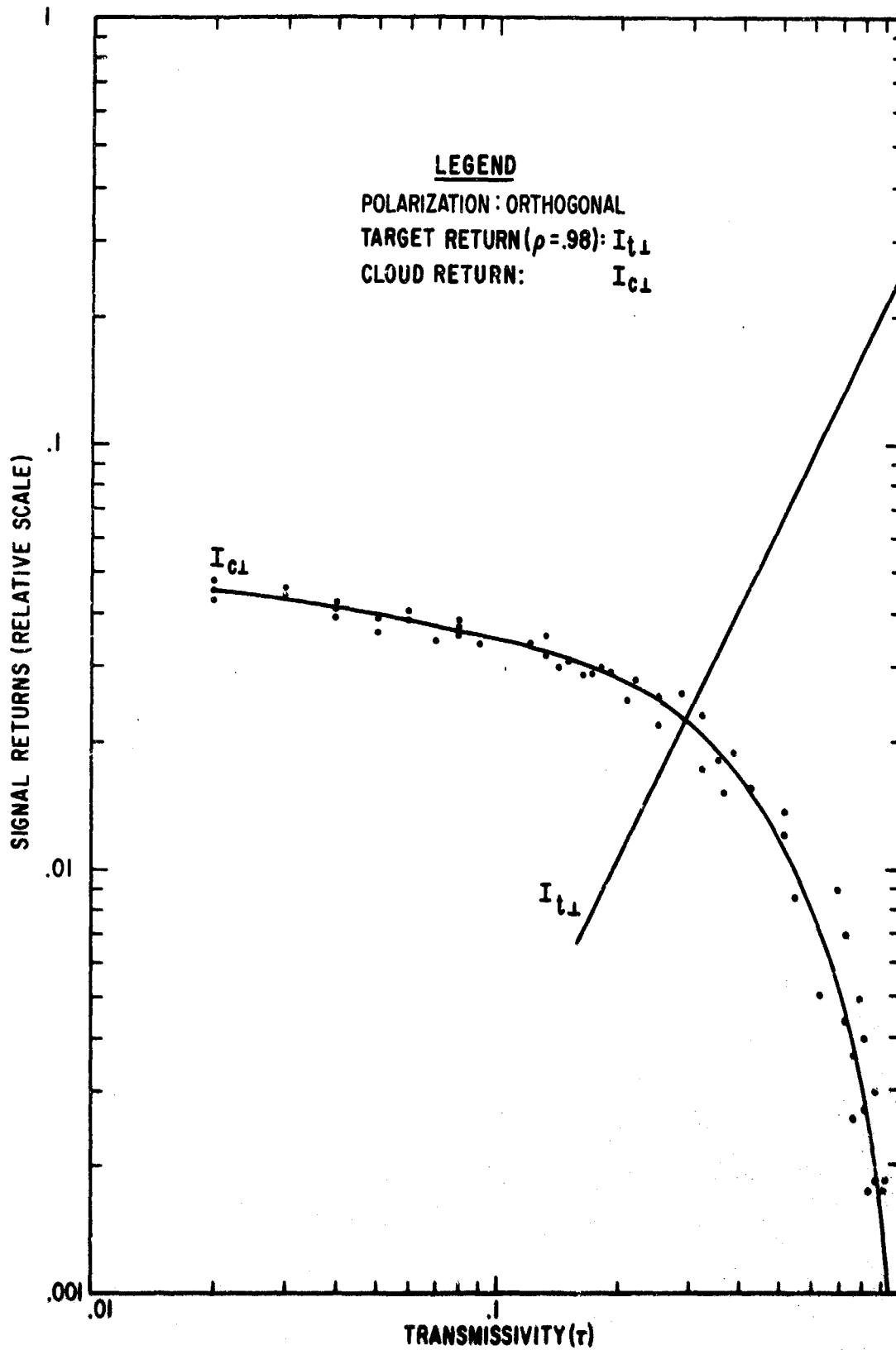


Figure 22. Target and Cloud Returns vs. Cloud Transmissivity

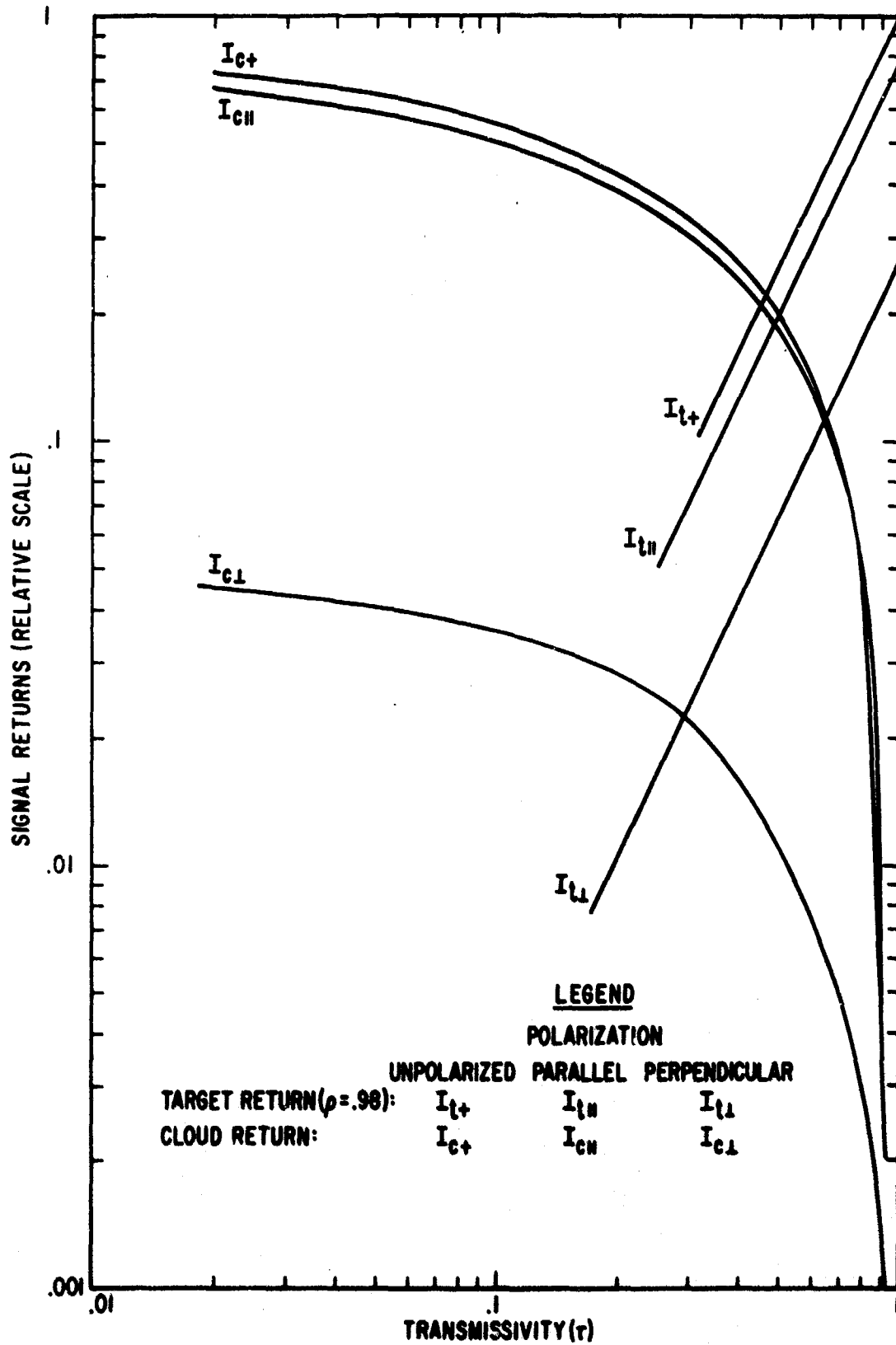


Figure 23. Target and Cloud Returns vs. Cloud Transmissivity

It is apparent, though, that I_{cl} approaches an asymptotic limit as the density increases indicating that the cloud is beginning to resemble a solid rather than an extended target.

The experimental arrangement shown in Fig. 24 was used for the Ruby laser ($\lambda = 6943$ Angstroms) polarization discrimination experiments. We were not able to obtain any meaningful data from this phase of the program, however, because the amplitude of the transmitted signal varied erratically from pulse-to-pulse. The amplitude difference varied as much as 20 percent. This phase of the program was postponed until the source of the malfunction can be located and corrected.

6.3 SANDIA PEAK AERIAL TRAMWAY EXPERIMENTS

The Sandia Peak Aerial Tramway provides an exceptional capability for performing laboratory experiments in an actual atmospheric environment. It is the longest aerial tramway in North America, the distance between the lower and upper terminals being 2.7 miles. The difference in elevation between the lower (elevation: 6550 feet) and upper (elevation: 10378 feet) terminals is 3828 feet. Two 60-passenger cabins move simultaneously on separate cables but in opposite directions (one moves toward the upper terminal as the other approaches the bottom). The distance between a cabin and the terrain directly below varies considerably (from 50 to 1000 feet) as the cabin travels next to and over rocky granite spires, cliffs, and pinnacles, across gullies and ravines formed by the spring runoffs, and over steep and heavily-forested canyons and valleys. In traveling from the base to the top of the mountain, the tramway passes over four of the earth's seven climatological life zones. The corresponding species of trees vary from

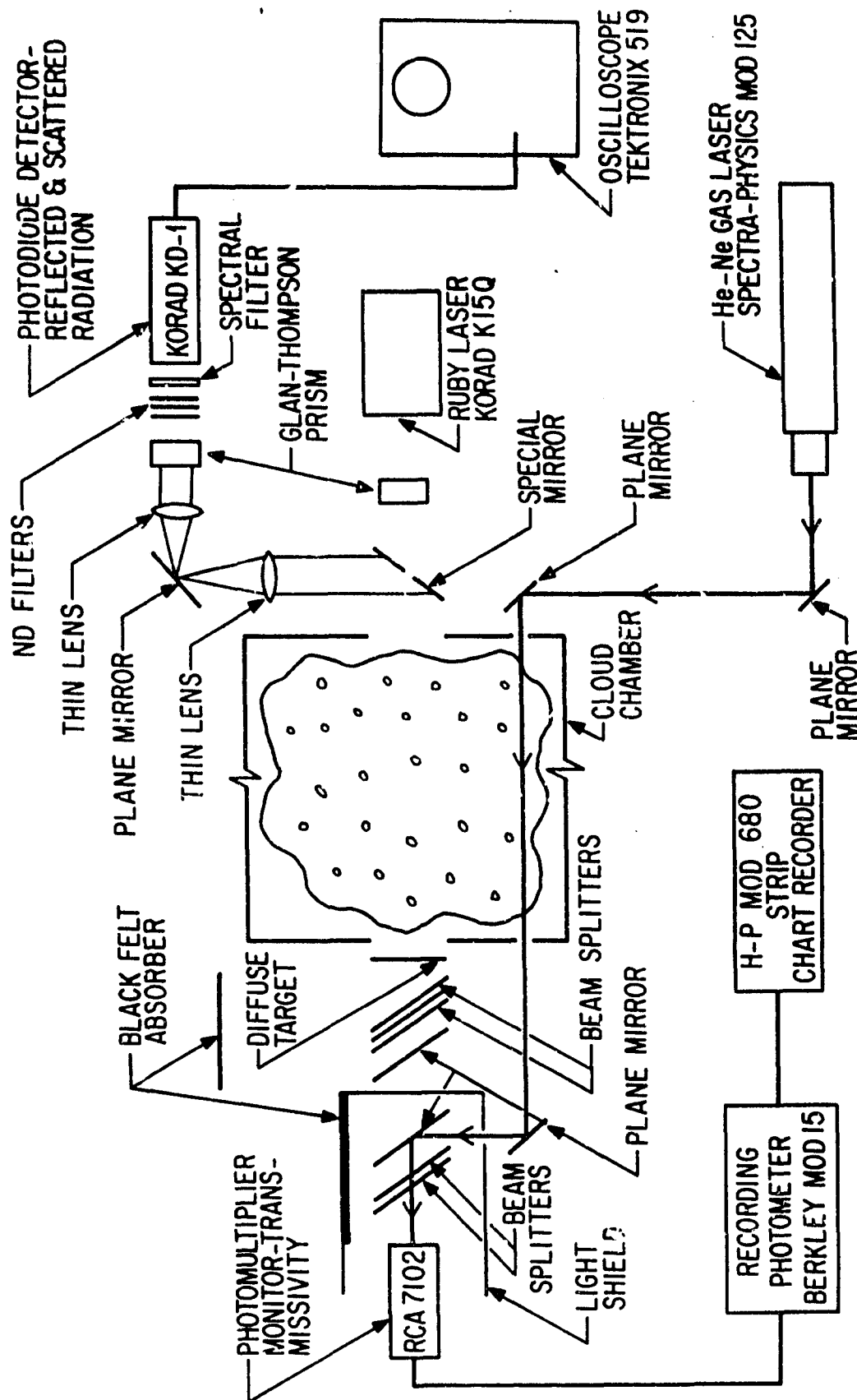


Figure 24. Experimental Arrangement for Ruby Laser Cloud Scattering Experiments

clusters of live oak, pinon, and juniper at the lower terminal to stands of ponderosa pine, spruce, fir, and aspen between the lower and upper terminals. In addition, many varieties of wild flowers, shrubs, grasses, and succulent plants grow on the west side of the mountain.

Even though the weather in the Albuquerque vicinity is usually clear and sunny, there are many days throughout the year when Sandia Mountain (including the tramway facility) is enveloped in clouds. While the degree of cloudiness does not appear to have a diurnal variation, there is a definite seasonal variation. There appears to be a predominance of high cumulus type rain clouds in the early spring and late summer, while in the winter, stratus type (including fog) clouds appear to be the most numerous. The bases of the spring and summer clouds are usually higher than 10,000 feet while in the winter the bases are generally much lower, varying from near the ground (fog) to 8000 feet.

A typical view of one of the tramway cabins and the surrounding terrain on a partially cloudy morning is shown in Fig. 25.

For the tramway experiments we used a portable battery-operated ladar system specifically designed for use in the field. The primary components of the system are the following:

- a. Source: GaAs (gallium arsenide) semiconductor laser and pulse driver (IBM Corp.)
- b. Detector: S-1 response photomultiplier tube (RCA Development type C70102B)
- c. Receiver: solid state amplifier
- d. Polarizers: Glan-Thompson
- e. Optics: appropriate mirrors, lenses, spectral filters, neutral



COURTESY JERRY ROSE STUDIO ALBUQUERQUE, NEW MEXICO

Figure 25. Typical View of Sandia Tramway Cabin on Partially Cloudy Day.

density filters, etc.

f. Range Indicator: nixie tube digital display (XM23 Time Interval Counter Range Finder, IBM Corp.)

Additionally, the output of the amplifier was displayed on a Tektronix Model 454 oscilloscope. A Polaroid-Land camera was used for photographing the signal returns.

A view (inside of a tram cabin) of the experimental arrangement used for the tramway experiments is shown in Fig. 26. A complete ladar system including the XM23 nixie tube display unit is mounted on the tripod. A similar system without the XM23 unit is mounted on a tripod base and is directed through an opening in the floor of the tram cabin.

A representative sample of the data obtained from the tramway experiments is shown in Figs. 27 through 29. For all photographs the tram cabin was enveloped in clouds with the type of cloud varying from very dense fog to very dense stratus. The visibility varied from 10 to 20 feet. A representative view of the weather conditions is shown by the photograph in Fig. 30. The ladar unit was mounted on the tripod base located at the opening in the floor of the tram cabin, and positioned so that the direction of propagation of the transmitted signal was toward the snow-covered terrain below. The distance between transmitting and receiving apertures was 4 inches. The laser was operated at an output power (peak) of 320 watts at a pulse repetition frequency of 20 Hertz. The beamwidth of the transmitter and the field of view of the receiver were 3 degrees. A 300-Angstrom spectral filter was used on the receiver to reduce the back ground noise. For the photographs in Figs. 27a, 28a, and 29a the plane of polarization of the analyzer (located at



Figure 26. Interior View of Sandia Tramway Cabin Showing Experimental Arrangement Used For Laser Cloud Scattering Experiments.

NOT REPRODUCIBLE

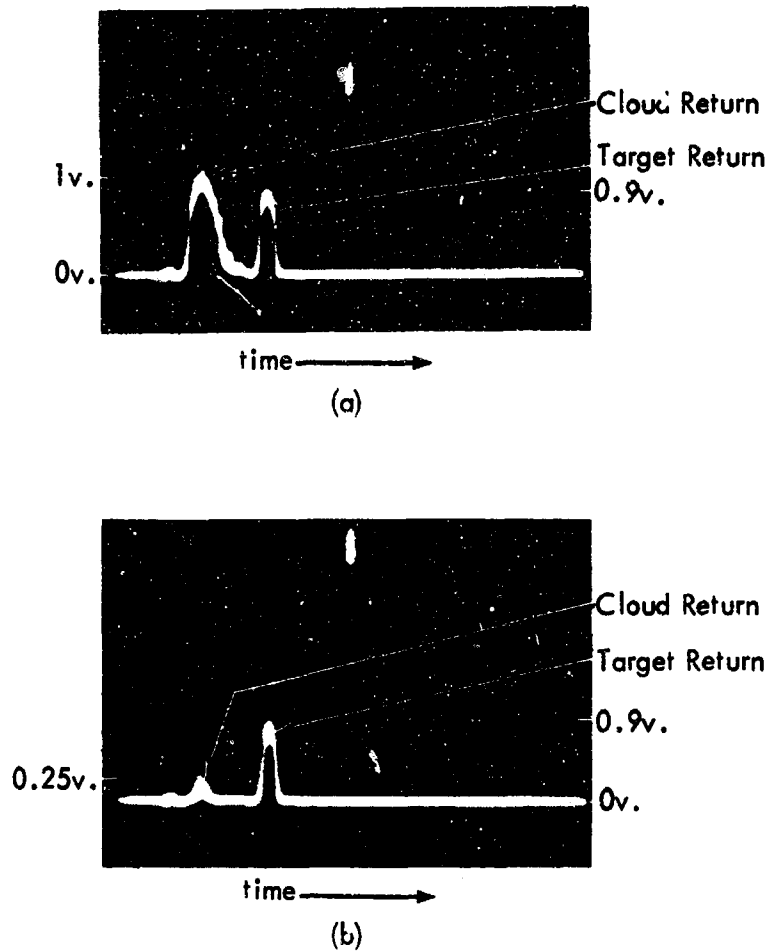


Figure 27. Oscillogram of Cloud and Target Returns. (a) Laser Transmitter Output Linearly Polarized, Plane of Polarization of Analyzer (Located at Receiver) Parallel to That of Transmitted Signal; (b) Laser Transmitter Output Linearly Polarized, Plane of Polarization of Analyzer (Located at Receiver) Orthogonal to That of Transmitted Signal. Vertical Sensitivity: .5v/div; Sweep Rate: 100 nanosec/div. Range: Cloud \approx 75 ft., Target \approx 150 ft.

NOT REPRODUCIBLE

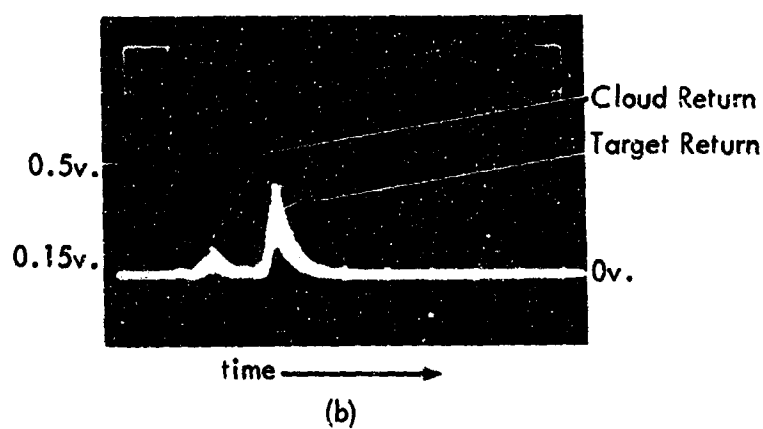
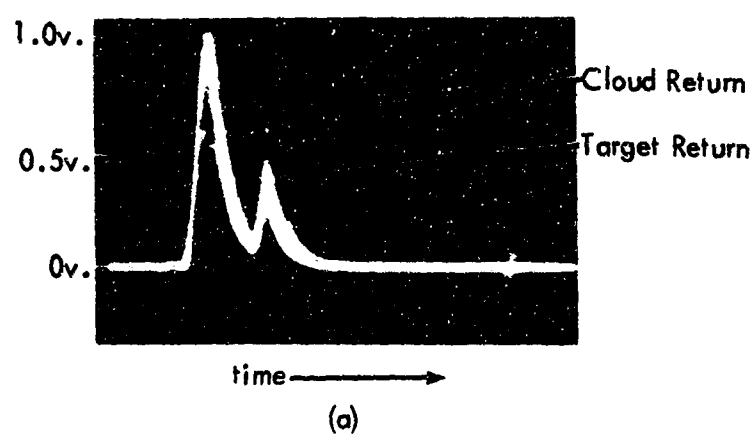
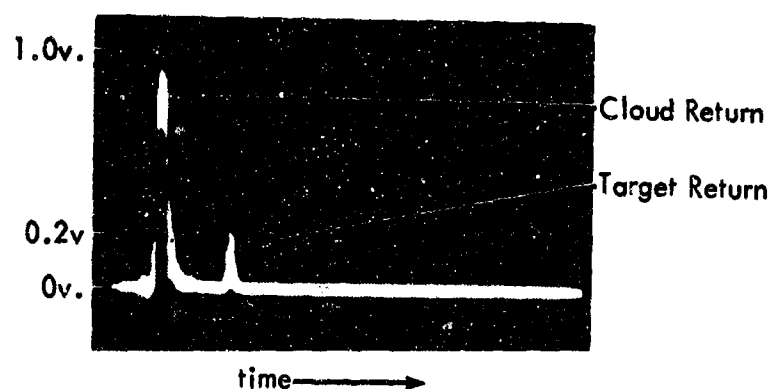
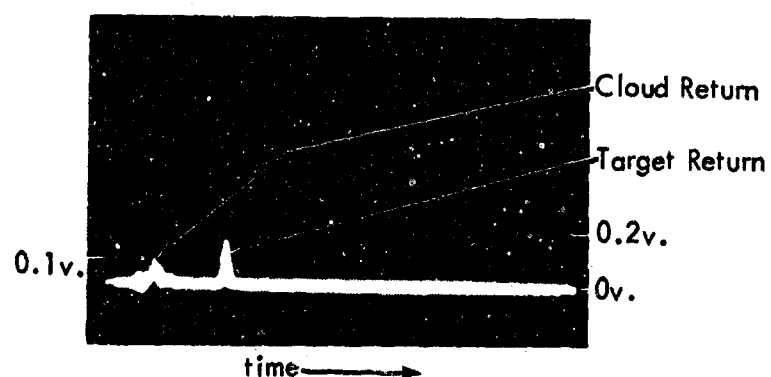


Figure 28. Oscillogram of Cloud and Target Returns. (a) Laser Transmitter Output Linearly Polarized, Plane of Polarization of Analyzer (Located at Receiver) Parallel to That of Transmitted Signal; (b) Laser Transmitter Output Linearly Polarized, Plane of Polarization of Analyzer (Located at Receiver) Orthogonal to That of Transmitted Signal. Vertical Sensitivity: .2v/div; Sweep Rate: 100 nanosec/div. Range: Cloud \approx 100 ft., Target \approx 175 ft.

NOT REPRODUCIBLE



(a)



(b)

Figure 29. Oscillogram of Cloud and Target Returns. (a) Laser Transmitter Output Linearly Polarized, Plane of Polarization of Analyzer (Located at Receiver) Parallel to That of Transmitted Signal; (b) Laser Transmitter Output Linearly Polarized, Plane of Polarization of Analyzer (Located at Receiver) Orthogonal to That of Transmitted Signal. Vertical Sensitivity: .2v/div; Sweep Rate: 200 nanosec/div. Range: Cloud \approx 80 ft., Target \approx 250 ft.



COURTESY JERRY ROSE STUDIO ALBUQUERQUE, NEW MEXICO

Figure 30. Typical View of Sandia Tramway Cabin Enveloped in a Dense Stratus Cloud. Camera Was Approximately 50 ft. from Cabin.

the receiver) was parallel to the plane of polarization of the transmitted signal. In all photographs the first return represents the radiation backscattered from the cloud while the second return represents the radiation reflected by the terrain (target). The difficulty in discriminating between the cloud return and the target return by conventional pulse discrimination techniques is obvious, and the photographs clearly illustrate the validity of the polarization discrimination concept. In addition, a comprehensive evaluation of the data revealed that: (a) while the target (terrain) return varied in range, the cloud return remained constant (approximately) in range and appeared to originate at a distance of $75(\pm 15)$ feet irrespective of the density of the cloud, and (b) the terrain return appeared to be depolarized for all varieties of vegetation (whether covered with snow or not).

SECTION VII

DISCUSSION

7.1 SUMMARY AND CONCLUSIONS

The use of laser detection and ranging systems in the atmosphere is seriously limited by the severe attenuation of the signal due to absorption by atmospheric gases and/or scattering by cloud and fog particles. Furthermore, the cloud and fog particles may scatter the transmitted radiation in the direction of the receiver, thus producing a false return. This false return must be distinguished from the true target return. The use of range-gating techniques to eliminate the cloud returns is unacceptable in the majority of applications and any electronic discrimination technique based on determining the difference in characteristics between the cloud and target returns would probably be very complicated, if not impossible, to implement. What is needed, then, is a cloud/target discrimination technique that while being physically realizable is also reliable and inexpensive to implement.

The purpose of the investigation described in this report was to determine the feasibility of using an optical technique for discriminating between a cloud return and a target return. Mie [Ref. 42] has shown analytically that if a linearly polarized, monochromatic electromagnetic plane wave propagating through a homogeneous medium is incident upon a single spherical particle the diameter of which is on the same order of magnitude as the wavelength of the incident radiation, then the scattered radiation is, in general, either linearly or elliptically polarized depending on the plane of observation. Other investigators

have extended (but not analytically) the Mie theory to a homogeneous medium (such as atmospheric cloud) containing a size distribution of independently scattering particles. Beckmann and Spizzichino [Ref. 4], on the other hand, have shown that if a linearly polarized, monochromatic electromagnetic plane wave is incident on an arbitrarily inclined rough surface, then the scattered radiation will, in general, be depolarized if the radius of curvature of the surface irregularities is large compared to the wavelength of the incident radiation. Since the majority of useful lasers emit radiation in the visible or near infrared portion of the electromagnetic spectrum, atmospheric clouds or fogs actually represent Mie scattering media and most targets—earth terrain including man-made irregularities, airborne objects such as aircraft, etc.,—can be considered to have rough surfaces at these wavelengths. One possible method, then, of distinguishing a cloud return from a target return could be based on the difference in the polarization characteristics of each return. Specifically, if the transmitter output of a laser detection and ranging system is linearly polarized and a polarizer (analyzer) is placed at the input to the receiver (assumed to be located adjacent to the transmitter) with its plane of polarization orthogonal to that of the transmitted wave, the receiver will "see" only the component of the radiation reflected from the target whose electric vector vibrates at right angles to the electric vector of the transmitted wave. All other returns—due to scattering from cloud particles and the parallel polarized component of the radiation reflected from the target—will be eliminated by the analyzer.

The results of the theoretical and experimental investigation described in the previous chapters verify conclusively the validity of the cloud/target polarization discrimination concept. In the laboratory phase of the program a linearly polarized signal from a He-Ne gas laser was propagated through an artificially produced cloud. The total intensity and the corresponding intensities of the parallel and perpendicular electric field components of the radiation scattered out of the laser beam by the cloud particles were measured as a function of the transmissivity, τ , of the cloud. The resultant cloud return data was normalized to a clear air reference target return. Plots of $\log I$ vs. $\log \tau$ for the cloud returns and their corresponding target returns are shown in Figs. 20 through 23. These curves show that for $\tau > 0.75$ the entire cloud-scattered radiation is polarized the same as the transmitted signal (i.e. $I_{c||} = I_{c+}$), and that for $\tau < 0.75$ almost all of the cloud return is polarized the same as the transmitter except for a small portion that is cross polarized relative to the transmitted signal (i.e. $I_{c||} \neq I_{c+}$). These results indicate that for $\tau > 0.75$ single scattering prevailed while for $\tau < 0.75$ the backscattered radiation was partially depolarized due to multiple scattering. Thus, these curves verify that for less dense clouds the cloud-scattered radiation is almost in exact agreement with the Mie Theory (all of the backscatter is polarized the same as the transmitted wave); whereas, for more dense clouds there is some back-scattered radiation cross polarized relative to the transmitter polarization. This partial depolarization of the cloud return at the higher cloud densities was caused by an increase in the multiple scattering. In Figs. 22 and 23 we see that while the intensity of the cross-polarized

component (I_{cl}) of the backscattered radiation should be zero, it in fact increases as the density of the cloud increases indicating the presence of depolarization effects due to multiple scattering. Additional evidence supporting our conclusion that the partial depolarization of the cloud returns was caused by multiple scattering is given by van de Hulst [Ref. 54]. He states that for an atmospheric cloud single scattering prevails for less dense clouds ($\tau > 0.9$); whereas, the effects of multiple scattering may be observed in the range $0.74 < \tau < 0.90$, multiple scattering definitely occurs in the more dense clouds when $\tau < 0.74$. We conclude, then, that the laboratory produced cloud actually represents a Mie scattering media whose scattering characteristics simulate a naturally occurring atmospheric cloud. In addition, the size distribution of cloud particles, as determined from photomicrographs, indicates that the laboratory produced cloud simulates a low altitude atmospheric stratus cloud.

We see also from Figs. 20, 21, and 23 that, when no analyzer was used on the receiver or when the plane of polarization of the analyzer was parallel to that of the transmitted signal, the cloud return was greater than the target return for $\tau < 0.5$ (i.e. $I_{c+} > I_{t+}$ and $I_{c||} > I_{t||}$ for $\tau < 0.5$). On the other hand, in Figs. 22 and 23 we see that when the plane of polarization of the analyzer was orthogonal to that of the transmitted signal, the cloud return was reduced approximately 94 percent and was greater than the target return only when $\tau < 0.28$ (i.e. $I_{cl} > I_{tl}$ for $\tau < 0.28$). The data of Arnulf, et al, [Ref. 3], Carrier, et al, [Ref. 11], and other researchers indicate that the transmissivity

per meter of most clouds and fogs is usually between 70 to 90 percent. While the data, then, in Figs. 20 and 23 indicate that for transmissivities above 48 percent the target return will be greater than the cloud return, even when the analyzer is not used on the receiver, the target in this case (a block of MgO) was almost both a perfect reflector and a perfect diffuser. Most natural earth objects (water surfaces, coniferous forest, grass meadows, plowed fields, etc.) are very nearly perfectly diffuse targets at laser wavelengths; however, when compared to MgO they usually are poor reflectors (except possibly when covered with snow). The reflection coefficients of various earth surfaces is tabulated in the Smithsonian Meteorological Tables [Ref. 37] and the values vary from a low of 0.03 - 0.10 for water surfaces to a high of 0.03 - 0.25 for ground surfaces. The reflectance of fresh fallen snow varies from 0.70 to 0.86. The coefficient of reflection for man-made objects (roads, buildings, etc.) varies from 0.08 to 0.35 [Ref. 51].

The value of the discrimination technique when used in a realistic situation is illustrated in Fig. 31. Here we replotted the cloud returns, I_{c+} and I_{c1} , from Fig. 23 substituting for the MgO returns, two representative earth targets ($\rho = 0.10$ and $\rho = 0.25$). The earth targets are assumed perfect diffusers and their returns are normalized to the reflectance of the MgO target. These curves show that when no analyzer is used on the receiver, the cloud return will be greater than the return from a typically good reflecting target ($\rho = 0.25$) for $\tau < 0.65$ (i.e. $I_{c+} > I_{t+}$ for $\tau < 0.65$). Similarly, for an average reflecting target ($\rho = 0.10$) the cloud return will be greater than the target return (i.e. $I_{c+} > I'_{t+}$) for $\tau < 0.75$. On the other hand, if a

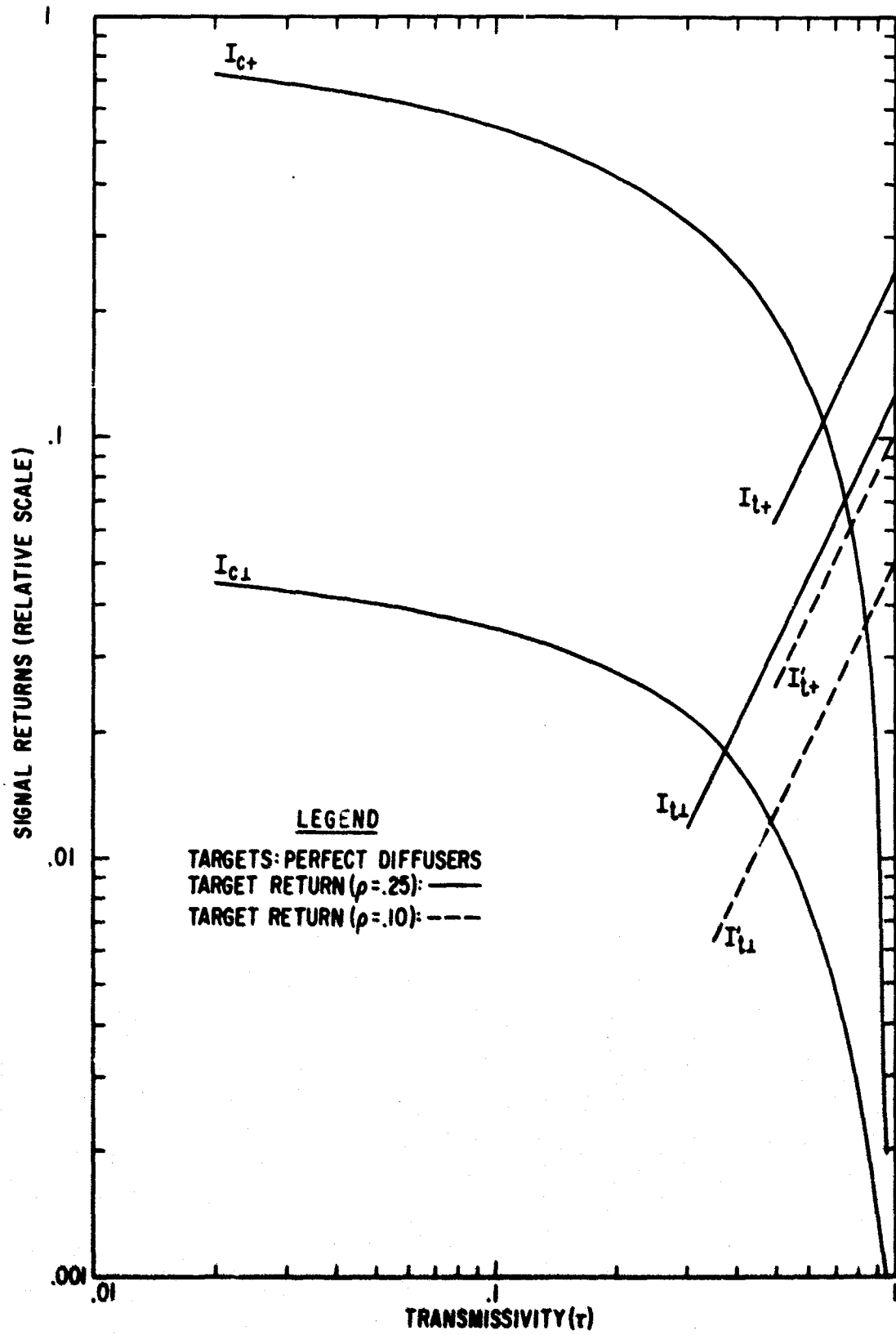


Figure 31. Target and Cloud Returns vs. Cloud Transmissivity for Realistic Earth Targets

polarizer is placed at the input to the receiver with its plane of polarization orthogonal to that of the transmitted signal, we see that the two target returns (I_{t1} and I'_{t1}) are greater than the cloud return (I_{c1}) for $\tau > 0.36$ and $\tau > 0.48$, respectively. These transmissivity levels correspond to very dense clouds which do not occur very frequently in the atmosphere. We conclude, then, that the use of the polarization technique will greatly improve the ability of a laser detection and ranging system to discriminate between the returns from an atmospheric cloud and a realistic target.

The data collected in the field evaluation phase of the experimental program clearly confirms the results of the laboratory investigation. The field tests were performed in one of the two cabins of the Sandia Peak Aerial Tramway. The cabin was used as a transmitter/receiver site and the terrain below the cabin was used as a target. The tramway experiments were conducted with a portable battery-operated GaAs (gallium arsenide) rangefinder system specifically designed for use in the field. A representative sample of the data obtained in the field evaluation phase is presented in Figs. 27 through 29. In Fig. 27, the relative intensity of the cloud return was reduced 80 percent when the plane of polarization of the analyzer was rotated 90 degrees; that is, the oscilloscope display of the cloud is reduced from $I_{c11} = 1v.$ (peak) in Fig. 27a, to $I_{c1} = 0.2v.$ (peak) in Fig. 27b. Similarly, in Figs. 28 and 29, the relative intensities of the cloud returns were reduced 75 and 90 percent respectively. The average reduction in the relative intensity of the cloud returns for all of the tramway data ranged between 75 to 90 percent. In addition, a comprehensive evaluation of the data

revealed that: (a) while the target (terrain) return varied in range, the cloud return remained constant in range (approximately) and appeared to originate at a distance of 75 (± 15) feet irrespective of the density of the cloud, and (b) the terrain return appeared to be depolarized for all varieties of vegetation (whether covered with snow or not). The expected signal returns from the cloud and the terrain below the tram car were calculated from Equation (285)

$$P_R = \frac{\rho P_T A_R e^{-2\sigma r} \cos \gamma}{\pi r^2} \quad (285)$$

and Equation (301)

$$P'_R = \beta(\pi) A_R I_o 2\pi \left(1 - \cos \frac{\theta_R}{2}\right) E_2(2\sigma) \quad (301)$$

where

$$I_o = \frac{4P_T}{\pi \theta_T^2} \quad (281)$$

and

$$E_2(2\sigma) = \int_{r_o}^r \frac{e^{-2\sigma x}}{x^2} dx \quad (300)$$

The receiver output voltage, V_R , was calculated from

$$V_R = N_R P_R S R_L A_V \quad (309)$$

Where N_R is the efficiency of the receiver optics, S is the sensitivity of the detector, R_L is the load resistance, and A_V is the gain of the receiver. The calculated values for the cloud and target returns were in good agreement with the measured values for an assumed terrain (target) reflectivity $\rho = 0.15$.

The following calculations are presented to illustrate the close correlation between the measured and calculated values of the cloud and target returns. Specifically, the measured values of the receiver output voltage for the cloud and target returns shown in Fig. 29 are compared to the calculated values where

$$\rho = 0.15$$

$$P_T = 320 \text{ watts}$$

$$A_R = \frac{\pi}{144} \text{ ft.}^2$$

$$\sigma = 0.015 \text{ m}^{-1} = .0045 \text{ ft.}^{-1}$$

$$\gamma = 45^\circ$$

$$r = 250 \text{ ft.}$$

$$r_0 = 2 \text{ ft.}$$

$$\theta_T = \frac{\pi}{60} \text{ rad.}$$

$$\theta_R = \frac{\pi}{60} \text{ rad.}$$

$$\beta(\pi) = 6 \times 10^{-4} \text{ m}^{-1} \text{-ster}^{-1} = 3.84 \times 10^{-7} \text{ ft.}^{-1}$$

$$E_2(2\sigma) \approx 0.49$$

$$N_R = 0.0315$$

$$S = 3100 \frac{\text{amps}}{\text{watt}}$$

$$R_L = 316 \Omega$$

$$A_V = 368$$

Substituting these values into the appropriate equations, we obtain the following values for the target return,

$$P_R = 3.77 \times 10^{-7} \text{ watts}$$

$$V_R = 0.4253 \text{ volts}$$

Similarly, for the cloud,

$$P_R = 1.3 \times 10^{-6} \text{ watts}$$

$$V_R = 1.47 \text{ volts}$$

The values of the receiver output voltages measured from Fig. 29 are

$$V_R = 0.4 \text{ volts (peak)}$$

$$V_R = 1.0 \text{ volt (peak)}$$

The calculated value of the receiver output voltage for the target return is in good agreement with the measured value. The measured value of the receiver output voltage for the cloud return is, however, almost 50 percent greater than the calculated value. The reason for this difference is that the detector was probably saturated by the cloud return.

The data collected from both the laboratory verification phase and the field evaluation phase of the program has definitely shown that the denominator of the polarization discrimination coefficient

$$PDC = \frac{\beta(\pi)}{\beta_{\perp}(\pi)} \quad (307)$$

can be physically made very small. This substantiates the assumption that the Mie theory of scattering (originally derived for a single sphere) is applicable to a homogeneous medium consisting of many scattering particles, not necessarily of the same size, such as the clouds that were generated in the laboratory and that were encountered in the field tests on board the tram.

7.2 RECOMMENDATIONS FOR FUTURE RESEARCH

(a) Mie presented his analytical solution for the field components of the radiation scattered from a linearly polarized monochromatic plane wave incident on a single homogeneous spherical particle in 1908. Since then many reserachers have extended the Mie theory to a homogeneous medium containing a size distribution of independently scattering particles. These expanded versions of the Mie theory are, in reality, only approximations based on simplifying assumptions that may not be valid. The ultimate use of the laser in present and proposed applications where the laser energy may be severely attenuated when propagating through a medium containing many scatterers will depend on the results of an accurate analysis of the interaction between the propagating wave and the scattering medium. An analytical solution based on electromagnetic theory is required, then, for the diffraction of a collimated beam of electromagnetic energy propagating through a medium consisting of many spherical (or similar shaped) particles, not necessarily of the same diameters. Furthermore, the effects of multiple scattering definitely should be included in the analysis.

(b) While the validity of the discrimination technique has been experimentally verified for two optical wavelengths (one in the visible and one in the infrared portion of the electromagnetic spectrum), a thorough analytical and experimental analysis of the wavelength dependence (if any) of the concept has not been performed. It has been shown by several researchers [Refs. 3, 11, 13] that the transmissivity of clouds and fogs is virtually independent of wavelength. While, on the

other hand, the transmissivity of haze increases rapidly with increasing wavelength until at 10 microns the haze becomes almost transparent [Refs. 3, 13]. Deirmendjian [Ref. 13] and Carrier, et al [Ref. 11] have shown that the backscattered radiation is definitely wavelength sensitive with the amount of backscatter decreasing as a function of increasing wavelength.

(c) Arnulf, et al [Ref. 3] has reported that the optical properties of artificial smoke are very similar to those of haze, that is, the transmissivity of artificial smoke increases with increasing wavelength and approaches 100 percent at 10 microns. Additionally, physical measurements of the composition of artificial smoke demonstrated that it consists of spherical droplets and almost never solid particles. The results of recent artificial smoke experiments conducted in our laboratory are in good agreement with Arnulf's findings and indicate that the polarization discrimination technique works equally well for smoke clouds. The theoretical and experimental program should be expanded to include an evaluation of the effectiveness of the discrimination technique in other aerosols such as smog and smoke.

REFERENCES

1. Airy, G. B. "On the Diffraction of an Object-Glass with Circular Aperture," Trans. Cambridge Philos. Soc. V, p. 283., 1935.
2. Aitken, J. "On Dust, Fogs and Clouds," Trans. Roy. Soc. Edin., XXX, p.337, 1880.
3. Arnulf, A., et al. "Transmission by Haze and Fog in the Spectral Region 0.35 to 10 microns," J. Opt. Soc. America, (Vol. 47, No. 6) p. 491-98, 1957.
4. Beckmann, P. and A. Spizzichino. The Scattering of Electromagnetic Waves from Rough Surfaces, New York: MacMillan Co.-Pergamon Press Ltd., 1963.
5. Best, A. C. "Drop Size Distribution in Cloud and Fog," Quart. J. Roy. Met. Soc., LXXVI, 1951.
6. Born, M. and E. Wolf. Principles of Optics, 2nd (rev.) ed. Pergamon Press, 1964.
7. Boylan, R. K. "Atmospheric Dust and Condensation Nuclei," Proc. Roy. Irish Acad., A, XXXVII, 1926.
8. Bricard, J. "Etude de la Constitution des Nuages au Sommet du Puy-de-Dome," La Meteorologie, p. 84, 1939.
9. Bricard, J. "La Teneur des Nuages en eau Condensee," La Meteorologie, p. 57, 1943.
10. Byers, H. R. General Meteorology. McGraw-Hill, Inc., 1959.
11. Carrier, L. W., G. A. Cato, and K. J. von Essen. "The Backscattering and Extinction of Visible and Infrared Radiation by Selected Major Cloud Models," Appl. Opt., (Vol. 6, No. 7), p. 1209-15, 1967.
12. Debye, P. Ann. der Phys. 30, p. 59, 1909.
13. Deirmendjian, D. "Scattering and Polarization Properties of Water Clouds and Hazes in the Visible and Infrared," Appl. Opt., (Vol. 3, No. 2), p. 187, 1964.
14. Dessens, H. "The Use of Spiders' Threads in the Study of Condensation Nuclei," Quart. J. Roy. Met. Soc. 75, 1949.
15. Diem, M. "Messungen der Grösse von Wolkenelementen I," Ann. der Hydrogr., 70, 1942.

16. Diem, M. "Messungen de Grösse von Wolkenelementen II," Met. Rundschau, 1, 1948.
17. Frith, R. "The Size of Cloud Particles in Stratocumulus Cloud," Quar. J. Roy. Met. Soc., 77, 1954.
18. Hagemann, V. "Eine Methode zur Bestimmung der Grösse de Nebel und Wolkenelemente," Gerlands Beitr. zur Geophys., 46, 1936.
19. Hilderbrandsson, H. "Sur la Classification des Nuages Employee a l'Observatoire Meteorologique de'Upsala," Upsala, 1879.
20. Hertz, H. R. Electric Waves. London: MacMillan & Co., Ltd., 1900.
21. Hess, S. L. Introduction to Theoretical Meteorology. New York: Henry Holt and Co., 1959.
22. Houghton, H. G. "The Size and Size Distribution of Fog Particles," Physics. 2, p. 467, 1932.
23. Houghton, H. G. and W. H. Radford. "On the Measurement of Drop Size and Liquid Water Content in Fogs and Clouds," Papers in Phys. Ocean. and Meteorol., (Vol. VI, No. 4), 1938.
24. Houghton, H. G. "On the Relation Between Visibility and the Constitution of Clouds and Fog," J. Aer. Sci., 6, p. 408-11, 1939.
25. Howard, L. "On the Modifications of Clouds," Philos. Mag., 1803.
26. Junge, C. "Zur Frage de Kernwirksamkeit des Staubes," Met. Zeit., LIII, p. 186-8, 1936.
27. Junge, C. "Die Konstitution des Atmosphärischen Aerosols," Ann. Met., 1952.
28. Junge, C. "Die Rolle de Aerosole and der gasförmigen Beimengungen der Luft im Spurenstoffhaushalt der Troposphäre," Tellus, 5, p. 1, 1953.
29. Kelvin, Lord. "On the Equilibrium of Vapour at a Curved Surface of Liquid," Proc. Roy. Soc. Edin., VII, 1870.
30. Kneusel, S. "Die Grösse der Wolkenelemente," Met. Zeit., LII, p. 64-7, 1935.
31. Köhler, H. "Über die Tropfengrössen der Wolken und die Kondensation," Met. Zeit., XXXVIII, 1921.
32. Köhler, H. "Zur Kondensation des Wasserdampfes in der Atmosphäre," Geofys. Publ., II (1921, No. 1; 1922, No. 6).

33. Köhler, H. "The Nucleus in and the Growth of Hygroscopic Droplets," Trans. Faraday Soc., XXXII, Part 8, 1936.
34. Kourganoff, V. Basic Methods in Transfer Problems. Oxford at the Clarendon Press, 1952.
35. Kraus, J. D. Electromagnetics. McGraw-Hill, Inc., 1953.
36. Kuroiwa, D. "Electron-Microscope Study of Fog Nuclei," J. Met., 8, p. 157, 1951.
37. List, R. J. (ed.). Smithsonian Meteorological Tables Smithsonian Institution, Washington, D.C.
38. Lodge, J. P. "Analysis of Micron-Sized Particles," Anal. Chem., 26, 1954.
39. Marshall, S. L. (ed.). Laser Technology and Applications. McGraw-Hill, Inc., 1968.
40. Mason, B. J. The Physics of Clouds. Oxford at the Clarendon Press, 1957.
41. Middleton, W. E. K. Vision Through the Atmosphere. University of Toronto Press, 1952.
42. Mie, G. "Beitrage zur optik trüber Medien, Speziell Kolloidaler Metallosungen," Ann. der Phys. 25 p. 377-445, 1908.
43. Neiburger, M. "Reflection, Absorption, and Transmission of Insolation by Stratus Cloud," J. Met., 6, 1949.
44. Ogiwara, S. and T. Okita. "Electron-Microscope Study of Cloud and Fog Nuclei," Tellus, 1952.
45. Owens, J. S. "Condensation of Water From the Air Upon Hygroscopic Crystals," Proc. Roy. Soc. A., CX, p. 738, 1926.
46. Pauthenier, M. and E. Brun. "Denombrement des Gouttelettes d'un Rrouillard an Mogen d'un Champ Electrique Ionise," Com. R. Acad. Sci., 211, p. 295-6, 1940.
47. Rayleigh, Lord. "On the Light from the Sky, its Polarization and Colour," Phil. Mag., 41, p. 107, 1871.
48. Reisman, E., A. J. Ruhlrig and A. B. Bauer. Active Optical Fuzing Systems. Air Force Weapons Laboratory Technical Report No. AFWL-TR-66-149, Jan. 1968.
49. Renou, E. "Instructions Meteorologiques," Ann. Soc. Met. France, tome 3, Parts, p. 142-6, 1855.

50. Seely, B. K. "Detection of Micron and Sub-micron Chloride Particles," Anal. Chem., 24, 1952.
51. Sewings R. Handbuch der Lichttechnik. Berlin: 1938.
52. Stratton, J. A. and H. G. Houghton. "A theoretical Investigation of the Transmission of Light Through Fog," Phy. Rev., 38, p. 159, 1931.
53. Stratton, J. A. Electromagnetic Theory. McGraw-Hill, Inc., 1941.
54. van de Hulst, H. C. Light Scattering by Small Particles. New York: John Wiley & Sons, Inc., 1957.
55. Watson, G. N. A Treatise on the Theory of Bessel Functions. Cambridge University Press, 2nd ed., 1944.
56. Weickmann, H. K. and H. J. Aufn Kampe. "Physical Properties of Cumulus Clouds," j. Met., 7, 1953.
57. Wigand, A. "Über die Natur der Koudensationskerne in der Atmosphäre Insbesondere Über die Kernwirkung von Staub und Rauch," Met. Zeit, XXX, p. 10, 1913.
58. Wilson, C. T. R. "Condensation of Water Vapour in the Presence of Dust-Free Air and Other Gases," Phil. Trans. Roy. Soc. A., MDCCCXCVII, p. 265, 1897.
59. Wilson, J. G. "Note on Optical Methods of Measuring the Size of Small Water Drops," Proc. Cambridge Philos. Soc., 32, p. 493, 1936.
60. Woodcock, A. H. "Sea Salt Nuclei in a Tropical Storm," J. Met., 7, p. 397, 1950.
61. Woodcock, A. H. "Salt Nuclei in Marine Air as a Function of Altitude and Wind Force," ibid., 10, p. 362, 1953.
62. World Meteorological Organization International Cloud Atlas, Volume I, 1956.
63. Wright, H. L. "The Size of Atmospheric Nuclei: Some Deductions from Measurements of the Numbers of Charged and Uncharged Nuclei at Kew Observatory," Proc. Phys. Soc., XLVIII, p. 675, 1936.
64. Wright, H. L. "Atmospheric Opacity: A study of Visibility Observations in the British Isles," Quart. J. Roy. Met. Soc., LXV, p. 411, 1939.

This page intentionally left blank.

UNCLASSIFIED

Security Classification

DOCUMENT CONTROL DATA - R & D

(Security classification of title, body of abstract and indexing annotation must be entered when the overall report is classified)

1. ORIGINATING ACTIVITY (Corporate author) Air Force Weapons Laboratory (ESA) Kirtland Air Force Base, New Mexico 87117		2a. REPORT SECURITY CLASSIFICATION UNCLASSIFIED	
		2b. GROUP	
3. REPORT TITLE A LADAR CLOUD/TARGET POLARIZATION DISCRIMINATION TECHNIQUE			
4. DESCRIPTIVE NOTES (Type of report and inclusive dates) October 1964-April 1970			
5. AUTHOR(S) (First name, middle initial, last name) Joe E. Manz, Major, USAF			
6. REPORT DATE September 1970		7a. TOTAL NO. OF PAGES 182	7b. NO. OF REFS 64
8a. CONTRACT OR GRANT NO.		9a. ORIGINATOR'S REPORT NUMBER(S) AFWL-TR-70-76	
b. PROJECT NO. 5791			
c. Task No. 028		9b. OTHER REPORT NO(S) (Any other numbers that may be assigned this report)	
d.			
10. DISTRIBUTION STATEMENT This document has been approved for public release and sale; its distribution is unlimited.			
11. SUPPLEMENTARY NOTES		12. SPONSORING MILITARY ACTIVITY AFWL (ESA) Kirtland AFB, NM 87117	
13. ABSTRACT (Distribution Limitation Statement No. 1) The use of laser detection and ranging (ladar) systems in the atmosphere is limited by the severe attenuation of the signal due to absorption by atmospheric gases and/or scattering by cloud and fog particles. Furthermore, the cloud and fog particles may scatter the transmitted radiation toward the receiver, thus producing a false return, which must be distinguished from the true target return. Described herein is an optical polarization technique for discriminating between a cloud return and a target return. Also presented are the results of a research program which demonstrated the validity of the discrimination technique both in the laboratory and in the field. The discrimination technique is based on the theory that if a linearly polarized laser beam propagating through an atmospheric cloud or fog is incident on a diffuse surface, then according to Mie theory the radiation scattered from the cloud is either linearly or elliptically polarized while the radiation reflected from the surface is depolarized. The results of the investigation described have shown that if the transmitter output of a ladar system is linearly polarized and an analyzer with its plane of polarization perpendicular to that of the transmitted wave is placed at the input to the receiver (which is adjacent to the transmitter), then the cloud return will be up to 94 percent less than the value obtained when the analyzer's plane of polarization is parallel to that of the transmitted signal. The target return remains unchanged. The conclusion is that the cloud/target discrimination technique will greatly improve the capability of a ladar system to distinguish between an atmospheric cloud and a target.			

DD FORM 1 NOV 65 1473

UNCLASSIFIED

Security Classification

14

KEY WORDS

LADAR
Laser Radar
Cloud Physics
Cloud Chamber
MIE Theory of Scattering
Polarization

LINK A

LINK B

LINK C

ROLE

WT

ROLE

WT

ROLE

WT